Bubbles propagation in undoped and Titanium (Ti3+)-doped sapphire crystals grown by Czochralski (Cz) technique

Hui Li

▶ **To cite this version:**

Hui Li. Bubbles propagation in undoped and Titanium (Ti3+)-doped sapphire crystals grown by Czochralski (Cz) technique. Cristallography. Université Claude Bernard - Lyon I, 2014. English. NNT : 2014LYO10327 . tel-01136566

HAL Id: tel-01136566

https://theses.hal.science/tel-01136566

Submitted on 27 Mar 2015

HAL is a multi-disciplinary open access archive for the deposit and dissemination of scientific research documents, whether they are published or not. The documents may come from teaching and research institutions in France or abroad, or from public or private research centers.

L'archive ouverte pluridisciplinaire **HAL**, est destinée au dépôt et à la diffusion de documents scientifiques de niveau recherche, publiés ou non, émanant des établissements d'enseignement et de recherche français ou étrangers, des laboratoires publics ou privés.

N° d'ordre Année 2014

THESE DE L'UNIVERSITE DE LYON

Délivrée par
L'UNIVERSITE CLAUDE BERNARD LYON 1

ECOLE DOCTORALE
Chimie

DIPLOME DE DOCTORAT
(Arrêté du 7 août 2006)
Soutenue publiquement le 08 décembre 2014

par

HUI LI

Titre

Bubbles propagation in undoped and Titanium (Ti^{3+})-doped sapphire crystals grown by Czochralski (Cz) technique

Directeur de thèse :
M. KheirreddineLebbou
Co-directeur de thèse :
Alain Brenier

JURY

Pr Patricia Segonds	Rapporteur
Pr Mohamed Abdou Djouadi	Rapporteur
Pr Gérard Panczer	Examinateur
Dr Pascal Loiseau	Examinateur
Dr Kheirreddine Lebbou	Directeur de thèse
Dr Alain Brenier	Co-directeur de thèse

UNIVERSITE CLAUDE BERNARD - LYON 1

Président de l'Université	**M. François-Noël GILLY**
Vice-président du Conseil d'Administration	M. le Professeur Hamda BEN HADID
Vice-président du Conseil des Etudes et de la Vie Universitaire	M. le Professeur Philippe LALLE
Vice-président du Conseil Scientifique	M. le Professeur Germain GILLET
Directeur Général des Services	M. Alain HELLEU

COMPOSANTES SANTE

Faculté de Médecine Lyon Est – Claude Bernard	Directeur : M. le Professeur J. ETIENNE
Faculté de Médecine et de Maïeutique Lyon Sud – Charles Mérieux	Directeur : Mme la Professeure C. BURILLON
Faculté d'Odontologie	Directeur : M. le Professeur D. BOURGEOIS
Institut des Sciences Pharmaceutiques et Biologiques	Directeur : Mme la Professeure C. VINCIGUERRA
Institut des Sciences et Techniques de la Réadaptation	Directeur : M. le Professeur Y. MATILLON
Département de formation et Centre de Recherche en Biologie Humaine	Directeur : Mme. la Professeure A-M. SCHOTT

COMPOSANTES ET DEPARTEMENTS DE SCIENCES ET TECHNOLOGIE

Faculté des Sciences et Technologies	Directeur : M. F. DE MARCHI
Département Biologie	Directeur : M. le Professeur F. FLEURY
Département Chimie Biochimie	Directeur : Mme Caroline FELIX
Département GEP	Directeur : M. Hassan HAMMOURI
Département Informatique	Directeur : M. le Professeur S. AKKOUCHE
Département Mathématiques	Directeur : M. le Professeur Georges TOMANOV
Département Mécanique	Directeur : M. le Professeur H. BEN HADID
Département Physique	Directeur : M. Jean-Claude PLENET
UFR Sciences et Techniques des Activités Physiques et Sportives	Directeur : M. Y.VANPOULLE
Observatoire des Sciences de l'Univers de Lyon	Directeur : M. B. GUIDERDONI
Polytech Lyon	Directeur : M. P. FOURNIER
Ecole Supérieure de Chimie Physique Electronique	Directeur : M. G. PIGNAULT
Institut Universitaire de Technologie de Lyon 1	Directeur : M. le Professeur C. VITON
Ecole Supérieure du Professorat et de l'Education	Directeur : M. le Professeur A. MOUGNIOTTE
Institut de Science Financière et d'Assurances	Directeur : M. N. LEBOISNE

Acknowledgements

This thesis is finished under the instruction of my supervisor mister Kheirreddine Lebbou. He showed me how a true researcher of science should be. Since I started my research of PhD, he taught me the ways how to do research, influenced me enjoying my work with great passion, indoctrinated me to be serious, precise, active and creative with the work, he also supplied an easy work environment for every student. I am deeply grateful to all he did for my improvement. Thank very much my co-supervisor mister Alain Brenier, he is always nice and tolerant with me, instructed me how to manipulate the laboratory equipments, replied all my problems and modified my papers.

Thanks a lot to professor Patricia Segonds and professor Mohamed Abdou Djouadi for accepting to be referee of my PhD thesis. Great thank for Professor Gérard Panczer and Dr Pascal Loiseauto takeing your time in the committee. Thank you very much!

Thanks to professor Akira Yoshikawa from Tohoku University (Japan) for his kind help to do X-ray rocking curve for us. Thanks to RSA Le Rubis company to provide us alumina powder and alumina crackle. Great thanks!

During my research, professor Gerard Panczer and professor Jin Yu gave me great support on luminescence and LIBS measurements, thank very much! Thank the help from mister Laurent Grosvalet and madame Elodie Romeo on cutting and polishing the samples. Thank the support from mister Huguengy Hervé and mister Ingargiola Jean-Marc on my work. Thank madame Martinez Valérie, mister De Ligny Dominique and mister Le Brusq Jacques helped me a lot on raman measurement. Thank Dr Federico Moretti and Dr Guillaume Alombert supplied me great help on luminescence and wavefront measurements. In the laboratory, Dr Abdeldjelil Nehari, Ahmed Ghezal, Benamara Omar, Kononets Valerii and Xiaochun Wang had many helpful discussion with me about the experiments, thanks a lot!

Madame Aloui Ouassilla gave me much kind care on my life, that makes me

feeling as in the home, I appreciate her very much! Thank the great support from my family. Thank Chinese scholarship council (CSC) imburse me during my three years study, thank Zhengzhou University gave me this chance coming to France for my PhD study. Thank my Chinese supervisor professor Shaokang Guan, who gave me great support on my study and life, I respect him and appreciate him a lot!

All above support me finished my PhD thesis, thank you very much!

Contents

Bubbles propagation in undoped and Titanium (Ti^{3+})-doped sapphire crystals grown by Czochralski (Cz) technique

Abstract

In spite of the chemical simplicity, the congruent melt behaviour and it's performed mechanical and optical properties sapphire single crystals contain bubbles defects also known as micro-voids. Whatever the growth technology, the grown crystals are characterized by the presence of micro and macro bubbles which affect the optical and mechanical quality of the crystal limiting their application. They degrade the optical properties and the laser efficiency by reduction of the transparency; they also induce surface defects during substrate polishing process. In order to improve the crystal quality, it is important to eliminate bubbles defects and know the reason of their formation, the causes of their propagation, their incorporation and their distribution in the crystal. We have studied bubbles distribution and their size in undoped and Ti-doped sapphire crystals grown by Czochralski (Cz) technique. The collected experimental data made it possible to know the effect of several growth parameters on the distribution, the density and the size of the bubbles. The bubbles propagation and distribution in the crystal are not influenced by the seed type. If the pulling rate increases, the diameter of bubbles decreases and their density increases. The bubbles formed in sapphire crystal are influenced by the starting charge material. Using sapphire crackle as starting charge could be a good way to minimise bubbles creation and limited their propagation. The obtained results in the frame of this thesis describe the whole phenomena involved during bubbles incorporation in undoped and Ti-doped sapphire crystals.

Keywords: Bubbles, Czochralski, sapphire, crystal, propagation, interface, opticalproperties

Propagation des bulles dans le saphir non dopé et dopé Titane (Ti^{3+}) cristallisé par la technique Czochralski (Cz)

Résumé

En dépit de leurs simplicités chimiques, de leurs fusion congruente, de leurs performances mécaniques et de leurs propriétés optiques, les monocristaux de saphir contiennent comme défauts des bulles aussi connus sous le nom de micro-vides. Quelle que soit la technologie de croissance, les cristaux obtenus sont caractérisés par la présence de micro-et macro-bulles qui affectent leurs qualités optiques et mécaniques limitant ainsi leurs applications. Ces bulles dégradent les propriétés optiques et l'efficacité des lasers produits par une réduction de la transparence des saphirs; elles induisent également des défauts de surface pendant le processus de polissage. Afin d'améliorer la qualité des cristaux, il est important d'éliminer les bulles, de connaître la raison de leurs formations, les causes de leurs propagations, de leurs constitutions, et de leurs diffusions dans le cristal. Nous avons étudié la distribution des bulles et leurs tailles dans les cristaux de saphir non dopés et dopés titane obtenus par la technique Czochralski (Cz). Les données expérimentales recueillies ont permis de connaître l'effet de différents paramètres de croissance sur la distribution, la densité et la taille des bulles. La propagation des bulles et leurs distributions dans les cristaux ne sont pas influencées par le type de germe. Si les vitesses de tirages augmentent, le diamètre des bulles diminuent et leurs densités augmentent. Les bulles formées dans le cristal de saphir sont influencées par la matière formant la charge de départ. L'utilisation de saphirs craquelés comme charge de départ pourrait être une bonne façon de minimiser la création de bulles et de limiter leurs propagations. Les résultats obtenus dans le cadre de cette thèse décrivent l'ensemble des phénomènes impliqués lors de l'incorporation de bulles dans les cristaux de saphir non dopés et dopés titane.

Mots clefs : Bulles, Czochralski, saphir, cristal, propagation, interface, propriétés optiques

Introduction

Due to several predominations compared to other materials, sapphire is one of the most significant tendencies in modern materials science: the raw material for sapphire production is readily available and cheap; the growth technology of sapphire production is less energy-intensive than alternative materials and allows the growth of large-size crystals; sapphire production does not pollute the environment, the growth of sapphire is less harmful than that of alternative materials.

Sapphire is a multifunctional material, it possesses high corrosion and radiation resistance, high mechanical strength, good thermal conductivity, low thermal expansion coefficient, high hardness and high biological compatibility, especially its perfection in the transmission from the ultraviolet 190 nm through the visible and into the midwave infrared. The outstanding physical and chemical properties make sapphire widely applied in medical implants, epitaxial substrate material of new semiconductor GaN, optical window, excellent material of light emitting diodes (LED), laser diodes (LD) and special light source tube, wearable parts of jewel bearing, watch bearing, instrument bearing and precision mechanism. Many growth techniques such as Verneuil, Czochralski (Cz), Kyropolous (Ky), edge defined film fed growth (EFG), heat exchange method (HEM), micro-pulling down (μ-PD) and etc. are employed to grow sapphire crystals.

Since P. Moulton produced laser with Ti-sapphire ($Ti:Al_2O_3$) crystal in 1982, to date Ti-sapphire is recognized the most common and commercially available material of tunable solid-state laser. Ti-sapphire has the widest relative emission bandwidth ($\Delta\lambda/\lambda$) which allows a very broad laser wavelength tunability extending from about 660 to 1180 nm, and the production of the shortest laser pulses, below 10 fs. Ti-doped sapphire lasers can be pumped by gas, solid-state, and diode lasers, or by flashbulb, and work in pulsed and continuous regimens. One laser of this type can be used instead of several lasers with fixed radiation wavelengths. Moreover, Ti-doped

sapphire is ideal laser oscillation and amplification medium of high power tunable lasers and ultrashort pulse, has a broad application prospect in the small terawatt level high power tunable ultrashort pulse laser system.

Large size, ultra-high-quality (free of any defects) sapphire crystals and Ti-sapphire crystals highly doped are required. Therefore, emphasis was placed on the development and improvement of several crystal growth technologies to produce high quality undoped Ti-doped sapphire single crystals. Attempts have been made to scale up the Cz, Bridgman, HEM, GOI, Ky processes to grow large boules. But the high melting point of α-Al_2O_3, the quality requirement of raw material, seed and crucible, the temperature field control, etc. make it difficult to produce sapphire crystals with a high enough defect-free optical quality. With the effort of crystal growth researchers, the defects such as crack, color center, and dislocations were studied and finally can be avoided during the growth process. Among the problems encountered micro-bubbles or micro-voids are difficult to avoid in sapphire and Ti-doped sapphire crystals, this defect degrades their optical quality significantly. Most part of the published papers were focused on the bubbles in shaped sapphire, relatively few studies have examined the bubbles in sapphire grown by Cz method (mainly by our group), this is the motivation of our research topics. Among the results obtained, the shape of bubbles, the relationship between bubbles density and pulling rate, rotation rate were the first time studied thoroughly and already published by our team (this thesis). Besides, another problem that makes Ti-doped sapphire difficult to grow, it is the difference size between Ti^{3+} and the substituted Al^{3+} ion in the octahedral site of sapphire cell, which results in Ti^{3+} ions segregation, that is very detrimental to the production of laser quality single crystals. In a word, despite the improvement of crystal growth technology, it is nowadays difficult to grow reproducible bubbles-free and large diameter of undoped and Ti-doped sapphire crystals.

This thesis is included in one project of the team of Dr. Kheirreddine Lebbou. The aim of this project is to characterize the shape, distribution, origin, nucleation and propagation of bubbles in undoped and Ti-doped sapphire crystals. The main aim is to

find the effective way to eliminate the bubbles defects and improve crystal quality to increase their performance. In the last period, E. A. Ghezal studied the bubbles in sapphire fibers grown by μ-PD method, obtained bubbles-free sapphire fibers with appropriate growth parameters. In this Thesis, the bubbles in sapphire and Ti-sapphire crystals grown by Cz technique were studied. Ti-doped sapphire crystals exempt of bubbles and sapphire crystals contained very few bubbles were obtained. The shape, distribution and origin of bubbles were analyzed; the effective methods to eliminate bubbles were proposed.

The thesis manuscript is presented as following:

Chapter I introduces the properties, applications and market of sapphire and Ti-doped sapphire crystals, a monography of the different growth technology of sapphire crystals and the problems encountered during the growth process. The content is helpful to understand the motivation of this thesis and the subsequent experiment parts.

Chapter II is focused on the experimental part related to the growth technique and the characterization tools used in this research program.

Chapter III presents the results part related to the growth and the characterization of undoped sapphire crystals.

Chapter IV presents the results part related to the growth and the characterization of Ti-doped sapphire crystals.

The last part summarizes the main conclusions and the outlook for the future research work.

Chapter I

Background information & literature review

In this chapter, first the basis information of alumina and sapphire crystallization are introduced. The predominance of sapphire and Ti-sapphire crystals make them widely applied in large range of applications, they are more and more required of quantity and quality in the world market. The principles of techniques to grow sapphire crystals are presented. There are some defects come into being during sapphire growth process, the literatures studying these defects are reviewed.

1.1 Sapphire raw material

The raw material for sapphire production is alumina, readily available and cheap. Figure 1.1 exhibits global alumina production by region in 2013 [1], China, after is Oceania, are the biggest suppliers. The global alumina production increased significantly in the past decades, of course it is due to the increasing of market requirement. The total alumina production of the world in 2013 amounts to 102,304 thousand metric tones. The total production in 1974 is 24,343 thousand metric tones, in 1984 is 27,055, in 1994 is 41,771 and in 2004 is 61,866 thousand metric tones. Although there is plenty of alumina resource, its cost is greatly dependent on its quality. The cost of high purity alumina is much more expensive than the inferior purity one. Usually growing sapphire crystal requires high quality alumina.

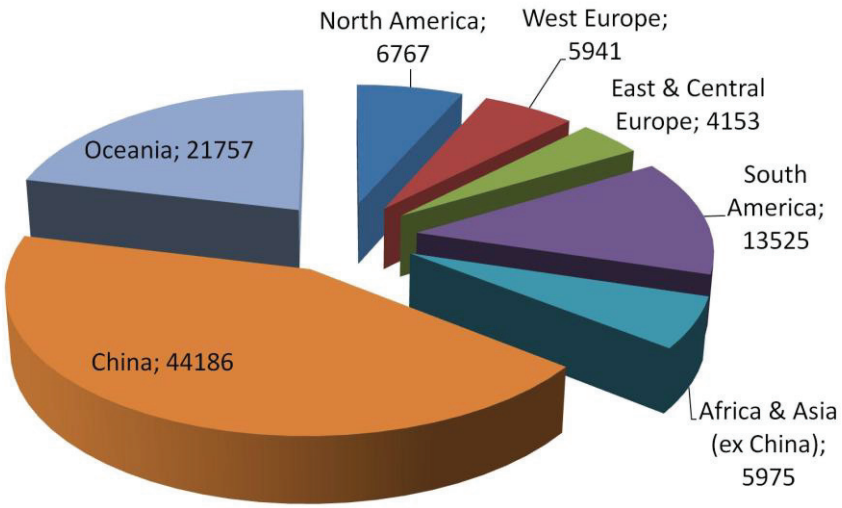

Figure 1.1 Global alumina production in 2013 by region [1] (thousand metric tonnes)

Alumina is mainly produced by bauxite, a mineral rich of resource all over the world. The crystalline form of sapphire is α-Al_2O_3, also named corundum Alumina or aluminum oxides, exist three main families: alumina hydrates, transition alumina and α- alumina. α- alumina is the only stable phase of aluminum oxide (Al_2O_3). The type of obtained alumina depends on the nature of the hydrate decomposition. The general formula of the alumina hydrate is: Al_2O_3 x H_2O, x is the degree of hydration.

There are at least six types of hydrates, which are well defined as:

- Aluminum trihydroxides ($Al(OH)_3$), x=3:gibbsite, bayerite and norstrandite,
- Monohydroxide aluminum (Al_2O_3, H_2O or AlOOH), x=1:boehmite and diaspore,
- Hydroxides very dehydrated (Al_2O_3, 1/5 H_2O), x=0.2:tohdite.

There are only gibbsite, bayerite, boehmite and diaspore are naturally in existence. However, they can also be obtained in the laboratory by different preparation methods. The transition alumina are derived from the thermal dehydration alumina hydrate, and the final dehydration stage leads to the α-alumina. There are eight crystallographic forms of alumina. The best known are: η, γ, δ, θ and α, and less known are: χ, κ and ρ. Hydroxides have common structural features: there is a common oxygen network well defined, where the aluminum atoms are placed differently according to hydroxides. The mechanism of the dehydroxylation is driven by the symmetry of original hydroxide oxygen networks, then the production of transition alumina is obtained. The transformation in transition alumina involves complex processes, strongly depends on the temperature, the sequences of transformations of aluminum hydroxides to phase α-Al_2O_3 are schematically shown as below [2]:

Gibbsite (γ-$Al(OH)_3$) $\xrightarrow{150\text{-}300^{o}C}$ χ−Al_2O_3 $\xrightarrow{650\text{-}750^{o}C}$ κ-Al_2O_3 $\xrightarrow{1000^{o}C}$ α-Al_2O_3

Boehmite(γ-AlO(OH)) $\xrightarrow{300\text{-}500^{o}C}$ γ-Al_2O_3 $\xrightarrow{700\text{-}800^{o}C}$ δ-Al_2O_3 $\xrightarrow{900\text{-}1000^{o}C}$ θ-Al_2O_3 $\xrightarrow{1000\text{-}1100^{o}C}$ α-Al_2O_3

Bayerite (α-$Al(OH)_3$) $\xrightarrow{200\text{-}300^{o}C}$ η-Al_2O_3 $\xrightarrow{600\text{-}800^{o}C}$ θ-Al_2O_3 $\xrightarrow{1000\text{-}1100^{o}C}$ α-Al_2O_3

Boehmite(α-AlO(OH)) $\xrightarrow{700\text{-}800^{o}C}$ α-Al_2O_3

1.2 The structure of sapphire

Sapphire is a simple coordinated type oxide crystal, whose chemical composition is Al_2O_3 and crystalline form is α-Al_2O_3. Sapphire, also named corundum, which belongs to the ditrigonal-scalenohedral class of the trigonal symmetry D^6_{3d}–$R\bar{3}C$ ($L_3 3L_2 3PC$) with symmetry elements: Mirror-turn axis of the sixth order (ternary inversion axis), three axes of the second order normal to it, three symmetry planes normal to the axes of the second order and intercrossing along the axis of the highest order and symmetry center [3]. There are seven simple forms (facets) in this class of symmetry. According to Bravais classification they have the following symbols: pinacoid (0001), hexagonal prisms $\{10\bar{1}0\}$and $\{11\bar{2}0\}$, dihexagonal prism {hki0}, rhombohedron $\{h0\bar{h}l\}$, hexagonal bipyramid $\{hh2\bar{h}l\}$, and ditrigonal scalenohedron. Depending on its position with respect to the hexagonal crystallographic axes, the rhombohedron may be "positive" $\{10\bar{1}1\}$ or "negative" $\{01\bar{1}1\}$.

The crystal lattice of α-Al_2O_3 is formed by Al^{3+} and O^{2-} ions. If the O^{2-} anions are depicted as balls, the crystal lattice takes the form of their closest hexagonal packing. The Al^{3+} cations are located in a crystalline field that has no symmetry center (due to crystal lattice distortions). These cations lie in the octahedral hollows between the closely packed O^{2-} ions, filling two thirds of these hollows. The octahedron hollow is surrounded by six balls. If the radius of each is taken as a unit, then the hollow contains a ball with a relative radius of 0.41. Due to the ratio of the ionic radii of O^{2-} and Al^{3+} (equal to 1.40 and 0.57 Å, respectively), the cations are located within the hollows of the anion packing. They slightly distort the lattice, but do not fall outside the stability limits of the octahedron position. The coordination numbers for

Al^{3+} and O^{2-} are 6 and 4, respectively. The three upper O^{2-} ions in the octahedron are turned about 64.3° with respect to the three lower O^{2-} ions and lie in parallel planes at a distance of 2.164 Å from each other. The closest packing distortion bound up with the discrepancy between the size of Al^{3+} and the octahedron position is manifested by the fact that the octahedron is formed by oxygen triangles of different size, and their rotation angle of 64.3° exceeds the value characteristic of ideal packing (60°). The structure with the spatial symmetry group $D^6_{3d} - R\bar{3}C$ can be considered to be a slightly distorted closest hexagonal packing of oxygen ions. In the crystal lattice of sapphire, two structural elementary cells — hexagonal and rhombohedral— can be distinguished. The shape of natural crystals usually has the following facets (denoted by the most often used literal symbols): c (0001), a $\{11\bar{2}0\}$, r $\{10\bar{1}1\}$, n $\{22\bar{4}3\}$, m $\{10\bar{1}0\}$, s $\{02\bar{2}1\}$, s $\{22\bar{4}3\}$, R $\{01\bar{1}2\}$, p $\{11\bar{2}3\}$ (figure 1.2) and others.

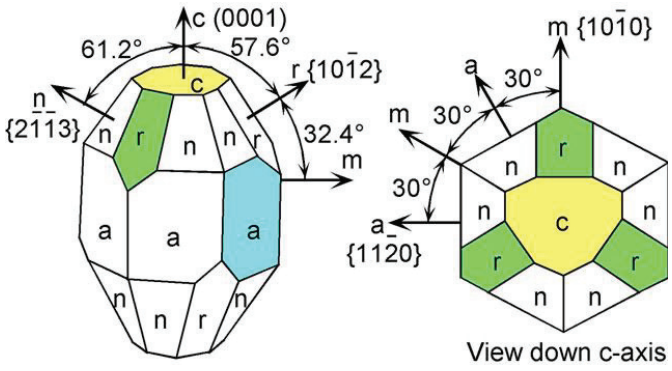

Figure 1.2 Crystallographic diagram of sapphire

1.3 The properties of sapphire

Sapphire has high melting temperature 2050°C, can be used at up to 1900°C. Table 1.1 presents the main properties of the sapphire crystal. Sapphire has a high refractive index and a broad transmission band from 0.14 to 6.0 μm, spanning the UV, visible, and IR bands. Sapphire also has a high hardness and surface smoothness, very good tensile strength, thermal conductivity, electric insulation, wear resistance, and thermal shock resistance. The chemical properties of sapphire are excellent. Generally, sapphire is insoluble in water; insoluble in nitric acid (HNO_3), sulfuric acid (H_2SO_4),

hydrochloric acid (HCL), hydrofluoric acid (HF) and phosphoric acid (H_3PO_4) up to 300°C; and insoluble in alkalis up to 800°C. The favorable combination of excellent optical and mechanical properties of sapphire, together with high chemical durability, makes it a desirable substrate material for LED applications.

Table 1.1 Properties of sapphire [4]

Physical Properties	
Chemical Formula	Al_2O_3
Structure	hexagonal-rhombodedral
Molecular weight	101.96
Lattice Constants Å	a=4.765, c=13,000
solid density (g/cm^3)	3.98
Melt density (g/cm^3)	3.0
Hardness	9 Mohs 1800 knoop parallel to C-axis 2200 knoop perpendicular to C-axis
Young Modulus (GPa)	379 at 30° to C-axis 352 at 45° to C-axis 345 at 60° to C-axis 386 at 75° to C-axis
Shear Modulus (GPa)	145
Bulk Modulus (GPa)	240
Bending Modulus/ Modulus of Rupture (MPa)	350 to 690
Tensile strength	400 at 25°C 275 at 500°C 345 at 1000°C
Elastic Coefficient	C=496, C_{12}=164, C_{13}=115, C_{33}=498, C_{44}=148
Apparent Elastic Limit (MPa)	448 to 689
Flexural Strength (GPa)	2.5 - 4.0
Poisson ratio	0.25 - 0.30
Friction Coefficient	0.15 on steel 0.10 on sapphire
Abrasion resistance	8 times higher than steel
Thermal Properties	
Melting Point (°C)	2050
Specific Heat J/(kg ·K)	105 at 91 K 761 at 291 K
Thermal coefficient of linear expansion at 323 K (K^{-1})	66.66×10-6 parallel to optical axis 5×10-6 perpendicular to optical axis

Thermal conductivity (W/m °K) at 20°C	41.9
Thermal Expansion (20-1000°C)	Parallel to C-axis: 9.03×10^{-6} °C Perpendicular to C-axis: 8.31×10^{-6} °C 60° to C-axis: 8.4×10^{-6} °C
Optical Properties	
Transission Range	0.2 - 5.5 microns
Reflection loss	14% at 1 micron (2 surfaces)
Restrahlen Peak	13.5 micron
dN/dT	$+13\times10^{-6}$ °C
Refractive index	1.7122
T_t%	87.1
Electrical Properties	
Resistivity, Ohm•cm at 20 - 500°C	10^{11} - 10^{16}
Dielectric Constant	11.5 parallel to C axis 9.4 perpendicular to C axis
Dielectric strength (V/cm)	4×10^{5}
Loss Tangent	10^{-4}

1.4 The application of sapphire

Sapphire has excellent physical, mechanical, chemical, thermal and optical properties, are widely used in jewelry industry, engineering, optics, medicine and military applications [3]. Because the natural gems are very rare and have few choices of hues, people attempt to obtain synthetic crystals of different colors to satisfy the requirements of jewelry. The most widespread ways for changing the color of the sapphire crystals are shown as below: irradiation, implantation of ions, thermal treatment in different gaseous media and thermochemical treatment. Table 1.2 shows the brightest colors with nice hues by introducing a mixture of components into the starting material for the growth of color corundum crystals. However, the color or hue required cannot always be achieved.

The high mechanical strength, high hardness and good transparence make sapphire historically applied in the watch industry. Another important trend is nowadays more and more companies using sapphire as the screen cover and rim for mobile phone. With its reasonable cost, stable quality, high hardness, and good wear resistance, sapphire turned out to be suitable for wear-resistant part of mechanical

instruments such as sapphire jet-forming nozzles in water-jet cutting etc. Besides, sapphire substrates are used for epitaxy of semiconductor films such as Si, GaN, AlGaN, and for making integrated circuits.

Table 1.2 Corundum color with different impurities [3]

The crystal color	Impurity component
Red, pink	Cr_2O_3
Blue	$TiO_2 + Fe_2O_3$
Orange	$NiO + Fe_2O_3$
Orange (padparajah type)	$NiO + Cr_2O_3$
Yellow	NiO
Green (tourmaline type)	$Co_2O_3 + V_2O_3$
Dark-red (garnet type)	$Cr_2O_3 + TiO_2 + Fe_2O_3$
Violet	$TiO_2 + Fe_2O_3 + Cr_2O_3$

Sapphire has excellent chemical stability, perfect transmission from the ultraviolet 190 nm through the visible and into the midwave infrared, these make sapphire optic windows with diameters from several millimeters to several hundreds of millimeters are applied in various devices that work under high pressure, high temperature and aggressive environment. The low reactivity and appropriate unit cell size make sapphire an excellent substrate materials in blue, green, ultraviolet and white light-emitting diodes (LEDs). Besides, sapphire lenses and prism, sapphire light guides, thermocouple casings made of sapphire, sapphire meniscuses (domes) shaped as hemispheres, thermoluminescent detectors (TLDs) made of sapphire etc. are used widely in optics domain.

Owing to their high corrosion and erosion resistance, chemical ware such as crucibles, boats, measuring glasses, reactor housings, and other articles came into use after the development of shaped sapphire growth methods. Sapphire capillaries are used for investigating microexplosions, the growth of biocrystals, micro-dose measuring facilities, and other applications. Sapphire fibers are used for the creation of compositional materials; they reinforce metallic and ceramic composites. Sapphire abrasive (α-Al_2O_3) crystal particles are an extremely sharp grinding, long-lasting, blasting abrasive that can be recycled many times.

At the mention of application of sapphire in medicine, sapphire possesses high biological compatibility, can be inserted (implanted) in human tissue, as these stones do not react with organic acids and tissues; they are superior to all known constructional materials in inertness, as an example, the use of sapphire in friction pairs is of particular interest. Sapphire dental implants have more functional merits compare to other widely used material. Except sapphire implants, due to their high hardness and chemical inertness in any media (including those of the patient), sapphire tools e.g. microscalpels are used in all the branches of microsurgery, large-size scalpels are employed in general surgery also.

Table 1.3 Characteristics of Ti^{3+}:Al_2O_3 lasers [3]

Source of pumping	Tuning range (μm)	Eps (J)	Pps (W)	Eth	Efficiency (%) Full	Efficiency (%) Differential
Continuous coherent pumping – Ar-laser	0.715–1.14	—	1.6	2.6 W	13.3	19.1
Pulse-coherent pumping Quasicontinuous laser on YAG with frequency doubling	0.675–0.950		0.38	25 mJ	46–50	68–72
Laser on rhodomyn dye 6G with lamp pumping	0.660–0.986	0.0065	—	2 mJ	44	67
Monopulse laser on YAG with frequency doubling	0.65–1.20	0.03	1.2	0.5–2.5	42–44	70
Pulse nonselective pumping	0.72–0.92	0.3	0.15	11 J	0.2	0.5

Minimum width of generation line (pumping of the amplifier and generator by YAG lasers with frequency doubling) = 0.08 Å

Luminescence lifetime at temperature: 3.9 μ s (T < 150 K) 2.9 μ s (T = 300 K)

Saturation energy density in the region of pumping by pulse emission (532 nm, 10 ns, π -polarization) = 7.6 J/cm^2

Absorption cross section near 532 nm = $4.9 \cdot 10^{-20}$ cm^2

Doped sapphire crystals are promising material for tunable lasers, such as Ti^{3+}, Cr^{3+}, Cu^{2+} , V^{3+} , Ni^{2+} , Co^{2+} , Co^{3+} , possessing wide absorption bands and wide emission regions. The most interesting dopant among these elements is Ti^{3+}. Ti:Sapphire (Ti^{3+}:Al_2O_3) lasers were introduced by Moulton at Lincoln Laboratory in 1982 [6]. A wide variety of developments in Ti^{3+}:Al_2O_3 1aser technology then followed the advances in crystal growth that occurred during the mid-1980s [7]. Octahedrally coordinated Ti^{3+}-doped crystals were thoroughly investigated as possible

tunable laser materials. Efficient laser oscillation was obtained in Al_2O_3 in pulsed and continuous-wave operation. The tuning range Ti^{3+}:Al_2O_3 1aser is≈670–1100 nm. In mode-locked operation, pulses as short as ~5 fs were achieved. To date, Ti^{3+}:Al_2O_3 is the most common and commercially available tunable solid-state laser [8]. Ti^{3+}:Al_2O_3 is ideal laser oscillation and amplification medium of high power tunable lasers and ultrashort pulse, besides, it has a broad application prospect in the small terawatt level high power tunable ultrashort pulse laser system [9]. Moreover, Ti^{3+}:Al_2O_3 lasers can be pumped by gas, solid-state, and diode lasers, or by flashbulb, and work in pulsed and continuous regimens. One laser of this type can be used instead of several lasers with fixed radiation wavelengths. The generation characteristics of Ti^{3+}:Al_2O_3 are presented in table 1.3 [3].

1.5 Sapphire market

As is introduced in the previous section, sapphire is widely utilized in many regions of military and civilian applications, the demand of sapphire is increasing greatly. The annual output in the world of monocrystal increased from 5000 tons in 1979 to 11000 tons in 1986, and to 20000 tons in 1999, thereinto 60% are semiconductor Si, GaAs, InP, GaP, CdTe and so on [10]. Figure 1.3 shows that laser and nonlinear crystals, crystals used in jewelry and watch, acoustic crystals occupied respectively 10%, optical crystals and scintillation crystals occupied less than 10% in all. At present, the proportion of single crystal yield is changed, the production of mobile phones requires some 6 billion sapphire glasses annually, and this quantity is expected increasing significantly year by year. At the same time, if the technology progress allows growing enough big bulk sapphire of high quality, it can be anticipated that in the near future sapphire display will be employed for computer and television. Of course, the cost will be very high also. So conversely, more high growth rate is required to decrease the cost. Which reflected the beneficial improvement of industrial demand to technology progress.

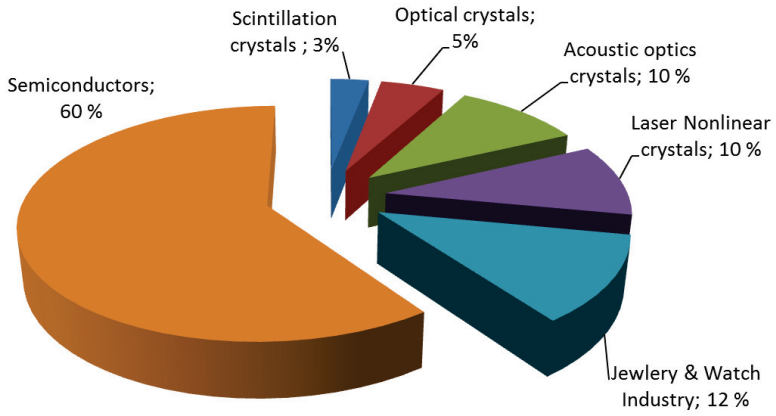

Figure 1.3 Proportion chart of single crystal yield (20.000 t) in the world in 1999 [10]

The total synthetic sapphire production in 2005 is approximately 1,250 million carat, equal 250 tons [11]. The specialists consider by 2008 the world sapphire market of synthetic crystals is about $2.8 billion. The growth rate of sapphire production is extremely high. One should expect that during the next 20 years the world production of sapphire will increase approximately tenfold. In 2010, the leading manufacturers of sapphire are the United States, Japan and Europe. In the United States, sapphire crystals are grown by the Czochralski, HEM, and EFG methods. In the after several years, the rate of sapphire production is being stepped up in China and Korea. To 2013, the annual sapphire production rate in China is 34%. However, lots of works are needed to improve the quality of these products. Since the beginning of 2004, contradictory tendencies have been observed for sapphire world market. At the same time, technical requirements for the quality of the material itself and the working surfaces of sapphire articles become ever more stringent. The performed analysis indicates that one of most important problems for the development of sapphire production is the increase of crystal size. This is explained not only by economic considerations, but also by technical requirements. The main trend in the development of the sapphire industry will be the increase in the size of the grown crystals. In addition, there are some researchers make efforts on the creation of technologies for obtaining permanent sapphire joints such as gluing, bonding, weld and so on [3] [12].

1.6 The growth technology of sapphire

The theories of crystal growth developed very slowly because crystal growth is a nonequilibrium process. The cultivation of crystal growth talents is lagging in all countries in the world, which makes the development of crystal growth technique in face of severe situation. This phenomenon mainly results from the complexity of crystal growth. Buckley called crystal growth as an art in his book [13], Gilman even put the word "art" in the name of his book [14], these all reveal its complexity. The complexity of crystal growth technique exhibits in the following aspects: first it's a multidisciplinary field concerns chemistry and chemical engineering, solid and defect chemistry, process engineering, material science and engineering, material physics, thermodynamics and statistical mechanics etc, see the table 1.4. This complexity not only brings a lot of difficulties for education, but also makes troubles for its identity and belongingness- no anyone department in the university feels itself suitable for crystal growth technique. Besides, phase transformation occurs during the process of crystal growth, which will change the structure and physicochemical properties of material, thus increase the complexity. Crystal growth also has the scale problem, for example, it's required to control the crystal growth in nano scale shape in the system unit of growth in meters, further more required with the corresponding time and energy criterion. The complexity of the crystal growth is also reflected in the aspect that it is a process of multi parameters includes the impacts of dimension, calorifics, chemistry, supersaturation, hydrodynamics and the interactions between them. The optimization of these parameters are mainly realized by the repeated tests and the accumulation of experience. The optimization of these parameters is achieved by repeated tests and accumulated experience, during the process of optimization it is usually needed to be considered completely different applications, for example, to form the facet [15] and increase structural integrity [16] needed to take small temperature gradient, but to get more stable growth interface [17] and high growth rate needed to take big temperature gradient.

Table 1.4 The complexity of crystal growth technique [18]

a) Multi-Disciplinary
   - Chemistry (all fields) including Chemical Engineering
   - Materials Science & Engineering
   - Mechanical & Electrical Engineering (especially hydrodynamics, machine design, process control)
   - Theoretical Physics (especially thermodynamics, non-equilibrium thermodynamics, statistical mechanics)
   - Applied Crystallography and Crystal Chemistry
   - Solid-State Physics

b) Complexity
   - Phase Transformation from Fluid (melt, solution, vapour) to Crystal
   - Scaling Problem: Control of surface on nm scale in growth system of ～m size,
   - hampers numerical simulation
   - Complex Structure & Phenomena in Melts and Solutions
   - Multi-Parameter Processes: Optimize and compromise ~10 parameters

Al_2O_3 crystal growth started from 1890, its development up to now almost cover all the crystal growth methods such as floating zone method [19], Kyropoulos method [20], flux method [21], vapor growth method [22] etc., thereinto EFG, HEM, TGT methods are mainly invented for growing Al_2O_3 crystal and all have their own specialty. The LHPG and μ-PD methods usually are applicable to grow Al_2O_3 fibers, Cz method mainly for 3 inches Al_2O_3 crystals, EFG method mainly for shaped sapphire crystals and doped sapphire fibers, the HEM, TGT and Ky methods are mainly for growing bulk sapphire crystals. The classification of crystal growth methods [3] is based on the phase state, the composition of the initial components, and the conditions of the growth process. Based on these factors, one can distinguish the following groups of growth methods (table 1.5):

Table 1.5 Classification of sapphire crystal growth methods

Sapphire crystal growth methods	From gaseous phase	using a pressure gradient	Reaction method
	From the solution	using a concentration gradient at the crystal solution interface	Hydrothermal method
	From the melt	using a temperature gradient	Flame fusion method
			Czochralski method
			Heat exchange method
			Temperature gradient technique
			Flux method
			Kyropoulos method
			Edge defined film fed growth
			Zone melting method
	From the solid phase	the polycrystalline structure possesses excess free energy	Horizontal directional crystallization method

Classification by the type of phase transition (from the vapor phase, solution, melt, or solid phase) is somewhat arbitrary, as the process of crystal formation often proceeds through several phases. More detailed classification by attributes, authors, and so forth seems to be disorienting. For example, in classification of the various crystal growth processes using capillary forces for maintaining or shaping the molten material, Pedestal, Floating zone, and Verneuil methods belong to crucibleless technique, Czochralski, EFG, μ-PD, Dewetted and Encapsulated Bridge methods belong to technique with crucible. On the other hand, Pedestal, Czochralski and EFG methods belong to pulling up technique, while Floating zone, Verneuil, μ-PD, Dewetted and Encapsulated Bridge methods belong to pulling down technique. Besides, Pedestal method is also a special application of Floating zone methods. Although the classification of crystal growth methods by the form of phase transition is formal, researchers prefer to choose the way of classification according to actual requirements. The next part will introduce some important methods for sapphire crystal grown from the melt which are used more frequently.

1.6.1 Verneuil method

In 1885 E. Fremy, E. Feil and Wyse fabricated "Geneva ruby" with crude ruby powder and potassium dichromate melted by oxyhydrogen flame, then in 1890, French chemist A. V. L. Verneuil successfully grew ruby and sapphire single crystals with flame fusion technique [24], he improved this method and made it to fit the requirements of commercial production, so flame fusion technique is also called Verneuil method (figure 1.4), in fact Verneuil can be seemed as the originator of crystal growth technique. The necking down and shouldering technics can not only realize seed selection during the crucible-free crystal growth process, but also control structural integrity to a certain degree. This method can be summarily described as using the high temperature produced by burning oxygen and hydrogen, making the loose material go through the fire and melt, then fall on a cooling crystallization rod and form into single crystal. The manufacturing process of Verneuil method to grow crystals includes four parts: the purification of raw material, powder preparation, crystal growth and annealing. Verneuil method is usually being used to synthesize different gems such as ruby, sapphire, colored spinel, rutile, star ruby and star sapphire, strontium titanate-artificial and so on.

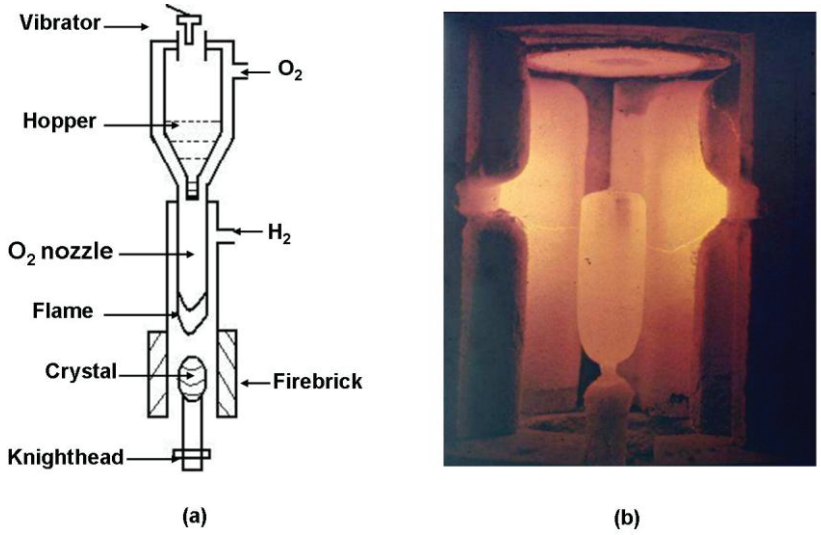

Figure 1.4 Configurations of Verneuil method. (a) schematic graph; (b) apparatus.

1.6.2 Floating zone (FZ)

Horizontal melting zone and vertical floating zone techniques (FZ) belong to melting zone method. The system is formed by three parts: polycrystal, molten zone, growing monocrystal, and exists two solid liquid interface: one taken place in crystallization process, another taken place in melted surface of polycrystal. The volume of molten zone is stationary while the material is variational. With the progress of crystal growing, the melted zone will move toward polycrystal and the latter will be exhausted finally. Originally melting zone is usually considered to be a method for purification of materials at the beginning, it was invented for purifying Si in 1952 by Pfann [25]. At the same time, melting zone is applicable as a crystal growth method since in the process of purification single crystals often are formed.

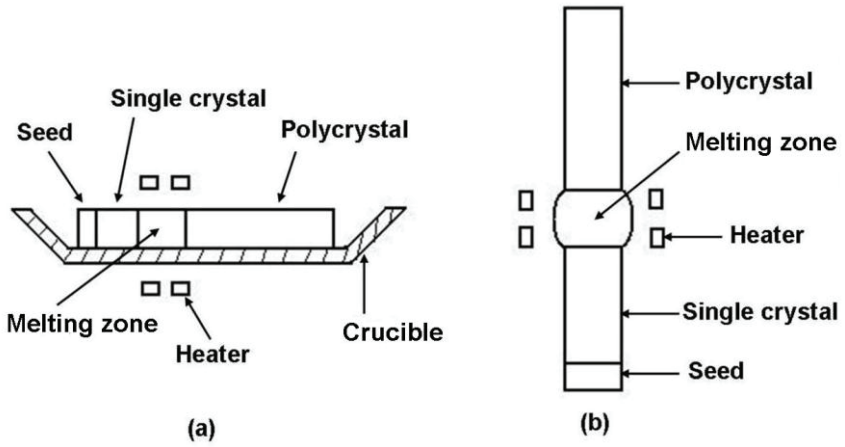

Figure 1.5 Configurations of melting zone method. (a) horizontal; (b) vertical.

Figure 1.5a is illustration of horizontal melting zone. For growing a single crystal, a seed is placed at the left end of the boat. The latter is partly melted to obtain a clean growth surface, then the zone is shifted to the right. If the left end of the boat is narrower, the crystal can nucleate without seed, too. Due to wetting, the grown crystal may stick to the container, and as the linear expansion coefficients of the crystal and the boat are different, inner stresses arise during cooling. Sometimes such difficulties are avoided by using damping boats. The characteristic of FZ (figure 1.5b) is the molten zone between growing crystal and polycrystal is supported by surface tension, the zone is moved from top to bottom or reverses to finish crystallization.

1.6.3 Czochralski (Cz)

Czochralski method (Cz) was invented by Polish chemist Jan Czochralski [26]. In 1950, Bell laboratory in America started to grow Germanium single crystal by this method, reported on the pulling of sapphire single crystals [27], then Cz was used by other scientists gradually to grow semiconductor single crystal, metal crystal and artificial gem etc. At present, induction heating crucible Cz method is more popular. Cz technique is one of the most popular methods for growing crystals from the melt, its main technical characteristics are common foundations of all the pulling methods.

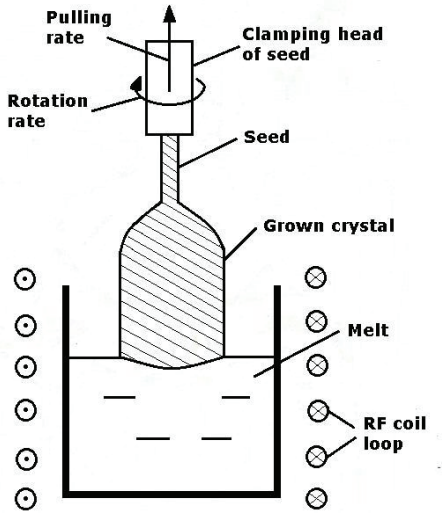

Figure 1.6 Schematic illustration of Cz method

Figure 1.6 shows the schematic principle of Cz technique apparatus. The raw material is melted in a crucible. The material of crucible can be iridium, molybdenum, platinum, graphite and other high temperature oxide. Usually iridium is used for growing sapphire. The crucible is inductively heated and an automatic controlled diameter based on the time derivative of the crystal weight is used for all the growth process. After the material is completely melted, the seed is rotated and dipped into the melt, the melt starts to crystallize on the seed due to temperature gradient, it needs to pay more attention to the pulling rate, rotation rate and heating power during the period of necking down and expand-shouldering, then will start the diameter growth with proper pulling rate, finally is tail ending. The melt and crucible temperature are followed by using an optical pyrometer, protective gas is used inside the growth

chamber, there is a window on the furnace to follow the growth process. In this thesis, Cz technique was used to grow sapphire and Ti-sapphire single crystals, detailed growth parameters and process will be introduced in the next chapter.

1.6.4 Kyropoulos (Ky)

In 1926 S. Kyropoulos of Soviet Union proposed this method [28], in Nineteen seventy Musatov in the State Optical Institute of former Soviet Union improved this technique for growing single sapphire crystals to be later used in optics. Kyropoulos (Ky) method also called the state optical institute method (GOI) can be used on unlimited amounts of melt, in this method growth of crystals is carried out directly in the melt by smoothly decreasing the temperature (figure 1.7). The raw material is melted in the crucible, the power of heater is adjusted to make the temperature of melt surface close to freezing point, connect the seed to the center of melt surface, the seed is partial melted, with the effect of cooling, the melt start to crystallize around the end of the seed downwards and increase shoulder at the same time.

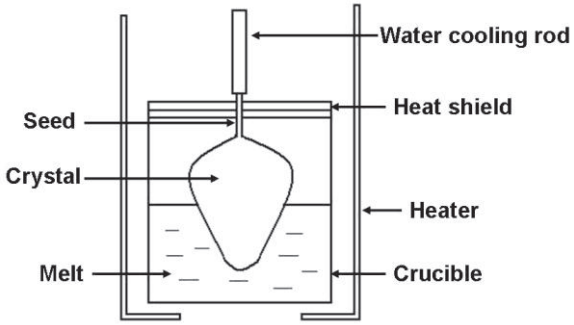

Figure 1.7 Schematic illustration of Ky method

The process of crystal growth includes seeding, shouldering, diameter growth and ending, the single crystal will finish growing until all the melt are exhausted. The important adjustable technical factors of Ky method involve the water flow in water cooling rod and the primary water temperature, the heater power. The main advantage of Ky lies in its technical simplicity and reliability, the possibility of effective screening of the heat source makes it economical.

1.6.5 Edge-defined film-fed growth (EFG)

Edge-defined film-fed growth method (EFG) is invented in 1960s, by Harold E. LaBelle Jr. [29] in Tyco laboratory of US and A.V. Stepanov [30] in USSA of Russia independently, so EFG method is also called Stepanov technique [31,32], belongs to near-net-shaping technique, viz. growing crystals of required shape directly from the melt. The first requirement of EFG is the die material can be wetted by the melt and no chemical reaction between them. Under the condition 0<wetting angle θ<90°, the melt can arise to the top of die by capillary action, then extend to the edge of section and form a film melt layer, so the section shape and size of the crystal is defined by the section shape and size of die (figure 1.8). The EFG is applicable to grow crystals directly from the melt with different shape such as sheets, rods, tubes, threads, ribbons and other specific forms. The melt arise to the top of die by capillary effect, the height of arising is decided by the formula (1.1):

$$h = \frac{2\delta \cos\theta}{drg} \tag{1.1}$$

δ-surface tension, θ-wetting angle, d-melt density, r-radii of capillary, g-acceleration of gravity.

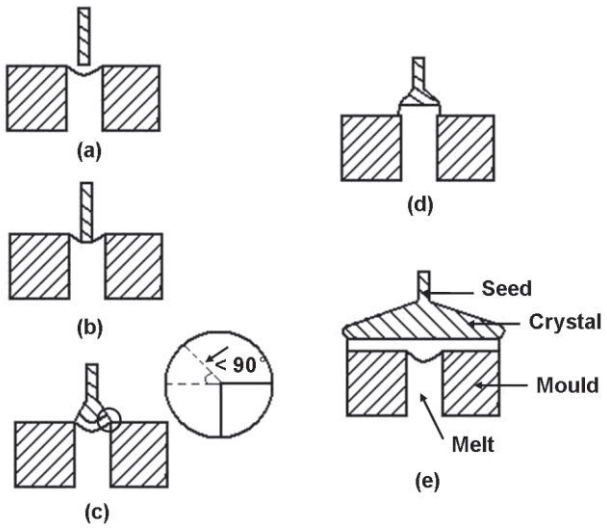

Figure 1.8 EFG crystal growth process. (a) connect the seed to the melt; (b) seed surface remelt; (c) necking, shoulder-expanding and pulling; (d) pulling to make the melt up to top of the mould; (e) crystal growth of specific shape.

1.6.6 Bridgman technique

In 1925 the American physicist Percy Williams Bridgman has a great share in developing today's high pressure furnaces and contributed to crystallography, where he devised a method of growing single crystals [33]. In 1936 D.C. Stockbarger [34] developed this technique into vertical bridgman method (VB) also called Bridgman-stockbarger (B-S) method. In 1959 Weisberg et al. improved into horizontal bridgman method (HB). Bridgman method is a directional crystallization method, means keeping the material in completely melted condition under a special temperature field, then crystallize slowly from one side to another side of the melt. This method is mainly used for growing single crystal, but also can be used for a simple purification as melting zone method. HB (figure 1.9b) method divides into two-temperature zone furnace (2T-HB), three-temperature zone furnace (3T-HB) and gradient solidification furnace (GF).

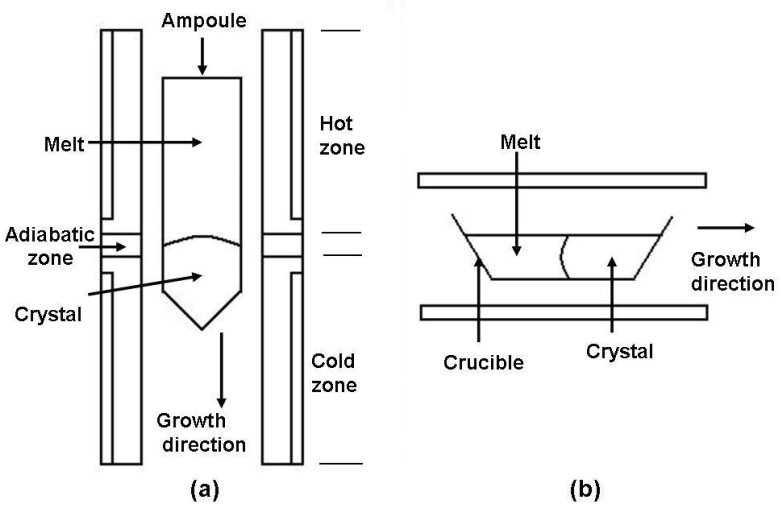

Figure 1.9 Schematic diagram of Bridgman method. (a) VB; (b) HB.

The principle of VB method: vertical the Bridgman furnace works with three temperature zones (figure 1.9a). The upper zone with temperatures above the melting point of raw material, the lower zone with a temperature below melting point and an adiabatic zone as a baffle between the two. The ampoule containg material is raised into the upper zone until only the lower portion of the single crystal seed remain unmelted in the lower zone. After temperature stabilization, the ampoule is lowered

slowly into the lower zone to initiate crystal growth from the seed. Due to a directed and controlled cooling process of the cast, zones of aligned crystal lattices are created growing single crystal.

1.6.7 Heat change method (HEM)

In 1967 F. Schmid and D. Viechnicki at the Army Materials Research Lab in Watertown Massachusetts invented the heat exchanger method (HEM) to grow large sapphire boules [35]. Later Schmid established Crystal Systems, Inc. accompany around this technology. HEM is one of the most mature methods to grow large size and high quality sapphire crystals, the modern implementation of Schmid and Viechnicki's heat-exchanger method at Crystal Systems in Salem, Massachusetts.

Sapphire seed crystal is placed at the bottom of a molybdenum crucible which is then loaded with pure alumina crackle, product of Verneuil process. The furnace is evacuated and resistively heated to melt the crackle while keeping the seed just below its melting point by passing helium gas through the heat exchanger beneath the center of the crucible. Heat and vacuum help purifying the alumina of vaporizing some impurities. After partial melting of the seed, helium flow is increased to cool the seed and initiate crystallization of sapphire onto the seed. The furnace is kept at constant temperature during growth, which proceeds out from the seed in 3 dimensions. After complete crystallization, the furnace temperature and the helium flow are decreased and the boule is slowly annealed. During all the growth procedure from material melting, crystal nucleation and until the solid-liquid interface cover completely the surface of the melt, the temperature of melt is just higher 5-10°C than the melting point of material. After the solid-liquid interface reached to the wall of crucible, the temperature decreases gradually to room temperature. During the whole growth process, the melt temperature is adjusted by regulating the furnace temperature; the heat of graphite heater goes through the melt, crystal, heat exchanger and was finally carried off by helium flow. The seed and crucible don't move, the driving force of crystal growth come from the temperature gradient of solid-liquid interface. By 2001,

sapphire crystals up to 34 cm diameter, 65 kg were grown in production using HEM method [36], the grown sapphire boules are removed from the crucible. By 2003, larger 380-mm diameter, 84-kg sapphire boules were produced by HEM method [37].

1.6.8 Laser-heated pedestal growth (LHPG)

Laser-heated pedestal growth (LHPG) is applicable to grow fiber single crystal. The first sapphire fiber was grown by EFG techniques [38]. LHPG is a specific application of floating zone technique, belongs to crucible-free method. The main characteristic of this method is the diameter of poly crystal low melted is much bigger than the seed and the grown single crystal, only the center part of feeding rod is melted. A CO_2 laser beam creates a molten zone on the top of the source rod. The seed crystal is dipped into the molten zone and slowly withdrawn, pulling the growing crystal from the melts. Simultaneously, the source rod is pushed upwards into the molten zone so as to maintain its volume constant (figure 1.10). LHPG can be used to grow very high temperature melting point materials. Because only a part of feeding rod needs to be heated. Both powerful arc lights and lasers beam can be used as heating source, but usually CO_2 laser is more popular. The great advantage of this method is the absence of crucible, which is helpful to limit the contamination problem.

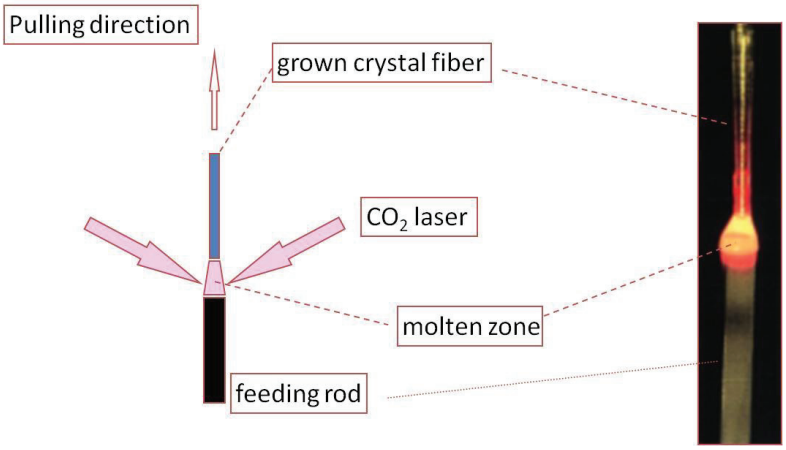

Figure 1.10 The principle of LHPG method

1.6.9 Micro-pulling down (μ-PD)

The pulling down technology as a growth process (also based on the Stepanov concept) has been available since 1976. Ricard et al. [39] originated this technology and used the process to grow sapphire plates, Si sheets and NaCl fibers. The single crystalline fiber grown by the micro-pulling down (μ-PD) method, shown in figure 1.11, have been established at Fukuda Laboratory of Tohoku University [40] since 1992 in the frame work of the "micro crystal project". This method is described for the first time by Yoon and Fukuda [41], Lebbou et al. [42] and Lee et al. [43] have developed a large range of single-crystalline and polycrystalline fibers from congruent and noncongruent melts. These researchers had worked together under the umbrella of a fundamental and applied research program in Fukuda's laboratory in Japan.

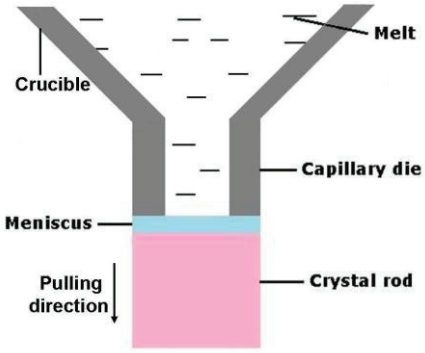

Figure 1.11 Principle of μ-PD method

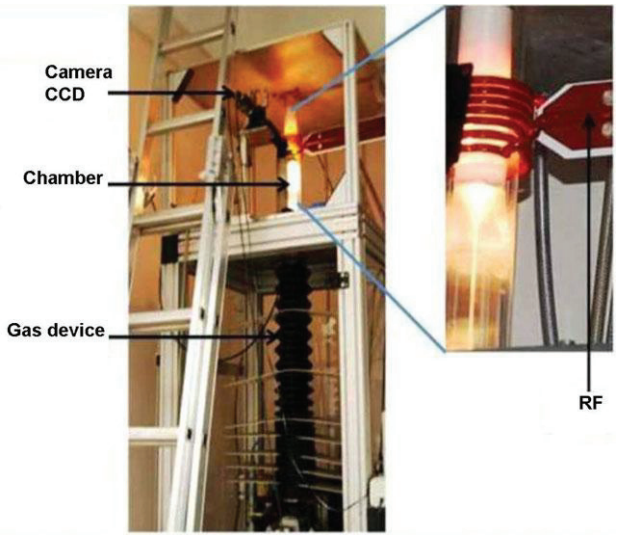

Figure 1.12 Apparatus of μ-PD developed by K. Lebbou in ILM laboratory

Figure 1.12 shows the apparatus of μ-PD developed by K. Lebbou in ILM laboratory. The raw material is melted in an iridium crucible, and thereafter the melt is pulled down continuously through a capillary channel made at the bottom of the crucible. The used die has cylindrical geometry，the liquid flow through the channel.

The diameter (φ) and the height (h) of the capillary die were strongly

dependent on the liquid proprieties following the Jurin law ($h =(4\sigma)/ (\varphi\rho g)$), where σ is superficial tension, ρ is liquid density, and g is gravitational acceleration. Iridium after heater and alumina ceramic insulation installed around the hot zone have been used to control thermal gradients in the case of Ir crucible. To visualize the melt meniscus and the growing crystal with a CCD camera is used. The crystals are grown in argon atmosphere to protect the crucible from oxidation and damage. The temperature distribution in the melt and the capillary die is measured by an Ircon pyrometer. Seed has been dipped into the melt at the bottom of the crucible in the capillary channel, and the melt temperature is adjusted to obtain the desired meniscus shape, the seed is pulled down continuously with a proper pulling rate.

1.7 The defects in sapphire crystals

Crystals with ideal and periodic arrangement of atoms or ions do not exist; there are always some defects in real crystals over the temperature of 0-K. Anything makes a deviation from the ideal state of crystals can be called "defects", these defects affect not only intrinsic properties of materials but also other physical and chemical characteristics. Defects can be classified into four types according to their geometry configurations: point defects, line defects, face defects and body defects.

- Point defects--- the dimension of defects stays on the order of magnitude of atoms, all three-dimensional size is very small, the breakage of crystal lattice caused by point defects occurs in one or several lattice constants. Vacancies, interstitial atoms and impurities belong to point defects; this kind of defects is usually due to thermal fluctuation also called thermal defects, including Schottky defect and Frankel defect. Color center is a common vacancy defect caused by non-stoichiometric ratio.

- Line defects--- the defects caused by the deviation on one-dimensional direction from periodic and regulatory arrangement of crystals, viz. the dimension of defects is long in one dimension but short in the other two dimensions. The typical line defect is dislocation, which arises from the

plastic deformation caused by stress exceeding elastic limitation.

- Planar defects--- the breakage of periodic arrangement is around a face in the crystal, the common planar defects include twins and stacking faults, small and large angle boundaries, grain boundaries, antiphase boundaries and domains etc.

- Volume defects--- the dimension of defects is big along the three-dimensional directions. The inclusions can be solid grains from the excessive elements of materials, impurities carried by the crucible during growth process. The volume defects significantly damage crystal qualities. They will result in light scattering, or decrease the intensity of light due to absorption of light. Besides, usually the thermal expansion coefficient of inclusions is different from the crystal, the stress produced during cooling period in growth process will induce large quantity of dislocations.

At the early stages of crystal growth development, crack and inclusions are common macroscopic defects in single sapphire crystals grown from the melt. Cracking is one of the main defects of large size sapphire crystal. It is divided into stress cracking and polycrystalline cracking, the crystal with stress is also easy to crack along cleavage plane during drilling rod process. The impurity elements of Al_2O_3 raw material and crucible material, as well as tungsten, molybdenum fragments from the crucible, heating unit and insulations will form inclusions in the crystals. Due to the impurity discharging phenomenon, impurities in the raw materials discharge to the edge, and impurities in the crucible diffuse to the centre. These impurities precipitate when the concentration exceeds the saturated concentration in the melt, forming inclusions. Therefore, high purity of Al_2O_3 raw material, crucible material and insulation material are important to grow high quality sapphire crystal. After the long-term efforts by many researchers of synthetic crystals, growth apparatus and techniques are all improved greatly nowadays, the above macroscopic defects such as cracking, inclusions and sub-grain boundaries can be generally avoided by usage of appropriate growth parameters. However, large numbers of

bibliographics have been published on microscopic defects e.g. color centers, dislocations, it is still difficult to eliminate these defects thoroughly. Especially for micro bubbles, which are common defects in sapphire crystals and very harmful to optical qualities, but there are no accordant theories around their origin, location, nucleation, and transport mechanism until now, no efficient and economic means to eliminate micro bubbles completely also.

1.7.1 Color center

Color center is a typical vacancy defect in single crystals caused by nonstoichiometric ratio, this kind of vacancies can absorb visible light and make the transparent crystal present color. The most simple color center is F center, which is formed by an anionic vacancy with a bounded electron in ionic crystals. The coloring principle of F center is excessive alkali metal atoms get inside the crystal and occupy the positions of alkali metal lattice, there are corresponding number of anion vacancies appear in the crystal to keep electric neutrality. At the same time, alkali metal atoms at the lattice positions are ionized, the lost electrons are bounded by positively charged anion vacancies. The configuration of F center is similar with hydrogen atom, so the electron energy state of F center can be roughly described by hydrogenic model, the absorption of F band is due to the transition of electron from ground state (1s state) to the first excited state (2p state). In this case, vacancies are seemed as traps of electrons, for the sake of simplicity, the size of electron is taken as the width of trap, the lattice constant of ionic crystal is supposed to be a, the width of trap is a/2, according to quantum mechanics the bound electron energy is

$$En = \frac{\pi^2\hbar^2 n^2}{8m(\frac{a}{2})^2} = \frac{\pi^2\hbar^2 n^2}{2ma^2} \tag{1.2}$$

Where m is the electron mass, n is integer, the absorption energy of electron transition from ground state to the first excited state is

$$\hbar\omega = \frac{3\pi^2\hbar^2}{2ma^2} \tag{1.3}$$

in the formula ω is the frequency of the photon absorption, it is inferred from the

formula that the wavelength of absorption light is in direct proportion with the square of lattice constant $\lambda \propto a^2$.

The opposite color center to F center is V center, when alkali halide crystals are heated in excessive halogen steam, a great deal of halogen will get inside the crystal, to maintain electric neutrality, cation vacancies appear and form into negative electricity centers, the system composed by negative electricity center and a positively charged hole is V center.

The common vacancy defects in sapphire crystals are F-type centers. Due to the formation energy (3.5 eV) of O^{2-} vacancies is smaller than that of Al^{3+} vacancies (9.1 eV) and Al^{3+} interstitial ion (10.8 eV), the migration energy (2.9 eV) of O^{2-} vacancies is smaller than that of Al^{3+} vacancies ($\perp$c 3.8 eV, //c 6.6 eV) and Al^{3+} interstitial ion (5 eV), so a high concentration of oxygen vacancies created in sapphire crystals [44]. When these O^{2-} vacancies capture two or one electrons, they form F or F^+ centers, if F^+ centers continue to capture two or one electrons, they form F_2 and F_2^+ centers:

O^{2-} vacancy + e^- → F^+ center ; F^+ center + e^- → F center ; F center + e^- → F_2^+ center ; F_2^+ center + e^- → F_2 center

Lee and Crawford studied luminescence of the F and F^+ centers in sapphire[45, 46], they proposed F^+ center and F center are responsible for the 4.8 and 6.1 ev absorption bands respectively. They observed an F-center emission band (3 ev) upon exciting with F light (6.1 ev) and the 3.8-ev F^+-center luminescence by exciting into 4.8-ev F^+ band during the 6.1 ev excitation circle, they conclude that the 3.8 ev emission originates with F^+ centers created by F^-center ionization. After the 204 nm absorption band of sapphire single crystals was first observed by Levy and Dienes [47], electron-bombardment [48], ion-implantation [49] and neutron-bombardment [50] can produce the defects responsible for this band. It is found that neutron irradiation or subsequent ionizing radiations such as gamma irradiation also can create it [51]. Turner and Crawford indicated the 204 nm band is due to an electron trapped at some defect produced by atomic-displacement processes [52]. Oscillator strength

ratio and the close and reciprocal relationship between 204 nm band and 254 nm band of neutron-bombarded Al_2O_3 single crystals indicate the former is associated with F (an oxygen- ion vacancy occupied by two electron) centers [53]. Lee and Crawford suggested that this band also can be introduced by heating Al_2O_3 single crystals at 2000°C in a graphite crucible [54]. The 204 nm band presented in the TGT grown sapphire crystal further substantiates the F-center model. In 2006, Guoqing Zhou et al. studied color center defects of a sapphire crystal grown by temperature gradient techniques (TGT) [55], they proposed a prominent 204 nm absorption band of the as-grown sapphire which doesn't appear in Al_2O_3 single crystals grown by Czochralski (Cz) method. It can be attributed to the formation of O^{2-} vacancies under strongly reducing atmosphere, the result of this band further substantiate the F-center model. Two relatively weaker bands absorbing at 229 nm and 255 nm were ascribed to F^+ centers.

Color centers strongly affect the transparency, homogeneity and optical properties such as absorption, and transmission. Researchers made efforts to eliminate this kind of defects in sapphire crystals. For the elimination of color centers, Lee and Crawford [45] think the thermalchemically introduced F centers are stable up to 1400°C and annealing in air or oxygen is necessary. Some type of inward diffusion process involving the oxygen is also useful. In 2002 a proprietary two-step post-growth thermal annealing was used to eliminate color centers in sapphire crystals [56]. It is understood that the origin of the pinkish color in the as grown sapphire crystals is caused by contaminations of Ti^{3+} from raw material and carbon from furnace, which causes oxygen vacancies and thus form F and F^+ centers. After annealing in O_2 or air, sample turns brownish, because of strong oxidation of carbon, but $Ti^{3+} \rightarrow Ti^{4+}$. After annealing in H_2, the carbon contamination is eliminated as hydrocarbon and Ti ions remain as Ti^{4+}, which compensate oxygen vacancies, thus eliminates color centers. It should be noted that color centers are not only damaged to sapphire crystals, they are beneficial on the other hand. For example, people utilize color centers to make sapphire presenting different colors, also colored sapphire is

used for jewery; furthermore, special sapphire crystals with color centers are material to fabricate lasers.

1.7.2 Dislocations

Dislocation is one of the common microscopic defects in the sapphire crystals. In 1934 British physicist G. I. Taylor realised the theory of dislocations developed by Vito Volterra in 1905 with Michael Polanyi and Egon Orowan for explaining plastic deformation of ductile materials. There are two elementary types of dislocations: when the dislocation line is vertical with glide direction, it is called edge dislocation; when the dislocation line is parallel with glide direction, it is called screw dislocation. In the case of the dislocation line is neither parallel nor vertical with the glide direction, the atom arrangement is between screw and edge dislocations, so it is called mixed dislocation. The glide plane of dislocations is defined by Burgers vector and dislocation line. Burgers vector of a dislocation line is constant. For a dislocation line, it is possible to form a loop inside the crystal or terminate on the surface, but it is forbidden to terminate in an integrated crystal. The dislocation density means the total length per unit volume.

The researchers studied dislocations in sapphire crystals mainly focused on the deformation principles and the relations with other motions during the past decades. Some geometrical relations in dislocated crystals are reported by J. F Nye [57], the author explains the observation of the c-axes in bent crystals of corundum are straight lines. M. L Kronberg [58] studied the plastic deformation sapphire single crystals. Basal slip and basal twinning in sapphire (α-Al_2O_3) had been an area of much interest and were investigated by many researchers [59,60,61].

Dislocation etch pits in [0001] orientation sapphire crystals grown by Cz method were observed using environmental scanning electron microscopy (ESEM) and SEM analysis. The dislocation density were measured at the same time [62]. Xin-huan et al. studied the dislocation etch pits [63] in Cz-sapphire crystals by SEM, using KOH and NaOH etchants at high temperature. Pletka et al. [64] studied the

dislocation substructures in sapphire (α-Al_2O_3) doped with isovalent (Cr^{3+} and Ti^{3+}) and aliovalent (Ti^{4+} and Mg^{2+}) solutes and deformed by basal slip at 1500–1520°C by transmission electron microscopy.

1.7.3 Bubbles defect

Quite often in sapphire crystal, microscopic and macroscopic bubbles can be observed. They degrade the optical properties and the laser efficiency by reduction of the transparency, they induce surface defects during substrate polishing processes and they are nucleation sites for cracks [65]. Small bubbles also known "micro-voids", usually have a diameter range from several μm to dozens of μm, some large bubbles even have diameter of hundreds of μm [66]. They belong to the category of "gaseous inclusions", a kind of volume defect. If the crystal is transparent enough, under strong light, the small bubbles can be observed distinctly by naked eyes.

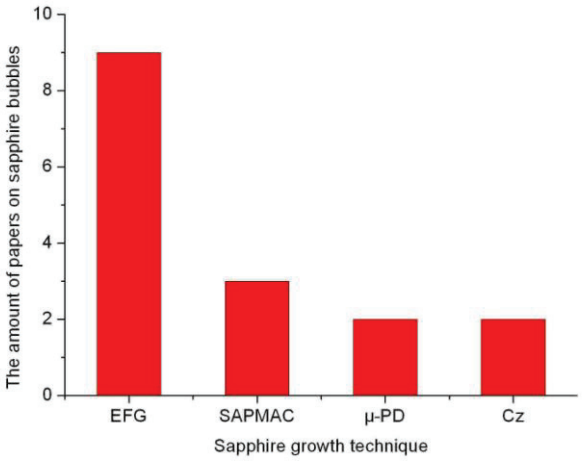

Figure 1.13 The amount of papers related to bubbles defect in sapphire growth by various techniques

Since long time ago, the researchers started studying the bubbles defect. However, up to now there is no complete and convincing theories to explain this common defect. Figure 1.13 presents the amount of papers discussed about bubbles of sapphire grown by different methods. There are 9 papers discussed about bubbles of sapphire grown by EFG technique, 3 papers by sapphire growth technique with micro-pulling and shoulder-expanding at cooled center (SAPMAC), 2 papers by μ-PD

and 2 papers by Cz technique. In 1995, T. Fukuda [67] reported the behaviour of bubble entrapment in Ti-doped Al_2O_3 single crystals grown by the Czochralski method, they studied the defects of crystal growth conditions such as the crystal rotation rate and kinds of growth atmosphere. On bubbles project, K. Lebbou team in ILM in France is one of the main teams working on bubbles of sapphire crystals, the two papers on bubbles of sapphire grown by Cz technique in figure 1.22 were published by K. Lebbou team. We can say, before the work of this thesis, the bubbles research of bulk sapphire crystals grown by Cz is blank, that is the challenge of this thesis. Although the papers on bubbles in sapphire crystals have been published by different research group, used different growth machines, with different heating systems, different growth atmospheres, their conclusions are often inconsistent and contradictory, but from the analyses of these literatures, we can still find some common regulations of bubbles in sapphire crystals.

1.7.3.1 The origin of bubbles

There are mainly four hypotheses to explain the origin of the bubbles:

- Growth atmosphere. Crystal growth processes are generally carried out in high purity inert atmosphere such as Ar, He, H_2 and N_2, it inevitably contains some oxygen and water. An imperfectly sealed growth chamber or incomplete vacuum of gas before the charge is melted can also increase the amount of gas. It was observed that, if the growth process occurs under vacuum, the density of the micro-bubbles is 2 or 3 times less than the density of the micro-bubbles in crystals grown in argon and even ten times less when the growth atmosphere is helium [66]. Fukuda [67] obtained crystals of sapphire doped with titanium without bubbles in helium atmosphere using the Czochralski method. E.A. Ghezal obtained sapphire fibers free of bubbles by the Micropulling Down (μ-PD) Technique with argon protective atmosphere and low pulling rate ($V \leq 0.25$ mm/min) [68].
- Dissolved gas as an initial component in the raw material. There are usually

three sources of alumina to obtain the sapphire single crystals: powder, cracked crystals or microballs (a new raw material provided by Le Rubis S.A., France), people can choose one or more of them as raw material according to the requirements. It is quite obvious that more higher quality of the initial feed material can get better quality of single crystals.

- Thermal decomposition of molten alumina. Molten alumina dissociates near the overheated walls of the crucible and the resulting gas inclusions are captured at the crystallization interface, O.M. Bunoiu [66] summarized the development of this theory. The composition of aluminum oxide melt strongly depends on the temperature in the crucible and the molten zone [69]. At low melt overheating temperature T<2100°C, the following dissociation reactions were occurred:

$$Al_2O_3 \rightarrow AlO_2 + AlO$$

$$2Al_2O_3 \rightarrow Al + 3AlO_2$$

At more significant overheating temperature T≈2100°C, the following reactions may be possible:

$$2AlO_2 \rightarrow 2AlO + O_2$$

$$2Al_2O_3 \rightarrow 2Al_2O_2 + O_2$$

$$Al_2O_3 \rightarrow Al_2O + O_2$$

$$Al_2O \rightarrow AlO + Al$$

At the overheating temperature T>2150°C, the following reactions are also possible:

$$2Al_2O_3 \rightarrow 4Al + 3O_2$$

$$2AlO \rightarrow 2Al + O_2$$

$$AlO_2 \rightarrow Al + O_2$$

- Reaction among the molten alumina, the crucible, and the graphite

devices--- Borodin et al. [70] concluded the molten alumina which is contaminated by impurities reacts with the crucible and the molybdenum die more actively than pure alumina. Jindra [71] reported molybdenum is dissolved in molten alumina and this process is accelerated in the presence of oxygen in the growth atmosphere. The composition of gas inclusions in the melt and in sapphire crystals was studied using mass spectrometry by Borodin et al. [72]. The presence of carbon and its compounds. The nitrogen and dissolved argon were found in the crystallized melt, a clear indication of the origin of carbon in the bubbles. All the chemical reaction equations are listed as follows:

$$Al_2O_3(l) \rightarrow Al_2O(g) + 2O(g)$$

$$Mo(s) + O(g) \rightarrow MoO(g)$$

$$2Mo(s) + 3O_2(g) \rightarrow 2MoO_3(g)$$

$$Mo(s) + Al_2O(g) \rightarrow MoO(g) + 2Al(g)$$

$$2Wo(s) + 3O_2(g) \rightarrow 2WO_3(g)$$

$$O(g) + C(s) \rightarrow CO(g)$$

$$Al_2O(g) + C(s) \rightarrow CO(g) + 2Al(g)$$

$$3MoO + 5C \rightarrow Mo_3C_2 + 3CO$$

1.7.3.2 The size of bubbles

Ivantsov observed the appearance of two types of gas inclusions, characterized by different sizes. He concluded that inclusions of large size result of the dissociation of molten alumina [66]. Irina Nicoara considers the void diameter decreases as the pulling rate increases. The dependence of the bubbles radius on the pulling rate can be described by Vr^k = constant, where V is the pulling rate, r is the void radius and k is a constant (k = -2, 4 for the analyzed crystals) [73]. Ghezal [68] concluded the same regulations in sapphire rods grown by μ-PD technique. By increasing the pulling rate (V>1 mm/min), the diameter of the bubbles decreases. They observed different shapes

of bubbles: spherical and some elongated bubbles were along the growth direction at the higher pulling rate (figure 1.14a). H. Li [74] observed two kinds of spherical bubbles: the majority is of diameter about 10μm and a few of the diameter around 25 μm (figure 1.14b).

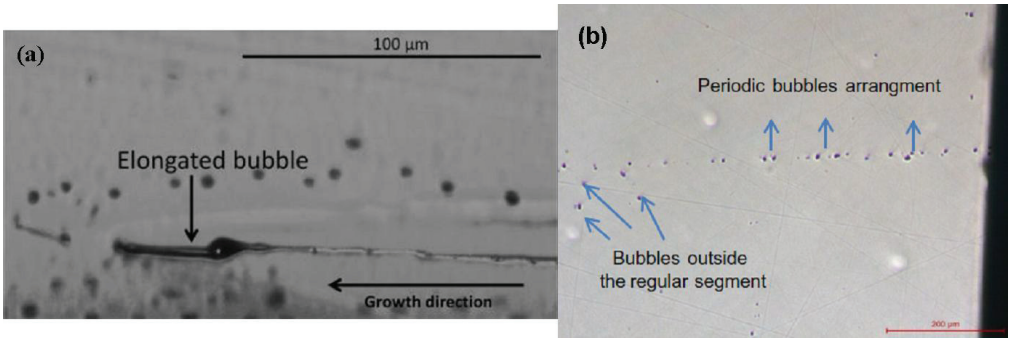

Figure 1.14 Different size of bubbles (a) spherical and elongated bubbles; (b) two kinds of spherical bubbles.

1.7.3.3 The distribution of bubbles

Usually the distribution of bubbles in sapphire crystals are impacted by many factors e.g. the equipment, the ambient atmosphere, the die shape, the raw material, the growth rate and so on, but after the attempt of lots of researchers, we can still find some common regulations of bubbles' distribution. For shaped sapphire crystals such as grown by EFG or μ-PD methods, gas inclusions' distribution depends on the velocity field of the melt flows in the meniscus viz. the melt between the top surface of the shaper and the crystallization front. Bunoiu [75] and Ghezal [68] all studied bubbles' distribution of sapphire rods, they concluded approximative regulations as a function of the pulling rate (figure 1.15). At low pulling rates, micro voids were arranged in a layer near the external face of the crystals and exhibited an almost uniform distribution, the bubbles are spherical and in general are generated in linear arrays along the pulling direction. At higher pulling rate, the bubbles are localized close to the lateral periphery of the rods forming a crown around the transversal section. When the pulling rate was increased further the crowns contain several layers of the bubbles that are irregularly distributed close to the periphery of the rod. At a

pulling rate greater than 2.5 mm/min, the smaller bubbles (φ≈1−6 μm) are observed in the volume and the core of the rod.

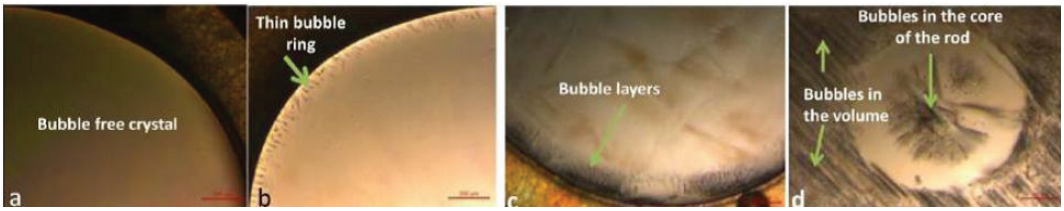

Figure 1.15 Bubbles' distribution in the cross section of the sapphire rod crystal as a function of the pulling rate (V) (a) v = 0.25 mm/min, (b) v =1 mm/min, (c) v = 1.5 mm/min, and (d) v = 2.5 mm/min [68].

In the case of Cz or Ky grown crystals, the available experimental data suggest that the gas inclusions generation depends on the forced convection in the melt and on the fluid flow in the meniscus. Researchers studied the bubbles distribution of the sapphire boule grown by Ky method examined by He-Ne laser. The bubble content is higher at the shoulder and center of the crystal, and the quantity and size of the bubble decrease on the equal diameter position [4]. When the crystallization rate is fast, the bubbles in the melt cannot be removed thoroughly, and bubble layer will form in the crystal. In Li's research [74], bubbles work in sapphire crystals grown by Cz method, the appearance (size, shape) of bubbles is slightly affected by the pulling rate which is different than sapphire shaped crystals growth. The statistical quantitative analysis of the bubbles distribution showed that the starting raw materials (powders, crackles) does not have any influence on the bubbles incorporated in sapphire crystals grown by Cz technique. The bubbles density increases apparently with the increasing of pulling rate, while the changes of rotation rate had no apparent effect on the size and the bubbles distribution.

1.8 Conclusion

Because of their excellent properties, sapphire crystals remain a strategic material for a large range of civil and military applications. To meet the requirements of sapphire market, the growth of large-size sapphire crystals is an important topic. The needed are large crystallization units that provide not only high perfection of the

crystals, but also quantity production. The use of such units essentially decreases consumption of both energy and materials, so the cost of the crystal diminishes. Based on this, attempts have been made to scale up the Cz, Bridgman, HEM, ky processes to grow large boules sapphire crystals.

Micro bubbles are almost always observed in sapphire single crystals, which decrease the properties of sapphire significantly. However, up to now, there is no complete and convincing theories to explain this common defect. The bubbles research of sapphire crystals grown by Cz method is still not well developed. In this chapter we have presented our overview about alumina and sapphire crystal growth technology. In addition we have shown the most defects which are observed in sapphire crystals. Whatever the growth method and the conditions, defects are quite often observed in the grown crystals, especially bubbles defect. We have shown the main hypotheses which describe the bubbles propagation.

References:

[1] "http://www.world-aluminium.org." .

[2] G. E. H. Ahmed, "Croissance cristalline de saphir non dopé préformé et étude des effets de la matière première et des vitesses de tirage sur la distribution des bulles et la qualité cristalline," PhD thesis, L'UNIVERSITE CLAUDE BERNARD LYON 1, 2013.

[3] Elena R. Dobrovinskaya, L. A. Lytvynov, and V. Pishchik, *Sapphire Material, Manufacturing, Applications*. Springer Science+Business Media, 2008.

[4] H. Tang, H. Li, and J. Xu, "Growth and Development of Sapphire Crystal for LED Applications," in *Advanced Topics on Crystal Growth*, 2013, pp. 307–333.

[5] "http://www.extremetech.com." .

[6] P. F. Moulton, "Spectroscopic and laser characteristics of Ti:$A1_2O_3$," *J. Opt. Soc. Am. B*, vol. 3, no. 1, pp. 125–133, 1986.

[7] K. F. Wall and A. Sanchez, "titanium sapphire lasers," *LINCOLN Lab. J.*, vol. 3, no. 3, pp. 447–462, 1990.

[8] S. Kück, "Laser-related spectroscopy of ion-doped crystals for tunable solid-state lasers," *Appl. Phys. B*, vol. 72, pp. 515–562, 2001.

[9] D. E. Spence, P. N. Kean, and W. Sibbett, "60-fsec pulse generation from a self-mode-locked Ti:sapphire laser," *Opt. Lett.*, vol. 16, no. 1, pp. 42–44, 1991.

[10] H. J. Scheel, "Histrical aspects of crystal growth technology," *J. Cryst. Growth*, vol. 211, pp. 1–12, 2000.

[11] "http://www.statista.com." .

[12] S. Senz, Pascal Kopperschmidt, and N. D. Zakharov, "Origin of Voids at the Interface of Wafer Bonded Sapphire on Sapphire," *Mat. Res. Soc. Symp. Proc.*, vol. 654, pp. AA3.19.1–5, 2001.

[13] H. E.Buckley, *Crystal growth*. New York: Wiley, 1951.

[14] J. J.Gilman, *The art and science of growing crystals*. New York: Wiley, 1966.

[15] W. R. Wilcox, "The influence of a temperature gradient on crystal faceting," *J. Cryst. Growth*, vol. 7, no. 2, pp. 203–208, 1970.

[16] E. Billig, "Some defects in crystals grown from the melt. I. defects caused by thermal stresses," *Proc. R. Soc. London A*, vol. 235, no. 1200, pp. 37–55, 1956.

[17] W. A. Tiller, "Theoretical analysis of requirements for crystal growth from solution," *J. Cryst. Growth*, vol. 2, no. 2, pp. 69–79, 1968.

[18] H. J. Scheel and T. Fukuda, *Crystal Growth Technology*. John Wiley & Sons Ltd, 2003.

[19] B. Cockayne, M. Chesswas, and D. B. Gasson, "Single-Crystal Growth of Sapphire," *J. Mater. Sci.*, vol. 2, no. 1, pp. 7–11, 1967.

[20] S. E. Demina, E. N. Bystrova, M. A. Lukanina, and et al., "Numerical analysis of sapphire crystal growth by the Kyropoulos technique," *Opt. Mater. (Amst).*, vol. 30, pp. 62–65, 2007.

[21] A. B. Chase and J. A. Osmer, "Localized cooling in flux crystal growth," *J. Amer. Ceram. Soc.*, vol. 50, pp. 326–330, 1967.

[22] H. S. Parker, "Vapor growth of Al_2O_3 bicrystals," *J. Amer. Ceram. Soc.*, vol. 53, no. 11, pp. 583–587, 1970.

[23] T. Duffar, *Crystal Growth Processes Based on Capillarity Czochralski, Floating Zone, Shaping and Crucible Techniques*. John Wiley & Sons Ltd, 2010.

[24] A. Verneuil, "Production artificielle du rubis par fusion," *Comptes Rendus Acad. Sci.*, vol. 135, no. 19, pp. 791–794, 1902.

[25] H. C. Theuerer, "Methode of processing semiconductive materials," 3060123, 1952.

[26] J. Czochralski, "Measurement of velocity of crystallization of metals," *Z. Phys. Chem.*, vol. 92, p. 219, 1917.

[27] B. Cockayne, M. Chesswas, and D. B. Gasson, "Single-crystal growth of sapphire," *J. Mater. Sci.*, vol. 2, pp. 7–11, 1967.

[28] S. Kyropoulos, *Z. Anorg. Chem.*, vol. 154, p. 308, 1926.

[29] H. E. J. LaBelle and A. I. Mlavsky, "Growth of controlled profile crystals from the melt: Part I - Sapphire filaments," *Mater. Res. Bull.*, vol. 6, no. 7, pp. 571–579, 1971.

[30] P. I. Antonov and V. N.Kurlov, "A REVIEW OF DEVELOPMENTS IN SHAPED CRYSTAL GROWTH OF SAPPHIRE BY THE STEPANOV AND RELATED TECHNIQUES," *Prog. Cryst. Growth Charact. Mater.*, pp. 63–122, 2002.

[31] P. I. Antonov and S. P. Nikanorov, "Physical problems in crystal growth by the Stepanov method," *J. Cryst. Growth*, vol. 50, no. 1, pp. 3–7, 1980.

[32] P. I. Antonov, "Shape and Properties of Crystals Grown from the Melt by the Stepanov Techniques," *Growth Cryst.*, vol. 13, pp. 198–207, 1986.

[33] P. W. Bridgman, "A Condensed Collection of Thermodynamics Formulas," *Harvard Univ. Press*, 1925.

[34] D. C. Stockbarger, *Rev. Sci. Instrum.*, vol. 7, p. 133, 1936.

[35] F. Schmid and D. Viechnicki, "Growth of Sapphire Disks from the Melt by a Gradient Furnace Technique," *J. Am. Ceram. Soc.*, vol. 53, p. 528, 1970.

[36] C. P. Khattak and F. Schmid, "Growth of the world's largest sapphire crystals," *J. Cryst. Growth*, vol. 225, pp. 572–579, 2001.

[37] C. P. Khattak, Paul J. Guggenheim, and Frederick Schmid, "Growth of 15-Inch Diameter Sapphire Boules," *Proc. SPIE*, vol. 5078, 2003.

[38] LaBelle Jr.H. E. and A. I. Mlavsky, "Growth of sapphire filaments from the melt," *Nature*, vol. 216, no. 574–5, 1967.

[39] Ricard, J. and C. Excoffon, patent, 4,233,338, 1980.

[40] P. Rudolph, "The virtues of Fukuda laboratory of crystal growth," *III-Vs Rev.*, vol. Elsevier 9, pp. 27–32, 1996.

[41] D. H. Yoon and T. Fukuda, "Characterization of $LiNbO_3$ micro single crystals grown by the micro-pulling-down method," *J. Cryst. Growth*, vol. 144, pp. 201–206, 1994.

[42] K. Lebbou and G. Boulon, "Oxide Fiber Crystals Grown by μ-PD and LHPG Techniques," *Fiber Cryst. Growth from Melt*, vol. 6, pp. 219–254, 2004.

[43] L. J.H., A. Yoshikawa, K. Lebbou, H. Kaiden, T. Fukuda, D. H. Yoon, and Y. Waku, "Microstructure of Y_2O_3 doped Al_2O_3/ZrO_2 eutectic fibers grown by the micro-pulling-down method," *J. Cryst. Growth*, vol. 231, no. 1–2, pp. 179–185, 2001.

[44] G. J. Dienes, D. O. Welch, C. R. Fischer, R. D. Hatcher, O. Lazareth, and M. Samberg, "Shell-model calculation of some point-defect properties in α-Al_2O_3," *Phys. Rev. B*, vol. 11, no. 8, pp. 3060–3070, 1975.

[45] K.H. Lee and J. J.H. Crawford, "Luminescence of the F center in sapphire," *Phys. Rev. B*, vol. 19, no. 6, 1979.

[46] K. H. Lee and J. J. H. Crawford, "Electron centers in single-crystal Al_2O_3," *Phys. Rev. B*, vol. 15, no. 8, pp. 4065–4070, 1977.

[47] P. W. Levy and G. J. Dienes, "Colour Centers Induced in Al_2O_3 by Reactor and Gamma-Ray Irradiation," in *Report of the Bristol Conference on Defects in Crystalline Solids,The Physical Society, London*, 1955, pp. 256–260.

[48] G. W. Arnold and W. D. Compton, "Threshold Energy for Lattice Displacement in α-Al_2O_3," *Phys. Rev. Lett.*, vol. 4, no. 2, pp. 66–68, 1960.

[49] G. W. Arnold, G. B. Krefft, and C. B. Norris, "Atomic displacement and ionization effects on the optical absorption and structural properties of ion implanted Al_2O_3," *Appl. Phys. Lett.*, vol. 25, no. 10, p. 540, 1974.

[50] B. Jeffries, G. P. Summers, and J. H. Crawford, "F center fluorescence in neutron‐bombarded sapphire," *J. Appl. Phys.*, vol. 51, no. 7, p. 3984, 1980.

[51] P. W. Levy, "Color Centers and Radiation-Induced Defects in Al_2O_3," *Phys. Rev.*, vol. 123, no. 4, pp. 1226–1233, 1961.

[52] T. J. Turner and J. J. H. Crawford, "Nature of the 6.1-eV band in neutron-irradiated Al_2O_3 single crystals," *Phys. Rev. B*, vol. 13, no. 4, pp. 1735–1740, 1976.

[53] K. H. Lee and J. J. H. Crawford, "Electron centers in single-crystal Al_2O_3," *Phys. Rev. B*, vol. 15, no. 8, pp. 4065–4070, 1977.

[54] K. H. Lee and J. H. Crawford, "Additive coloration of sapphire," *Appl. Phys. Lett.*, vol. 33, no. 4, p. 273, 1978.

[55] G. Zhou, Y. Dong, J. Xu, H. Li, J. Si, X. Qian, and X. Li, "Φ140 mm sapphire crystal growth by temperature gradient techniques and its color centers," *Mater. Lett.*, vol. 60, pp. 901–904, 2006.

[56] B. C. Barish, G. Billingsley, J. Camp, W. P. Kells, G. H. Sanders, S. E. Whitcomb, L. Y. Zhang, R.-Y. Zhu, P. Z. Deng, J. Xu, G. Q. Zhou, and Y. Z. Zhou, "Development of Large Size Sapphire Crystals for Laser Interferometer Gravitational-Wave Observatory," *IEEE Trans. Nucl. Sci.*, vol. 49, no. 3, pp. 1233–1238, 2002.

[57] J. Nye, "Some geometrical relations in dislocated crystals," *Acta Metall.*, vol. 1, no. 2, pp. 153–162, 1953.

[58] M. Kronberg, "Plastic deformation of single crystals of sapphire: Basal slip and twinning," *Acta Metall.*, vol. 5, no. 9, pp. 507–524, 1957.

[59] J. B. Bilde-Sørensen, B. F. Lawlor, T. Geipel, P. Pirouz, A. H. Heuer, and K. P. D. Lagerlo¨f, "On basal slip and basal twinning in sapphire (α-Al_2O_3)—I. Basal slip revisited," *Acta Metall.*, vol. 44, no. 5, pp. 2145–2152, 1996.

[60] J. Castaing, A. Muñoz, D. G. Garcia, and A. D. Rodriguez, "Basal slip in sapphire (α-Al_2O_3)," *Mater. Sci. Eng. A*, vol. 233, no. 1–2, pp. 121–125, 1997.

[61] A. H. Heuer, K. P. D. Lagerlöf, and J. Castaing, "Slip and twinning dislocations in sapphire (α-Al_2O_3)," *Philos. Mag. A*, vol. 78, no. 3, pp. 747–763, Sep. 1998.

[62] J. Xiao, S. Yinb, M. Shao, and X. Zhang, "Observation of dislocation etch pits in a sapphire crystal grown by Cz method using environmental SEM," *J. Cryst. Growth*, vol. 266, pp. 519–522, 2004.

[63] N. Xin-huan, L. Guo-qi, Z. Wei-lian, G. Jin-yong, and L. Yu-ling, "Dislocation of Cz-sapphire substrate for GaN growth by chemical etching method," *Trans. Nonferrous Met. SOC. China*, vol. 16, pp. s187–s190, 2006.

[64] B. J. Pletka, T. E. Mitchell, and A. H. Heuer, "Dislocation substructures in doped sapphire (α-Al_2O_3) deformed by basal slip," *Acta Metall.*, vol. 30, no. 1, pp. 147–156, 1982.

[65] F. Theodore, T. Duffar, S. J.L., J. Pesenti, M. Keller, P. Dusserre, F. Louchet, and V. Kurlov, "Crack generation and avoidance during the growth of sapphire domes from an element of shape," *J. Cryst. Growth*, vol. 204, no. 3, pp. 317–324, 1999.

[66] O. M. Bunoiu, T. Duffar, and I. Nicoara, "Gas bubbles in shaped sapphire," *J. Cryst. Growth*, vol. 56, pp. 123–145, 2010.

[67] T. Fukuda, Y. Okano, N. Kodama, F. Yamada, S. Hara, and D. H. Yoon, "Growth of bubble-free Ti-doped Al_2O_3 single crystal by the czochralski method," *Cryst. Res. Technol.*, vol. 30, no. 2, pp. 185–188, 1995.

[68] E. A. Ghezal, H. Li, A. Nehari, G. Alombert-Goget, A. Brenier, K. Lebbou, M. F. Joubert, and M. T. Soltani, "Effect of Pulling Rate on Bubbles Distribution in Sapphire Crystals Grown by the Micropulling Down (μ-PD) Technique," *Cryst. Growth Des.*, vol. 12, no. 8, pp. 4098–4103, Aug. 2012.

[69] A. Nehari, "Etude et caractérisation de la synthèse de milli-billes d'alumine alpha et de la cristallogène du saphir pur et dopé titane (Ti^{3+})," PhD thesis, Claude Bernard Lyon 1 University, 2011.

[70] V. A. Borodin, T. A. Steriopolo, V. A. Tatarchenko, and T. N. Yalovets, "Control over gas bubble distribution in shaped sapphire crystals," *Cryst. Res. Technol.*, vol. 20, no. 3, pp. 301–306, 1985.

[71] J. Jindra, J. Filip, and B. Mánek, "Multiple growth of profiled sapphire crystals," *J. Cryst. Growth*, vol. 82, no. 1–2, pp. 100–105, 1987.

[72] V. A. Borodin, T. A. Steriopolo, V. A. Tatarchenko, L. I. Chernyshova, and T. N. Yalovets, "Production of sapphire tubes for high-pressure sodium lamps using the stepanov method at high rates of growth," *Cryst. Res. Technol.*, vol. 20, no. 2, pp. 159–166, 1985.

[73] I. Nicoara, O. M. Bunoiu, and D. Vizman, "Voids engulfment in shaped sapphire crystals," *J. Cryst. Growth*, vol. 287, pp. 291–295, 2006.

[74] H. Li, E. A. Ghezal, A. Nehari, G. Alombert-Goget, A. Brenier, and K. Lebbou, "Bubbles defects distribution in sapphire bulk crystals grown by Czochralski technique," *Opt. Mater.*, vol. 35, no. 5, pp. 1071–1076, Mar. 2013.

[75] O. M. Bunoiu, I. Nicoara1, J. L. Santailler, F. Theodore, and T. Duffar, "On the void distribution and size in shaped sapphire crystals," *Cryst. Res. Technol.*, vol. 40, no. 9, pp. 852–859, 2005.

Chapter II

Experiment process & technical methods

2.1 Czochralski(Cz) technique

2.2 Characterization techniques

2.3 Conclusion

References

Sapphire and Ti-sapphire bulk crystals were grown by Cz technique respectively, bubbles defects were investigated in the as grown crystals. To study the influence of growth parameters on bubbles, sapphire and Ti-sapphire crystals were grown with different pulling rate and rotation rate, two kinds of seeds: a-axis $[10\bar{1}2]$ and r-axis $[11\bar{2}0]$ were used. To characterize the bubble defect and optical properties, the as grown crystals were cut into wafers with different thickness perpendicular to the growth direction, then optically polished.

In this chapter, the principle of Cz technique and the growth process are introduced, the technical methods and equipments used in experiments to characterize the crystals are presented. The characterization are mainly: the quality of the crystals, the bubbles characterization, the impact of the bubbles on the crystal optical properties. The technique route of this research is schematically shown below (figure 2.1):

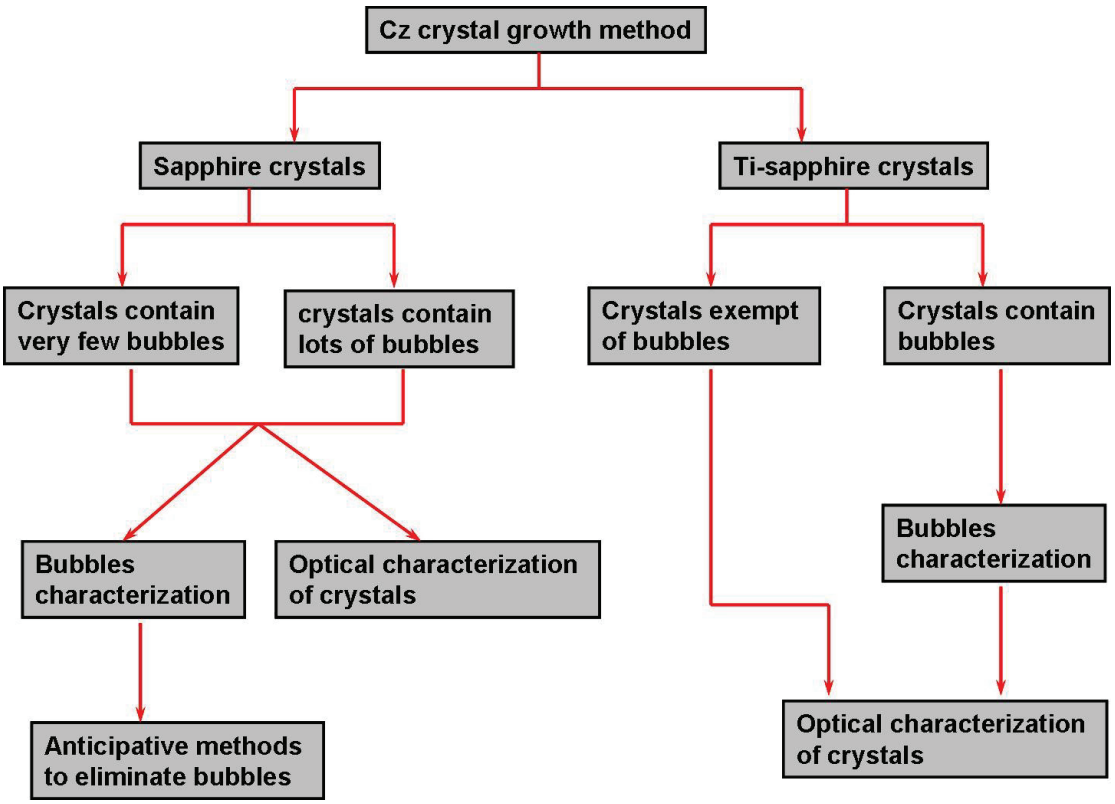

Figure 2.1 Technical route of the thesis

2.1 Cz crystal growth technique

The essential advantages of the Cz method provided its prevalence over other methods. Besides, its primary technical characteristics are common foundations of all the pulling methods. The principal advantages of Cz method are [1]:

- The whole growth situation can be observed conveniently during all the process.
- The growth rate is high and growth cycle is short.
- The crystal is grown at the surface of melt and keeps instance with the crucible, which can not only decrease the thermal stress but also prevent the parasitic nucleation from the wall of crucible.
- There is the possibility of the crystal withdrawal from the melt at any level of crystallization, which is very important while determining the single crystal growth conditions.
- Cz method permits to pre-set the geometrical form of the growing single crystal by varying the melt temperature and pulling rate, which as well as the seeding and necking down techniques can decrease dislocation density greatly and get crystals of high integrity.

The disadvantage of Cz method is that for its realization a crucible is required, which can be a source of impurity. Besides, crystal rotation will cause interaction of natural convection and forced convection, the complicated convection effect makes Cz process dynamics and control design more difficult, the researchers attempt a lot recently to understand the influence of convection and temperature field to the quality of crystals. C.J. Jing [2] studied effect of meniscus shape in Cz crystal growth by global analysis with a model of three-dimensional of heat transfer, it was found that the meniscus of the melt free surface caused the melt flow to be more unstable and shifted the critical Reynolds number at which the melt/crystal interface inversion occurs toward a much lower value. S.E. Demina [3] and Haisheng Fang [4] all studied

effect of heat transfer, fluid flow, convection and interface shape during sapphire crystal growth by Cz method by an integrated mathematical model analysis with non-dimensional parameters, the dimensionless parameter Nσ denotes the relative strength of natural convection and Marangoni convection, and the interface becomes more convex as it increases. The RF coil position also has a definite influence on the transport processes during the stages of sapphire Cz crystal growth [5], the least input power is required and the temperature gradients along the crystal-melt interface are the smallest when the central position of the RF coil is placed 10mm below the central position of the melt inside the crucible during the growth process and the optimal power input for growing sapphire crystal can be achieved by adjusting the RF coil position below the central position of the melt. In next section several important growth conditions of Cz method are introduced.

2.1.1 Growth rate

The normal growth rate of the crystal-melt interface is essentially controlled by the rate at which the pull rod is raised−the "pull rate", here denoted by v_p. If conditions are arranged so as to grow a cylindrical crystal then the normal growth rate of a crystal growing with a planar crystal-melt interface (v) will be equal to the pulling rate v_p plus the rate of fall of the melt level in the crucible. The latter depends on the relative diameters of the crucible (assumed cylindrical) and the crystal. One can readily show that the growth rate is given by:

$$v = v_p\rho_L R^2/(\rho_L R^2 - \rho_s r^2) \quad (2.1)$$

where $\rho_{s,\,L}$ are the densities of crystal and melt, R and r are the radii of the crucible and crystal respectively. Thus, for a material with no volume change on solidification (equal densities), growth in a crucible which is twice the crystal radius occurs at a rate which is 33% grater than the pulling speed [6]. When the crystal radius is changing with time, the height of the supported meniscus is also changing and this makes an additional contribution to the growth rate.

To achieve the condition of steady growth with constant radius requires that the

net heat flow through the interface exactly balances the rate of evolution of latent heat due to the crystallization process. Again assuming for the moment a planar interface, this condition can be expressed simply as:

$$k_s G_s - k_L G_L = L_v \tag{2.2}$$

where $k_{s,\ L}$ are the thermal conductivities of crystal and melt, $G_{s,\ L}$ are the axial temperature gradients in the crystal and melt at the interface, L is the latent heat of crystallization per unit volume.

To summarize, the growth rate of the crystal is predetermined by the operator by the choice of pulling speed and relative diameters of crystal and crucible. The growth of a cylindrical crystal is obtained by careful adjustment of the heat flow conditions so as to maintain the heat flux balance at the interface.

2.1.2 Crystal rotation

Crystal rotation is also a significant merit of Cz technique. The principal reasons for rotating the crystal are twofold. The first is the pragmatic one that doing so helps to give the crystal the desired circular cross section. Without any rotation, the crystal will grow most rapidly in directions corresponding to minimum heat transport from the melt to the crystal so that, if the equipment does not have perfect thermal symmetry about a vertical axis coincident with the pulling axis, the crystal would wander off the pulling axis producing an object resembling the proverbial dog's hind leg. The second, more subtle, reason for imposing crystal rotation concerns the distribution of dopant (deliberately added solute) into the crystal. Without any rotation the solute distribution in the melt would be subject to the vagaries of the natural convection flow in the melt. This flow is driven principally by the buoyancy produced by the temperature field so that, again, if this lacks perfect symmetry about the pulling axis, the flow pattern will also lack such symmetry. The rotating crystal can establish a solute boundary layer ahead of it which has the property that its thickness is sensibly independent of radial position and thereby yields crystals having a radial uniformity of doping.

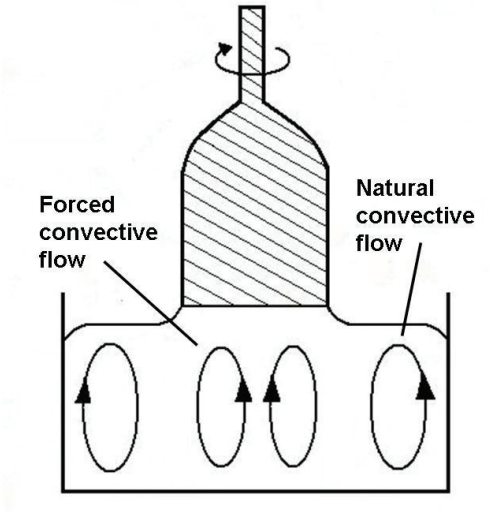

Figure 2.2 Schematic representation of natural and forced convective flow in Cz method

The flow in Cz crucible (shown in figure 2.2) is dauntingly complicated to elucidate. Natural convective flow includes Buoyancy-driven flow and Marangoni flow. Cz crucibles are usually heated from the side, the hot layer of fluid adjacent to the heated vertical crucible wall is made buoyant, rises and is then turned inwards rapidly at the melt surface. In the absence of crystal and crucible rotation, is carried around in a toroidal motion giving rise to a single "doughnut" circulation with fluid descending beneath the axis of the crystal. Marangoni convection is a capillary flow, named after the Italian physicist Carlo Giuseppe Matteo Marangoni (1840-1925). It is driven by the gradient of the surface tension at a free surface, which in turn results from temperature or concentration gradients. Crystal rotation will induce forced convective flow. The rotating crystal acts as a centrifugal fan sucking up fluid axially, spinning it up in a thin Ekman layer of thickness $(v/\Omega)^{1/2}$ and ejecting it tangentially (Ω is the crystal rotation rate). The rapidly outward flow due to the rotating crystal meets the rapidly inflowing fluid driven by the hot vertical crucible wall and downflow occurs at some radial distance which depends on the relative strength of the crystal flow and the buoyancy-driven convection. Several additional factors complicate this behavior. Firstly the radial temperature gradient across the melt surface will lead to a thermal-capillary component of flow. The description of this is complicated by the fact that the melt surface is not planar since the growing crystal

supports a liquid meniscus which is typically several millimeters in height. Secondly the loss of heat from the melt surface produces a destabilizing vertical temperature gradient in the upper region of the melt which can give rise to a further mode of convection.

2.1.3 The meniscus

The most important region in Cz crystal growth is the meniscus, the interconnection between melt and crystal. The meniscus and its shape result from gravitational forces and surface tension. At its upper end the so-called phase boundary, or interface is located. Here crystallization takes place and thereby heat of fusion (latent heat) is released. Because the crystal is pulled upwards into colder regions of the furnace a temperature gradient is established, which leads to a heat flow by conduction from the hot interface into the colder crystal. By this mechanism, crystallization is maintained throughout the growing process.

The amount of heat transported into the crystal consists of two components: the amount of heat transported from the meniscus region into the interface with radius r_c and the amount of heat released by crystallization. In general, the following relation holds for the vector $\vec{v}_c$ of the growth rate along the phase boundary described by z= Z(r), r $\in$ [0, r_c]:

$$\vec{v}_c(r,z(r)) = \frac{1}{\rho_s \Delta H}(\lambda_l \nabla T_l(r,z(r)) - \lambda_s \nabla T_s(r,z(r))) \quad r \in [0, r_c]. \qquad (2.3)$$

In this equation the specific latent heat is denoted by ΔH , the heat conductivities of the solid and the liquid are given by λ_s and λ_l , respectively, and $T_s(r, z)$ and $T_l(r, z)$ represent the temperature in the solid and the melt. The density of the crystal at the interface (at melting temperature T_i) is given by ρ_s. A necessary condition for growth is that the growth rate is positive, i.e. the heat flux is directed from the melt into the crystal. The changes in the temperature gradients on the liquid or solid side of the phase boundary lead to an immediate change of growth rate, as can be easily seen from Equation (2.3). On the one hand, a local change of growth rate

results in a deformation of the phase boundary, and in a change of the crystal diameter if this deformation is located at the rim of the interface. On the other hand, a change in interface geometry initiates a change in heat transport. This consideration leads to the conclusion that the demand to grow crystals of well-defined shape makes necessary exact control of thermal conditions in the interface region. This is quite complicated because of disturbances in heat transport (initiated by convection of gas and melt or changes of material properties during growth) as well as by the batch character of the process which causes an ever-changing heat input from the heaters. Furthermore, the shape of the meniscus strongly depends on the radius r_c of the crystal at the interface as well as on the growth angle α. This means that changes in the meniscus shape initiated by changes in geometry result in an immediate change of the heat balance in this region, with the consequences described above.

2.1.4 Cz crystal growth setup

In this thesis, Cz method was employed to grow undoped sapphire and Ti-doped sapphire single crystals respectively. The growth process by the Cz setup is shown in figure 2.3. In order to ensure the longitudinal temperature presents axial symmetrical distribution in the furnace, in installation of the furnace, the center of RF coil, the center of isolator system, the center of crucible and the center of seed should be kept at same axial position. To limit iridium crucible oxidation, the crystals were

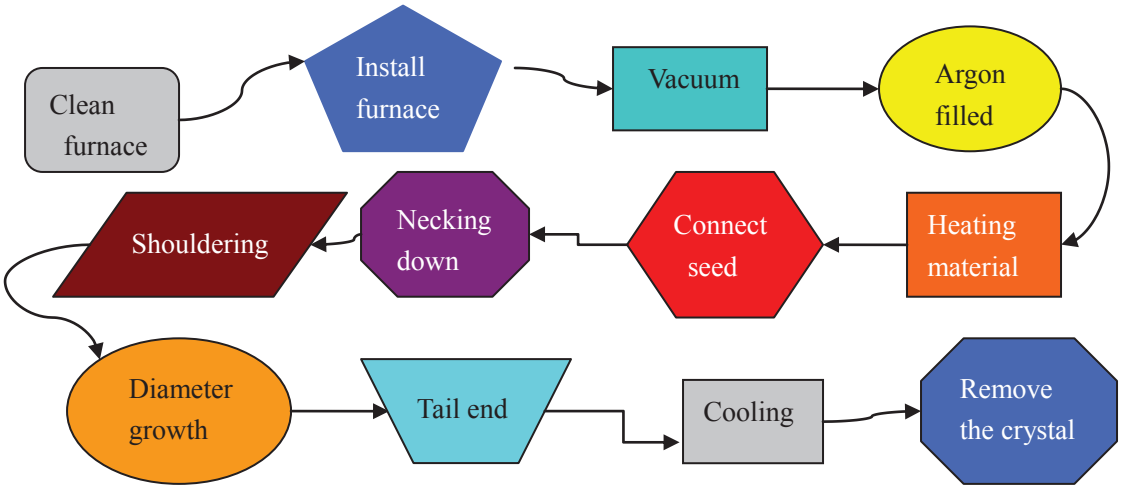

Figure 2.3 Cz growth process

grown in argon gas atmosphere.

First primary vacuum the furnace about one hour then fill with high purity argon to congruent pressure, start the heating power until all the raw material are melted, during this period keep the seed rotating to get a uniform temperature distribution in the furnace. After all material melted, observe the state of melt flow, adjust the power making the melt temperature close to melting point of sapphire and keep this temperature, descend the seed close to solid liquid interface and heat the seed for some time, connect the seed with the melt. To avoid the defects propagation from the seed to crystal, necking down technique is required, which is realized by slow heating technique. When the size of crystal decrease to needed, slow cooling is required for shouldering technique. When the crystal size extend to appropriate value, start isothermal growth i.e. diameter growth period.

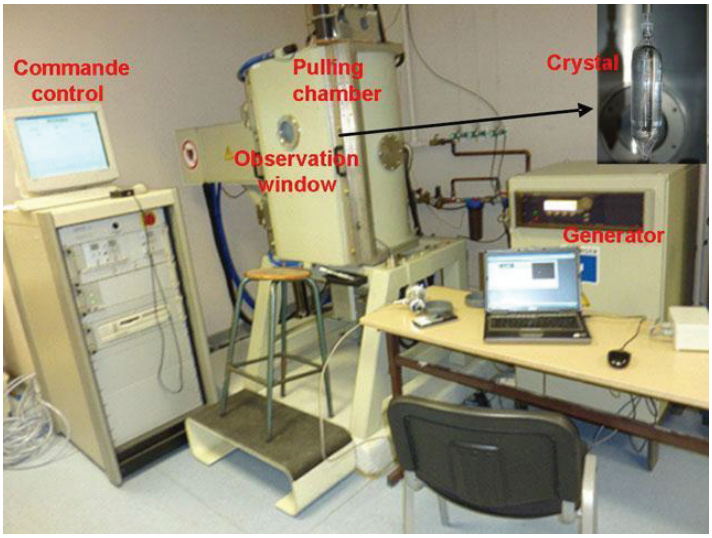

Figure 2.4 Cz growth technique used in the frame of this thesis

The preliminary growth line of solid-liquid interface is convex, so the fault zone and impurities are decreased even eliminated, then, the growth line becomes flat. After a definite length of diameter growth, increase the heating temperature making the crystal diameter decline to required size i.e. tail ending period. After, to avoid the cracks and other defects propogation, decrease the system temperature with a congruent rate to room temperature until the growth is finished. Figure 2.4 presents the growth system of Cz technique utilized in the thesis. Figure 2.5a shows the inside

status of the pulling chamber just after the growth process is finished, figure 2.5b illustrate some sapphire and doped sapphire single crystals grown by the Cz setup.

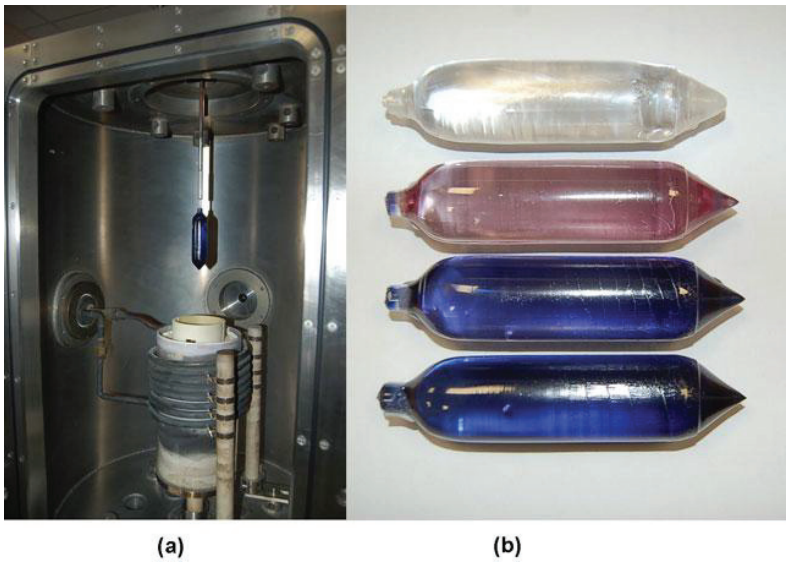

Figure 2.5 (a) the inside status of Cz chamber; (b) sapphire and doped sapphire single crystals grown by Cz method.

During growth process, a 60 mm-diameter iridium crucible was inductively heated and an automatic controlled diameter based on the time derivative of the crystal weight is used for all the growth process. A good thermal gradient was optimized and stable convection flow minimizes the fluctuation temperature which results in growing crystals under stationary stable state regime. Typical sapphire crystals weighted 250-400 g and were approximately 28-35mm in diameter and 90-110mm in length. Depending on the pulling rate, the average total process duration including crucible installation, charge melting, the growth and crystal cooling is about one week.

2.1.5 Cz crystal growth parameters

According to the principles of Cz technique and the growth experiences, the main growth parameters employed in this thesis, such as raw material, protective gas, growth rate, seed etc., are indicated in table 2.1 and discussed in the next section:

- Raw material---- For growing sapphire crystals, to meet the volume

requirement of the crystal size, alumina (α-Al_2O_3) powder and sapphire crackles were used together. Alumina (α-Al_2O_3) powder is produced by RSA Le Rubis [8] company in good agreement with JSPDS file no. 46-1212, the purity of the powder is at least 99.99%. For the growth of Ti-sapphire crystals, titanium-doped sapphire crackles and high purity titanium powder were adulterated as initial material. There are 5 classes of the starting concentration of titanium: 0.10 atom%, 0.17 atom%, 0.28 atom%, 0.45 atom% and 0.5 atom% respectively.

- Seed---- During undoped sapphire and Ti-doped sapphire crystal growth, two kinds of seed were used, one is oriented along a-axis [$11\bar{2}0$], another is r-axis [$10\bar{1}2$].

- Crucible---- The material of crucible is high purity iridium, its melting point is 2454°C, which is higher than the melting point of α-Al_2O_3, 2050°C. Compare to the other common crucible material molybdenum, iridium not only have high mechanical strength under working temperature, but also possess high chemistry stability, thus cause less contamination to sapphire. However, iridium is a costly material, easy to be oxidized or vaporized when works in air at high temperature, it's necessary to use protective gas as growth atmosphere. The diameter of crucible is 60 mm.

- Heater---- The crucible is conductively heated by a radio frequency (RF) coil, the material of the RF coil is copper. The RF coil position has a definite influence on the transport processes consequently affect the crystal quality, according to the experience, the top position of the RF coil is placed below the central position of the melt inside the crucible during the growth process.

- Growth atmosphere---- To protect Iridium crucible from oxidation, appropriate inert argon flow atmosphere of 1 bar is employed inside the growth chamber.

- Isolation---- ZrO_2 grains and tubes, quartz tubes, alumina discs are applied outside the iridium crucible as isolator to well keep the heat inside the heating system. Zirconium dioxide has a high chemistry stability, its melting point is 2680°C, the boiling point is 4300°C, the hardness is only second to diamond. ZrO_2 is one of the best fire resistance performance material in nature.

- Growth rate---- In Cz technique, usually the pulling rate is considered equal to the growth rate, which has most significant effect on growth process. In this work, to study the bubbles characterization as a function of the pulling rate, different pulling rate were chosen and employed. For sapphire crystal growth, the range of pulling rate is 1.5-5 mm/h. For Ti-sapphire crystal growth, the range of pulling rate is 1.5-4 mm/h.

- Rotation rate---- To study the effect of the rotation rate on bubbles formation, propagation, distribution, density etc., various rotation rates were used during growth process. For sapphire crystal growth, the range of rotation rate is 4-15 rpm. For Ti-sapphire crystal growth, the rotation rate was unaltered～8 rpm.

Table 2.1 CZ technique growth parameters of undoped sapphire and Ti-doped sapphire crystals and the thickness of prepared wafers cut from the ingot

Reference / Crystal	Raw material	Seed orientation	Pulling rate (mm/h)	Rotation rate (rpm)	Crucible material	Protective gas pressure	Thickness of wafers (mm)
Sapphire	alumina (α-Al_2O_3) powder and sapphire crackles	a $[1\bar{1}20]$	1.5-5	4-15	Iridium	Argon (1 bar)	0.5 / 1 / 2 / 5
		r $[10\bar{1}2]$	1.5-3	4-15			
Ti-sapphire	Ti-sapphire crackles and TiO_2 powder	a $[1\bar{1}20]$	1.5-4	8	Iridium	Argon (1 bar)	5
		r $[10\bar{1}2]$	1.5-4	8			

2.2 Characterization techniques

2.2.1 X-ray rocking curve

X-ray rocking curve (XRC) is an effective tool to characterize the structure integrity of single crystal. On the basis of diffraction peaks number and full width at half maximum (FWHM), we can analyze the integrity of crystal structure. XRC can also reflect the information of dislocation density, plane bending, low angle grain boundary and mosaic structure.

Figure 2.6 The setup for XRC measurement

The FWHM of diffraction peak is more smaller, it means more higher integrity of crystal structure. If there are multiple diffraction peaks, it means the crystal contains low angle grain boundaries. When the crystal structure is integrated, its angular breadth is smaller one or two orders of magnitude than the general spectral line width, thus has excellent angular resolution. This measurement employed a high resolution diffractometer PHILIPS X'Pert-MRD (figure 2.6), the diffraction source is Cu-K_α. It is not necessary to polish the samples.

2.2.2 Raman spectra

When the light with a frequency v_0 pass through a medium with a fixed vibration frequency v_i, due to the interaction between incident light and molecular

motion, the scattered light has 3 kinds of frequency: v_0, v_0+v_i and v_0-v_i, the first is Rayleigh scattering, the light with changed frequency correspond to Raman scattering, the spectrum with frequency v_0-v_i is called stocks line, the spectrum with frequency v_0+v_i is called anti-stocks line, this phenomenon was discovered by Indian physicist C.V. Raman in 1928. Raman spectrum is an important method to get the information of molecular vibration and rotation, widely applied to identify the material and analyze the structure of crystals or molecules. This technique was greatly improved after laser was invented, the nonlinear effect induced by intense laser results in new Raman scattering phenomenon.

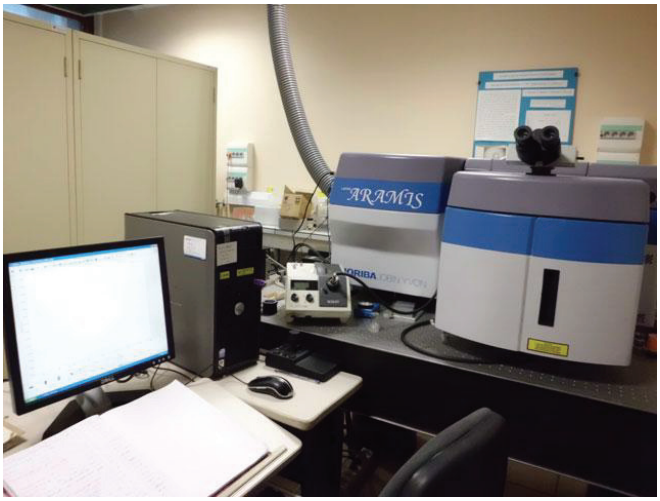

Figure 2.7 The spectrometer of Raman LabRam Aramis in ILM laboratory

The characteristics of Raman spectrum are: first the shift of Raman spectrum is only related to the energy level of molecular vibration and rotation in the material, is independent with the wavelength of incident light. Secondly, stocks line and anti-stocks line are distributed symmetrically on both sides of Rayleigh scattered light, usually the intensity of stocks line is stronger than anti-stocks line.

The advantages of Raman spectra are:

- No special sample preparation.
- Easy to operate in the analyzing procedure.
- The measurement is damage free, rapid, repeatable, high sensibility.

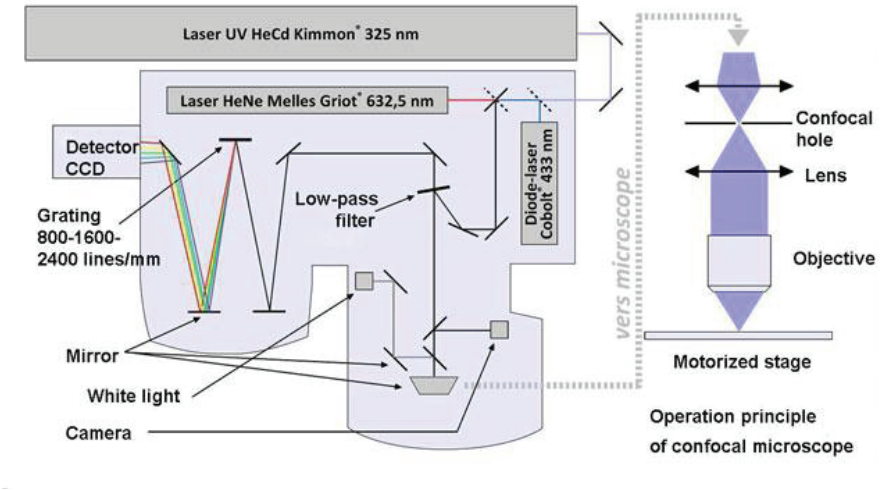

Figure 2.8 The operational scheme of Raman spectra equipment

In this study the Raman spectra were obtained with a microspectrometer Boriba Jobin Yvon® LabRam Aramis (figure 2.7). Figure 2.8 indicates the operational principles of the equipment, this spectrometer is coupled with three kinds of lasers: He-Cd 325 nm, He-Ne 633 nm and Cobolt-blue 473 nm, provided with three gratings: 600, 1800 and 2400 lines/mm, two filters: a dielectric filter (edge) in the UV and a notch filter in the visible to remove the laser stripe. In this work Cobolt-blue 473nm laser and grating 1800 lines/mm were employed. The spectral range is from 50 to 1000 cm^{-1}, the laser beam is focused on the sample surface with a ×100 objective, the spatial resolution is 1 μm with ×100 objective . The spectra obtained were compared with the standard spectra in the database RRUFF™ which got from well characterized minerals.

2.2.3 Optical microscopy

Optical microscopy is a method to obtain a picture of structures at the microscope scale. The principle in all cases is the same: the wave is emitted on the sample or transmitted by the sample, this wave is captured by a lens and the focus passes through an eyepiece that creates an image. This image is observed by the naked eye, or photographed, or recorded by camera CCD and stored on computer for processing. The techniques can identify accurately all kinds of defects and analyze qualitatively and quantitatively (size, number and location of the observed elements).

The principle is that the object is illuminated by a lamp, the emitted light is focused on the sample or the traverse. According to the intensity of the coloration, the light will be absorbed more or less and the area appears more or less dark. The principle is based on the fact that the structures have a different refractive index. This technique allows to observe samples without coloration.

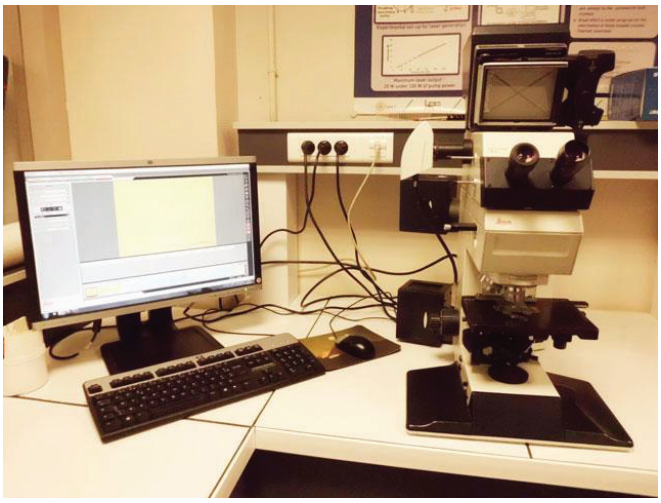

Figure 2.9 The optical microscope apparatus used in this thesis

The microscope used in this work is Leica DFC295 (figure 2.9), the apparatus is binocular and equipped with five magnifications of objective ×50, ×100, ×200, ×500, ×1000. It is not necessary that the object is translucent, because it is possible to have two light sources: microscopy transmission and reflection. For opaque material, reflection light source should be chosen and a vision of the surface is obtained. This principle is very significant, the influence caused by reflection and transmission light to the gained image of the crystals will be discussed in detail in the latter section.

The system used consists of a video camera and Leica software acquisition and image processing. The Leica Application Suite (LAS) marketed by Leica Microsystems Ltd. permits calibration of the microscope and then carry out the various measurements of the gas bubbles. It comprises a part of base that includes the environment and workflows of configure, acquire, browse and process. These are essential tools to refine, acquire and present images taken by the microscope. The main part of core software provides base for the configuration and control of the

microscope, as well as acquisition, analysis and processing of digital images of high quality. The core components include:

- Configuration of the microscope and digital camera and a fully integrated command.
- The automatic and manual exposure settings for obtain optimized imaging conditions.
- Calibration of the image based on the data read from Leica microscope and camera.
- Display the live image of the scale indicating the size of the image.
- Digital image acquisition in the familiar tree of explorer of images and folder structure. There is an optional module included in the archive database.
- The gallery of images acquired for a simple and quick reference.
- The text tools, scale and distance for a direct image annotation.

2.2.4 Wavefront measurement

Wavefront measurement was applied to detect defects in the crystals and how impact the crystal quality. The ideal surface of a wavefront plane that passes through a sample is a centered sphere on the focal point. The instrument therefore transforms the plane wavefront into spherical wavefront of a radius equal to the focal length of the optics. Due to aberrations, the actual surface is not a perfect sphere, and it is necessary to find a method to equate the surface in order to analyze the deviations it presents compared to the ideal sphere. Fritz Zernike created a new model based on the development of a polynomial which takes into account main optical aberrations affecting their specific terms. It is therefore possible to model a circular wavefront which is following an interferometer or a wavefront analyzer and decomposed into a series of polynomials each corresponding to an elementary aberration. Each term, and

it is the interest of this polynomial, corresponds to a type of aberration that is commonly found in optics. The terms, depending on their associated power, have an order. The polynomial consequently made it possible to equate a surface of wavefront. We can not measure that spherical powers or regular astigmatism (in the form of a sphere and a cylinder).

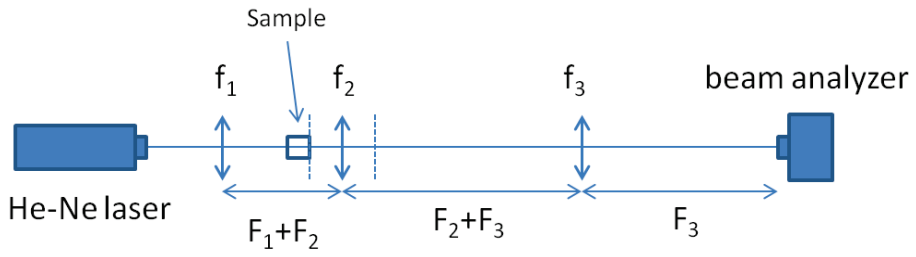

Figure 2.10 Diagram of wavefront measurement experimental setup

The principle illustration of the wavefront setup is represented in figure 2.10. A He-Ne laser is focalized by a lens f_1=100 mm. The sample is positioned at the waist of a laser beam. The diameter of the waist was measured at 140 µm. A focal imaging system is used to image the end face of the sample into a beam analyzer Beamwave 500. This imaging system is composed of two lenses: f_2 = 25 mm and f_3 = 254 mm so that G = 10. The beam analyzer Beamwave 500 from Phaseview is used to record the beam and wavefront profiles.

The Getlase software is used to analyze the beam profile and calculate the coefficients of the wave front decomposition in Zernike polynomials. To achieve this an optical sensor was used for analyzing a wavefront. Its principle is to break a wavefront in front elementary wave and determine the orientation for each of these front elementary wave. The measurement of these orientations allows to reconstruct the wavefront shape. After the wavefront recognized it is decomposed into aberrations known and listed by Zernike polynomials. The CCD camera converts the optical signal as many spots in digital data. The program Getlase software will allow to measure the position of these spots in the CCD plane.

2.2.5 Absorption spectra

The absorption measurements simply involve comparing the intensity of a light beam at a wavelength before (I_0) and after (I) its passage through the studied sample. The ratio of these two intensities depends on the thickness (L) of the sample, under the condition of an incident light with a certain wavelength λ, there is a relationship between the absorption coefficient and the thickness of the sample according to the law of Lambert-Beer:

$$e^{-KL} = \frac{I}{I_0} \tag{2.4}$$

Where I_0 is the intensity of incident light, I is the intensity of outgoing light, K is the coefficient of absorption (the unit is cm^{-1}), L is the thickness of the sample (the unit is cm). It is important to mention that in the absorption measurements, the beam emitted by the source passes through the sample after having left the wavelength selector. The radiation source most commonly used for measurements in the visible and near-infrared is the lamp of tungsten filament which continuous spectrum from UV to IR is calibrated. The filters and the monochromators for obtaining bands of narrow radiation were mainly used as wavelength selectors. The monochromators have the advantage of varying continuously the wavelength over an extended spectral range.

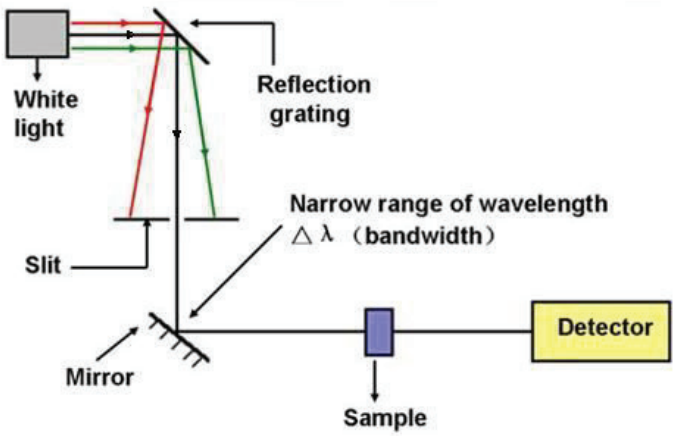

Figure 2.11 Experimental device of absorption spectrometer

The spectrophotometer is the device that makes it possible to accurately

measure the absorbance according to the different wavelengths. The absorbance α (without unit) is calculated by the formula:

$$\alpha = \lg \frac{I_0}{I} \tag{2.5}$$

Most of these spectrometers comprise four parts as indicated in figure 2.11:

- A reliable source of radiation energy.
- A wavelength selector that allows to isolate a limited area.
- A radiation detector or transducer that converts energy radiation into a measurable signal (usually electric).
- A processing device and signal display.

In this study a double beams spectrometer Perkin Elmer Lamda 900 (figure 2.12) was utilized to measure the absorption spectra of the samples. The instrument includes two lamps to cover a spectral range from 175 to 3300 nm. A deuterium lamp is used for the ultraviolet and a halogen lamp for visible and infrared emission. The light beam obtained is separated into two identical beams after passage in a monochromator. The intensity of the beam having passed through the samples is compared to the reference beam. It should also be noted that the automatic change of the lamps causes a slight discontinuity in the obtained spectra.

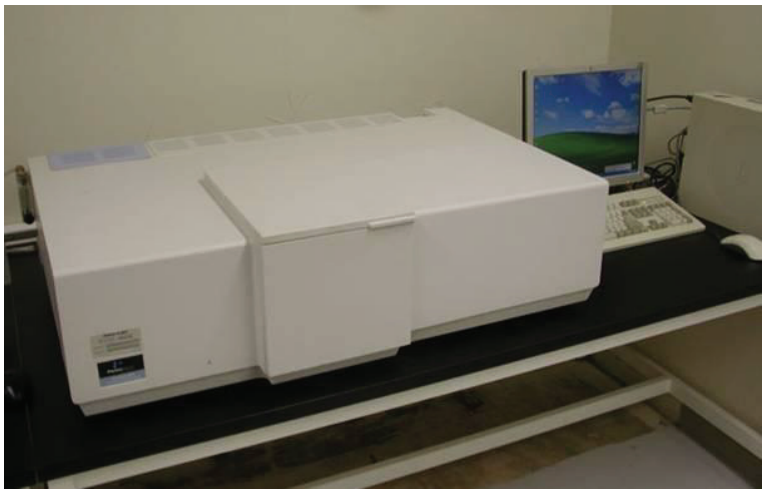

Figure 2.12 The setup of Perkin Elmer Lamda 900 UV/VIS/NIR photo spectrometer

2.2.6 Transmission and FOM

The principle of transmission is similar as absorption, the laser beam is separated into two beams by an optical splitter, the transmission of the original beam (E_0) is 1, measure the transmission of another beam passing through the sample (E_1), then compare the two transmission values will gain transmission rate of the sample, the equation is shown as below:

$$T = (E_0/E_1)\times coefficient \tag{2.6}$$

Where coefficient is a fixed parameter. It is important to make calibration of the transmission rate without samples each time to increase the accuracy of measurements. For sapphire slices, a He-Ne laser with the wavelength 633nm was employed, T value is mainly influenced by the crystal quality. For Ti-sapphire wafers, the light source was replaced by a green laser of (λ=532 nm, Z-laser ZM18), T value is impacted by the crystal quality and the titanium concentration. It should be noted that before measurements the polarization of the laser should be checked by 4 filters, and pay attention to the placement direction of the sample, because sometimes the orientation of crystals will make a slight variation of transmission (T) value.

As is known, figure of merit (FOM) as a function of the optical qualities of crystals is quite significant, which measures the ratio of the absorption coefficient at the pump wavelength of about 500 nm over the absorption coefficient associated with the parasitic Ti^{3+}-Ti^{4+} absorption band around 800nm. According to the relation between transmission and absorption, usually utilize T values to calculate FOM, which is more convenient. In this thesis, a 532 nm laser and a 800 nm laser were employed as pump band and laser band respectively. The inference procedure of FOM is as shown follows:

$$FOM = \frac{\alpha_{532nm}}{\alpha_{800nm}} \tag{2.7}$$

$$\alpha = \lg \frac{I_0}{I} \tag{2.8}$$

$$I = I_0(1-R^2)e^{-KL} \tag{2.9}$$

$$T_f = 1-R \tag{2.10}$$

$$T = T_f{}^2 e^{-KL} \tag{2.11}$$

$$K = -\frac{1}{L}\ln\frac{T}{T_f{}^2} \tag{2.12}$$

Where I_0 is the intensity of incident light, I is the intensity of outgoing light, K is the coefficient of absorption (the unit is cm^{-1}), L is the thickness of the sample (the unit is cm). α is absorbance intensity, T is transmission, T_f is the maximum transmission of laser beam minus reflections. Therefore formula (2.13) is concluded following formulas (2.7) to (2.12):

$$FOM = \frac{\alpha_{532nm}}{\alpha_{800nm}} = \frac{K_{532nm}}{K_{800nm}} = \ln\frac{T_{532nm}}{T_{f532nm}{}^2} \Big/ \ln\frac{T_{800nm}}{T_{f800nm}{}^2} \tag{2.13}$$

2.2.7 Micro-photoluminescence spectroscopy

In order to measure photoluminescence intensity of Ti-sapphire crystals on the micro-scale, a modified optical microscope allowing a pulsed laser injection (UV to visible), the focus of the beam (micro-scale spatial resolution) on the sample, as well as collection of the micro-fluorescence was employed. Such apparatus allows undertaking time-resolved measurements of micro-phases such as in minerals, glasses or phosphors. The general view of the micro-photoluminescence setup and the principle illustration of this apparatus are shown in figures 2.13 and 2.14 respectively.

Different pulsed laser sources can be used for time-resolved spectrodcopy, such as the harmonics of an Nd:YAG (532, 355 and 266 nm), nitrogen laser (337 nm), excimer (308 nm) or any excitation supplied by an OPO or a dye laser. The optical setup is based around an Axiotech 100 HD Zeiss microscope, modified to allow laser injection and fluorescence collection. The sample is observed either under

transmission or reflexion polarized white light, or under UV illumination (HBO lamp).

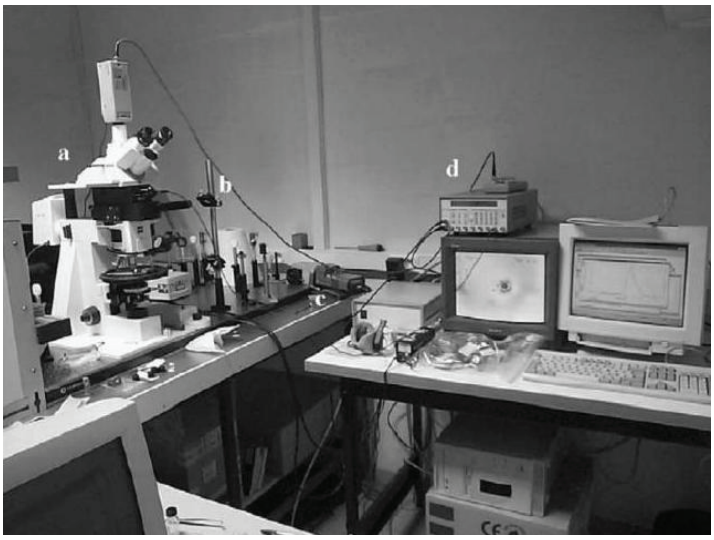

Figure 2.13 General view of the micro-photoluminescence setup (a) microscope; (b) laser injection; (c) ICCD camera; (d) delay generator.

A setup consisting on a dichroic mirror, for the selection of the excitation wavelength, and an objective (Epiplan Neofluar obj.>350 nm; Ealing/Coherent reflection obj. <350 nm) is used to focus the laser beam on the sample (spatial resolution over 5 lm with a ×50 objective). The limitation of the spatial resolution is mainly caused by the divergence of the laser beam. The emitted fluorescence is collected by the same objective and feed back in a pure silica glass fiber (transparent in the UV, visible and near IR range). The emitted light is then analyzed by the spectrometer (Oriel, grating 400 or 1200 l/mm) and recorded by a gated intensified CCD camera (Andor/Oriel Instaspec V ICCD). Such equipment allows time-resolved measurements with a minimum time resolution of 4 ns (delay and gate widths).

In this study, a Nd:YAG laser (Spectra-Physics) operating at 532 nm with an energy of 56 mJ per pulse was used as excitation source for Ti^{3+} ions. An iris followed by a beam expander system was used to shape the laser and obtain a good beam profile to gain spatial resolution. A laser power meter (Ophir) was placed in the beampath to monitor the laser energy in real time. The beam was introduced into a microscope (Zeiss, Axiotech) and focused on the sample surface through a×50

objective. Signal was collected through the same microscope system and transmit via an optical fiber to the spectrometer (Shamrock SR-303i; 1200-groves/mm grating with 303 mm focal length) and to the Intensified ICCD (IStar Andor).

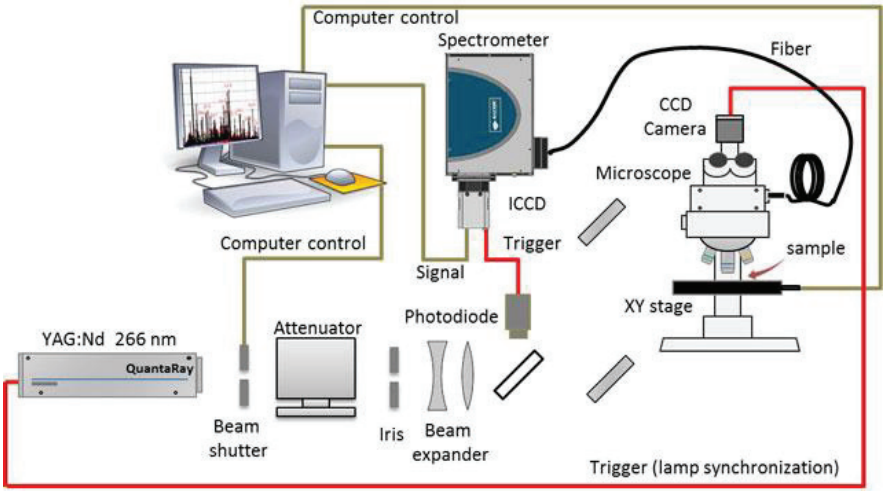

Figure 2.14 The principle illustration of micro-photoluminescence apparatus

2.2.8 Photoluminescence

To measure the excitation and emission spectra of sapphire and Ti-sapphire single crystals grown by Cz technique, an experimental setup which operational principle is indicated as figure 2.15 was employed. The light source is emitted from a Xe lamp (Energetiq EQ-99), then passes through a entrance slit, excitation monochromator (Jobin Yvon GEMINI) and exit slit, focalized by two lenses, reaches to the sample, the transmitted beam is passed by the fiber optic (high OH silica glass) and the filter reaches to emission monochromator (Jobin Yvon TRIAX), the informati-

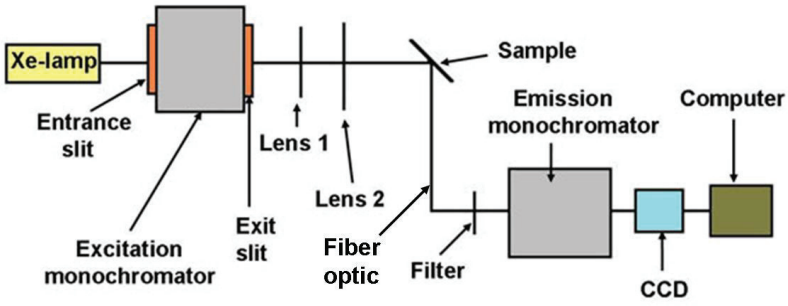

Figure 2.15 Illumination scheme of excitation spectra setup

-on is collected by the CCD (Jobin Yvon CCD 3000 with Peltier cooled) and stored in the computer, after a software Labview is applied to analyze the digital signal in the computer. There are several gratings in the excitation monochromator and emission monochromator respectively, usually only one is utilized according to the requirement.

2.2.9 Laser beam shape measurement

In order to visualize the effect of bubbles or other macroscopic defects on the intrinsic quality of the grown sapphire and Ti-sapphire crystals, a non-destructive analysis method has been applied. As exhibited in figure 2.16, a He/Ne laser emitting at 633 nm (Z-laser ZM18) with the power 1mw was utilized, the laser beam was focused and sent through the sample, the output intensity was recorded with a CCD digital camera connected to a computer, the software dataray was using to analyze the recorded information of laser beam shape. The figure of the transmitted laser beam without samples (in air) or passing through the region exempt any defects of the sample shows Gaussian profile, while for the region contains defects the beam profile was non-Gaussian and disturbed. Higher bubbles density or more macroscopic defects in the measured region, the pattern of the transmitted laser beam is more disturbed and distorted.

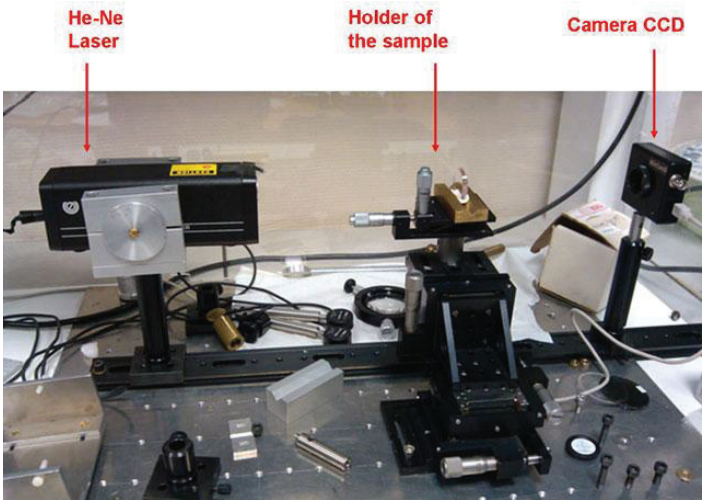

Figure 2.16 The setup of laser beam shape measurement

2.3 Conclusion

In this chapter we have presented Czochralski (Cz) crystal growth technology used in the frame of this PhD thesis to grow undoped and Ti-doped sapphire single crystal. We discussed the main parameters to control the growth process to obtain stationary stable regime. The crystals were grown in ILM laboratory, the cutting and polishing were performed in Cristalinnov platform at Montmélian. The grown crystals were microscopically and macroscopically characterized. In addition, we have described the technical experimental that we have used to characterize the grown crystals.

References:

[1] Kh.S.BAGDASAROV, *High-temperature Crystallization From Melt*, Edit Print. Edit Print, 2003, p. 180.

[2] C. J. Jing, S. Ihara, K.-I. Sugioka, T. Tsukada, and M. Kobayashi, "Analysis heat transfer in Cz crystal growth" *J. Cryst. Growth*, vol. 310, pp. 204–213, 2008.

[3] S. E. Demina and V. V. Kalaev, "3D unsteady computer modeling of industrial scale Ky and Cz sapphire crystal growth," *J. Cryst. Growth*, vol. 320, pp. 23–27, 2011.

[4] H. Fang, J. Tian, Q. Zhang, Y. Pan, and S. Wang, "Study of melt convection and interface shape during sapphire crystal growth by Czochralski method," *Int. J. Heat Mass Transf.*, vol. 55, pp. 8003–8009, 2012.

[5] C.-W. Lu, J.-C. Chenb, C.-H. Chenb, C.-H. Chenb, Wen-Ching Hsuc, and C.-M. Liu, "Effects of RF coil position on the transport processes during the stages of sapphire Czochralski crystal growth," *J. Cryst. Growth*, vol. 312, pp. 1074–1079, 2010.

[6] D.T.J.Hurle, *Crystal Pulling from the Melt*, Springer-V. Springer-Verlag, 1993.

[7] T. Duffar, *Crystal Growth Processes Based on Capillarity Czochralski, Floating Zone, Shaping and Crucible Techniques*. John Wiley & Sons Ltd, 2010.

[8] "http://www.rubisrsa.com." .

Chapter III

Results & Discussions: Undoped sapphire crystal

Sapphire bulk crystals were grown under different conditions by the Cz method, the crystallinity of the as grown sapphire was checked. Optical microscopy was used to study the bubbles in the as grown crystals, the shape of bubbles were analyzed. In order to optimize the growth parameters, bubbles distribution and density as functions of the pulling rate and the rotation rate were investigated. The origin and propagation of bubbles were analyzed; the prospective means to eliminate the bubbles of sapphire crystals were put forward. Furthermore, the influence how bubbles degrade the quality of sapphire was visualized by optical means, the optical characterizations of the as grown sapphire crystals were performed and discussed.

3.1 Undoped sapphire crystals grown by Cz technique

Sapphire crystals were grown along a-axis [$11\bar{2}0$] and r-axis [$10\bar{1}2$] respectively, the pulling rate was from 1.5 to 5 mm/h, the rotation rate was from 4 to 15 rpm. The crystals grown along a-axis are faceted and the ones along r-axis have circular geometry. The geometry of the bottom (end) of the grown crystals and the tail length depend on the growing parameters program selected in the pulling software [1]. In addition, to control melt decomposition and material evaporating from the charge, the weight of the crucible including the charge were followed during all the experimental procedure (figure 3.1).

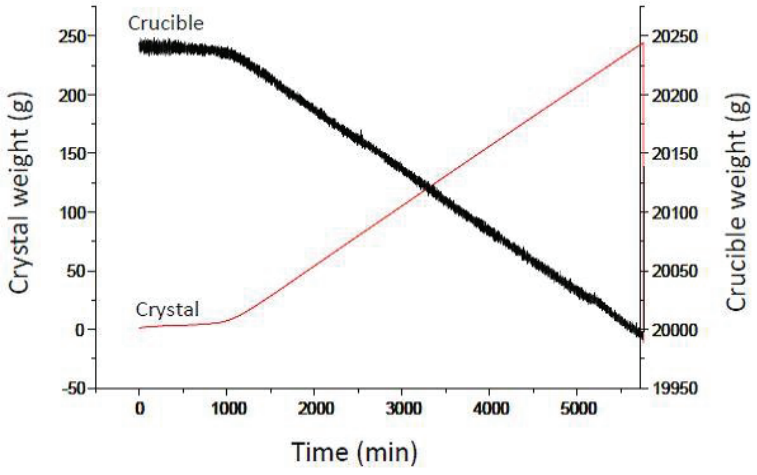

Figure 3.1 Crucible and crystal weight evolution during growing sapphire crystal under stationary stable regime.

The profile of the grown boules is cylindrical with good symmetry and uniformity. The cylindrical profile has been adjusted by varying the crystal growth parameters, so that the heat power and pulling rate are changed and automatically controlled. The obtained sapphire crystals weighted 250–400 g and were approximately 28–35 mm in diameter and 90–110 mm in length. Some undoped sapphire crystals are shown in figure 3.2.

Figure 3.2 The as grown sapphire crystals grown by Cz method

Whatever the growth direction and growth rate, the as grown sapphire crystals were transparent and colorless, exempt of visible macroscopic defects such as cracks, inclusions etc. The as grown sapphire crystals were inspected by microscopy and green laser beam (532 nm), gas micro bubbles were observed. The sapphire crystals grown at low speed contained comparatively very few bubbles, while the sapphire crystals grown at high speed contained much more bubbles. The typical sapphire crystals grown at low speed and high speed are illustrated in figure 3.3a and b, it should be noted that the micro bubbles in sapphire crystals can not be observed by eyes directly. In order to visually shows how to estimate qualitatively the bubbles distribution in the grown crystals, a non-destructive analysis method based on the utilization of green laser beam emitting at 532 nm and power 5 mW was used. The laser beam was sent through the crystal normal to the growth direction. The region containing bubbles absorb the green laser beam, while the regions without bubbles do

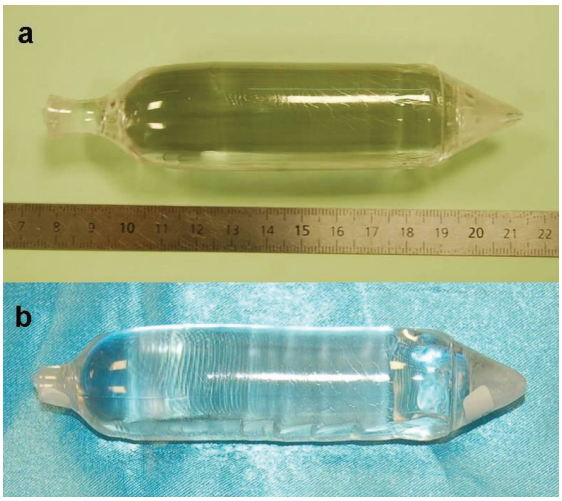

Figure 3.3 Sapphire crystals grown with (a) pulling rate 1.5 mm/h, 8 rpm, a-axis; (b) pulling rate 3 mm/h, 15 rpm, r-axis.

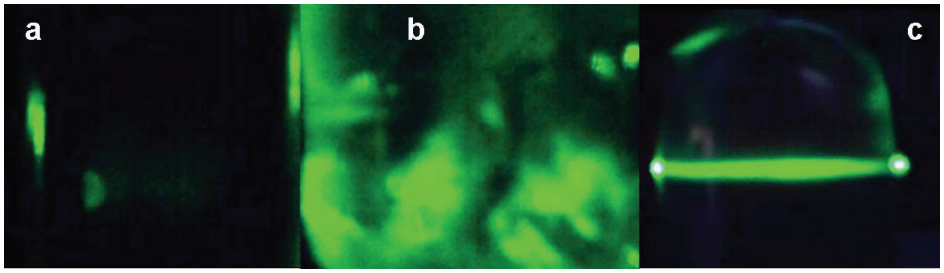

Figure 3.4 Bubbles analysis by green laser beam (532 nm), the crystal contained (a) very few bubbles; (b) middle quantity of bubbles; (c) lots of bubbles.

not absorb the green light and the beam passed through the crystal volume. The distribution of bubbles over the normal section to the growth direction is shown in figure 3.4. Figure 3.4(a) presents a sapphire crystal grown at low speed that contained very few bubbles, (b) was grown at middle speed that contained middle quantity of bubbles, and (c) was grown at high speed that contained a great deal of bubbles.

3.2 Sample preparation

To characterize the bubbles and optical properties of sapphire crystals correctly, the as grown crystals were cut into wafers of different thickness and optically polished in cristalinnov plateform. As indicated in figure 3.5, three parts of each crystal (top, middle and end) were cut along the direction perpendicular to growth direction, then been optically polished of both sides and characterized. In order to

study the form, the size and distribution of micro bubbles without any feint, sapphire crystals grown along a-axis and r-axis were cut into various thickness of 0.5 mm, 1 mm, 2 mm and 5 mm respectively, figure 3.6 shows some optically polished sapphire wafers of 2 mm thickness cut from the top, middle and end parts of the crystals. For all the measurements in this thesis, optically polished specimens were used, however, raman scattering measurements have no strict requirements of the specimens.

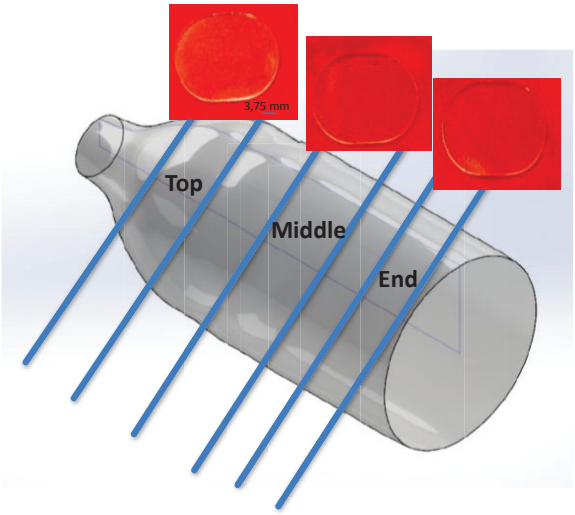

Figure 3.5 Cutting area for crystal polishing and defects analysis. (the wafers in this figure were cut from crystal grown along a-axis)

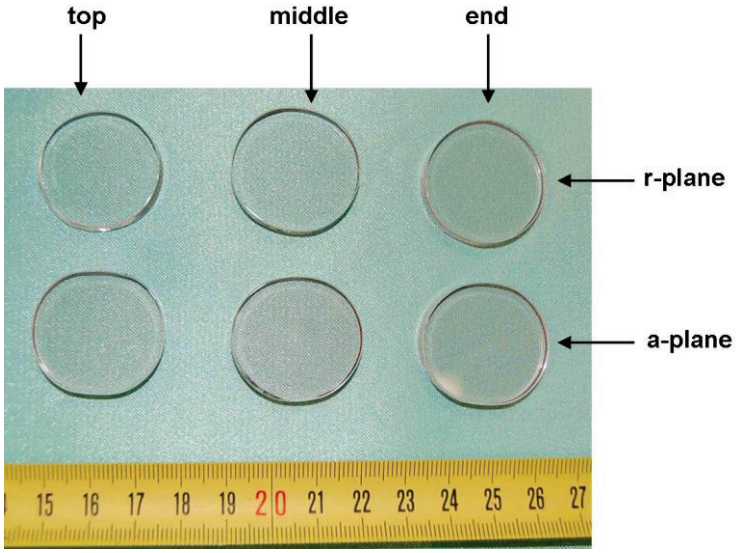

Figure 3.6 Optically polished sapphire wafers of 2mm thickness (cut from crystal grown along a-axis and r-axis respectively)

3.3 Bubbles characterization

3.3.1 The principle of optical microscope

The principle of optical microscope is getting image magnification effect produced by optical lens. An optical microscope usually consists of stage, lighting system, objective, eyepiece and focusing mechanism. Lighting system includes lighting source and condenser, the role of condenser is getting more light being focused on the observed position, the spectral characteristics of lighting source must suit the working band of microscope receiver. Lighting system has significant impact on the imaging performance of the microscope, however, it is the most easy to be ignored part by users. Its function is supplying adequate and well-distributed illumination for the object. The beam from convergent mirror should be able to ensure full of aperture angle lens of the objective, otherwise it can not be fully utilized to achieve the highest resolution ratio of the objective. For this purpose, there is a variable aperture stop (VAS), similar with the camera lens, which can adjust the aperture size for adjusting the aperture of the illumination beam to match the aperture angle of the objective. Changing the illumination mode, a dark point on the bright background (called bright-field illumination) or a bright point on the dark background (known as dark-field illumination) and other different way of watching can be obtained, in order to better identify and observe fine structure under different situations.

According to the kinds of specimens, optical microscope can be classified into reflection type and transmission type. The specimen of reflection type is usually opaque, the light from above is emitted on the object, the reflected light from the object goes through the microscope. This kind of microscope usually is used for observing the solid of engineering and materials, called metallographic microscope in domain of upright microscope. The specimen of transmission type is transparent or very thin, the light can penetrate the object and go into the microscope. This kind of microscope usually is used for observing biotic tissues or transparent objects. To

investigate the exact image of bubbles structure in undoped sapphire and Ti-doped sapphire crystals, we used an optical microscopy with two lighting sources of transmission and reflection respectively. The microscope equipment (LEICA DMR-XRE) is binocular and possesses five objective magnifications (×50, ×100, ×200, ×500, ×1000).

It should be noted that undoped sapphire and Ti-doped sapphire are transparent crystals, and bubbles are not distributed on the surface but inside the crystals. According to the functional principles of transmission and reflection mode, the former is more appropriate for the processed wafers. Furthermore, if the thickness of sample is too large, it's difficult for the transmission light to go through the wafer completely and been focused by the lens accurately. In this study, 0.5 mm is the best thickness to observe bubbles form with transmission light, 1 mm, 2 mm and 5 mm are all too thick for transmission light. Besides, 2 mm and 5 mm are too thick for reflection light over ×200 magnifications. To sum up, appropriate thickness, plane surface and optical polishing are necessary requirements of samples to study the exact structure of bubbles. On the other way, although these photos could not reflect true shape of bubbles, they could illuminate the rough distribution of bubbles. In this paper, we compared microscopic photos under transmission and reflection light source, discovered real figure and regulations of bubbles, thus redound to confirm the origination of bubbles in undoped sapphire and Ti-doped sapphire single crystals grown by Cz technique.

3.3.2 Bubbles distribution in undoped sapphire crystals

Whatever the seed orientation or growth speed, micro bubbles had been observed in the crystals, most of bubbles were spherical and were distributed in the crystal volume. Table 3.1 summarizes the obtained results as a function of the growth conditions. We can find that, the changes of seed orientation, pulling rate and rotation rate have no apparent effect on bubbles size and distribution. The changes of pulling rate and rotation rate had no apparent effect on the size and the bubbles distribution.

The statistical quantitative analysis of the bubbles showed that bubbles density were influenced by the pulling rate and rotation rate, which will be discussed in detail in the section 3.3.4 and 3.3.5.

Table 3.1 Bubbles analysis in undoped sapphire crystals as a function of growth conditions

Reference	CrysU1	CrysU2	CrysU3	CrysU4	CrysU5	CrysU6	CrysU7	CrysU8
Seed	a-axis	a-axis	a-axis	a-axis	a-axis	r-axis	r-axis	r-axis
Pulling rate (mm/h)	1.5	2	2.5	3	5	1.5	2	3
Rotation rate (rpm)	8	8	8	8	8	8	8	8
Bubbles sizes (μm)	2-5	2-5	2-5	2-5	2-5	2-5	2-5	2-5
Bubbles distribution from the top to the end of the crystal	All volume	All volume	All volume	All volume	All volume	All volume	All volume	All volume
Reference	CrysU9	CrysU10	CrysU11	CrysU12	CrysU13	CrysU14	CrysU15	CrysU16
Seed	a-axis	a-axis	a-axis	a-axis	r-axis	r-axis	r-axis	r-axis
Pulling rate (mm/h)	1.5	2.5	1.5	2.5	1.5	2	2	3
Rotation rate (rpm)	4	4	15	15	4	4	15	15
Bubbles sizes (μm)	2-5	2-5	2-5	2-5	2-5	2-5	2-5	2-5
Bubbles distribution from the top to the end of the crystal	All volume	All volume	All volume	All volume	All volume	All volume	All volume	All volume

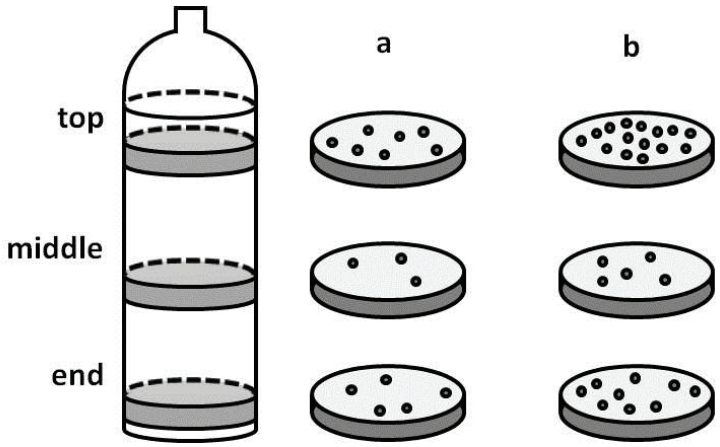

Figure 3.7 Schematic illustration of bubbles distribution in undoped sapphire crystals grown by Cz technique. (a) at low pulling rate and rotation rate; (b) at high pulling rate and rotation rate.

Figure 3.7 schematically illustrates the bubbles distribution in sapphire crystal volume. Crystals grown at high velocity contained more bubbles (figure 3.7b) than

grown at low velocity (figure 3.7a), which is in good agreement with the research of A.Ghezzal et al. [2] during shaped sapphire crystal grown by micro-pulling down technique. The average distance between each bubble is about 30µm±3. This distance changes as a function of the position (top, middle, end) of the wafer in the crystal. It becomes higher at the bottom of the crystal and reaches 45µm±5 at the end.

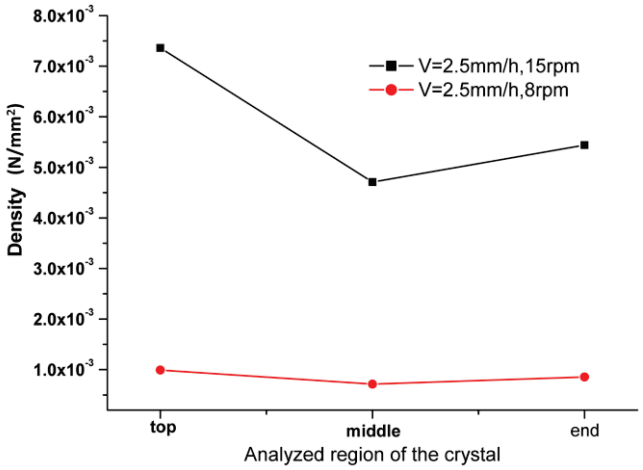

Figure 3.8 Bubbles density variation in different parts of undoped sapphire crystals

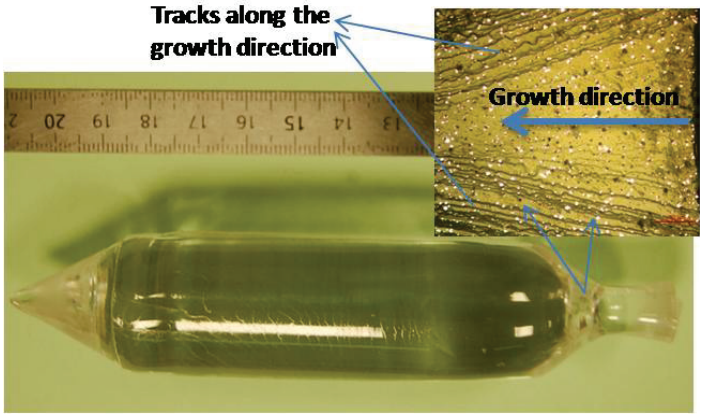

Figure 3.9 Tracks observed in sapphire crystal grown at high pulling rate (v_g = 5 mm/h)

Bubbles characterization showed that, bubbles density varies as a function of different position of the crystal, as we can see from figure 3.8, the order of bubbles density in different parts of sapphire crystal is: top part > end part > middle part. Generally the bubbles appear directly after seeding. At the top (beginning) of the crystal, high density of bubbles is accompanied by tracks apparition, their density is strongly connected to the bubbles density (figure 3.9). It should be noted that not all

the bubbles distributed randomly, there are some bubbles distributed in a line as shown in figure 3.10. This kind of linear arrangement bubbles had no special orientation, no fixed length and location. Linear bubbles and random arrangement bubbles were aleatory distributed in the crystal volume.

3.3.3 Quantitative bubbles sizes analysis

The bubbles in sapphire wafers of 0.5mm thickness were studied using microscope under reflection light and transmission light respectively. Figure 3.10 shows the bubbles distributed randomly and figure 3.11 shows the bubbles distributed regularly in a line. The inerratic linear arrangement of bubbles were observed in top, middle and end parts of the sapphire crystals, and without fixed orientation.

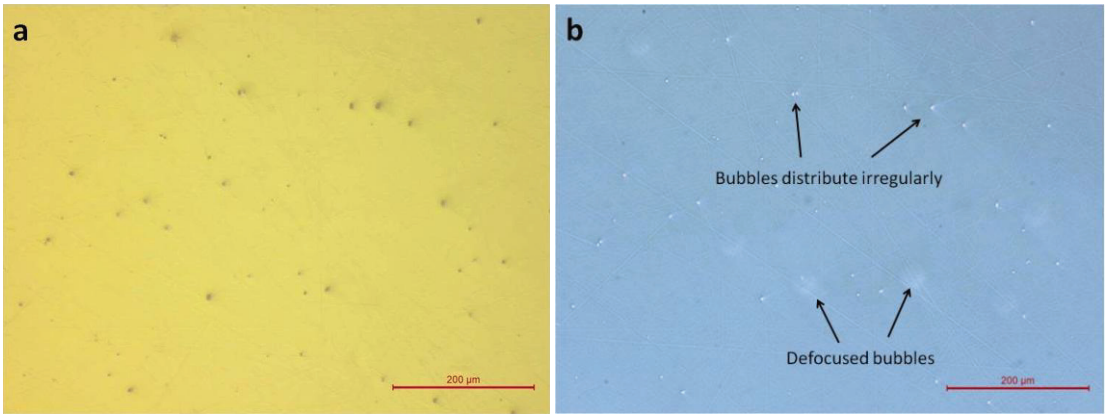

Figure 3.10 Bubbles distribute irregularly in 0.5mm thickness sapphire wafers. (a) with reflection light; (b) with transmission light.

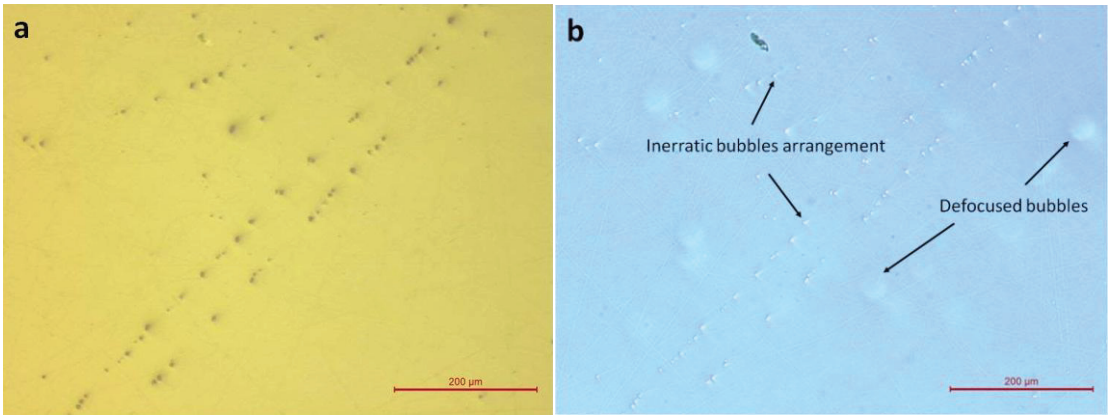

Figure 3.11 Inerratic bubbles arrangement in 0.5mm thickness sapphire wafers. (a) with reflection light; (b) with transmission light.

From figure 3.10a and figure 3.11a we could observe the size and figure of different bubbles under reflection light are inequitable, whereas figure 3.10b and figure 3.11b indicate bubbles under transmission light at the same region show nearly uniform size and spherical shape. Their diameters were in a range from 2 μm to 5 μm. From comparison we could get a conclusion that the so-called big size "bubbles" were formed by several small closer bubbles. To further illuminate the phenomenon, another four amplificatory pictures (figure 3.12) were exhibited and compared. Figure 3.12b shows two small spherical bubbles integrated one big "bubble" with irregular shape(figure 3.12a). Figure 3.12d shows many small bubbles congregated one anomalous figure "bubble" (figure 3.12c).

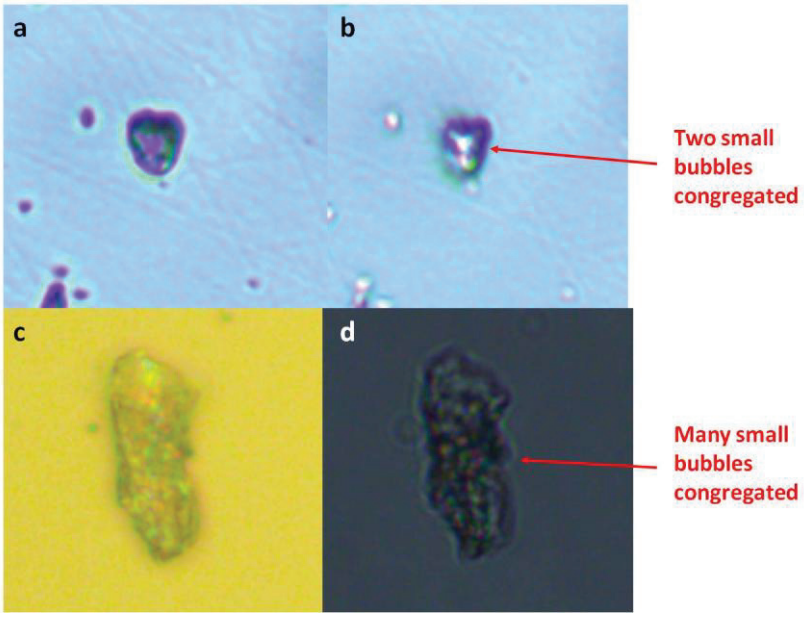

Figure 3.12 Contrast figure of bubbles congregation in sapphire wafer with thickness 0.5mm under reflection light and transmission light. (a), (c)-reflection mode; (b), (d)-transmission mode.

It should be noted that there were two kinds of "bubbles" in figure 3.10b and figure 3.11b, one kind with diameters range from 2 μm to 5 μm, another kind with diameter ranger from 20 μm to 25 μm. In fact, the latter "bubbles" with bigger size were out-focused images of the former small bubbles. Figure 3.13 illustrates visibly how the bubbles morphology changed with different focalization positions under transmission light. When the light was focused below the bubbles, "bubbles" showed larger dark figures (figure 3.13a, b, c). Continually shifted focalization at appropriate

position on bubbles in red circle, we could find some spherical bright small bubbles with similar size, two or more small bubbles were so close that connected into a so-called “big bubble” (figure 3.13d). Then kept changing focalization to above the bubbles, the image of bubbles in red circle became more and more blurry until disappear completely as is shown from figure 3.13e to figure 3.13l, these spherical bright bubbles of large size were accordant with the defocused bubbles in figure 3.10b and figure 3.11b.

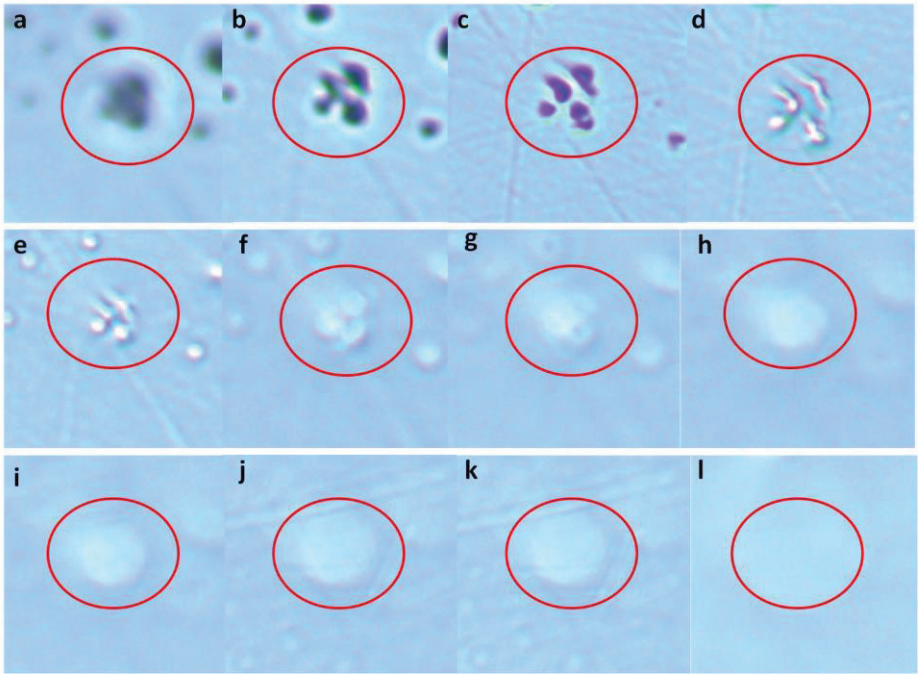

Figure 3.13 The effect of different focalization positions under transmission light on bubbles (in red circle) visualization of the sapphire wafer with 0.5mm thickness. (a), (b), (c)-focalized below the bubbles; (d)-appropriate focalization; from (e) to (l)-focalized above the bubbles.

3.3.4 The effect of pulling rate on bubbles

To analyze the effect of the pulling rate on bubbles distribution and density variation, sapphire crystals were grown with various pulling rate 1.5, 2.5, 3 and 5 mm/h at the same rotation rate 8 rpm respectively with inert argon flow atmosphere of 1 bar inside the growth chamber. The grown crystals were carefully inspected and evaluated for defects analysis. Whatever the growth direction, all the grown sapphire crystals were colorless, transparent and exempt of visible macroscopic defects. Three

parts of each crystal (top, middle and end) were perpendicular cut, optically polished and characterized. The distribution of bubbles, the number of bubbles per unit area of crystals were measured using Leica optical microscope.

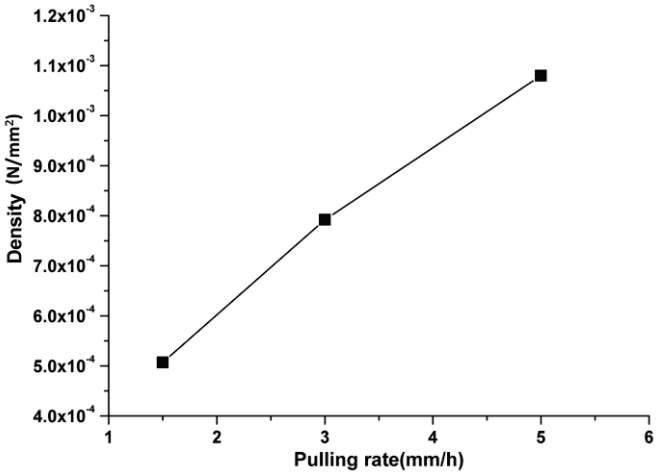

Figure 3.14 Bubbles density variation as a function of pulling rate (V_r=8 rpm)

For sapphire crystals, no matter grown along a-axis or r-axis, no matter low growth rate (1.5 mm/h, 8 rpm) or high growth rate (5 mm/h, 8 rpm), bubbles were observed and presented a random distribution in the section, the diameter of bubbles kept the same order of magnitude: ranges from 2 μm to 5 μm. .To analyze the effect of pulling rate on bubbles density variation, we chose the bubbles density of middle part from each sapphire crystal for comparison. From figure 3.14, we can find bubbles density is strongly affected by the pulling rate, which increased linearly with the increasing of pulling rate from 1.5 mm/h to 5 mm/h at rotation rate 8 rpm. Furthermore, high pulling rate had more possibility to cause the melt flow rapidly thus more possibility of bubbles to be captured by solidification interface in linear arrangement than low pulling rate.

3.3.5 The effect of rotation rate on bubbles

To analyze the effect of the rotation rate on bubbles distribution and density variation, undoped sapphire crystals were grown at various rotation rate 4, 8 and 15 rpm and the same pulling rate 2.5 mm/h respectively with inert argon flow atmosphere of 1 bar inside the growth chamber. The grown crystals were carefully

inspected and evaluated for defects analysis. Whatever the growth direction, all the grown sapphire crystals were colorless, transparent and exempt of visible macroscopic defects. Three parts of each crystal (top, middle and end) were perpendicular cut, optically polished and characterized. The distribution of bubbles, the number of bubbles per unit area of crystals were measured using optical microscopy.

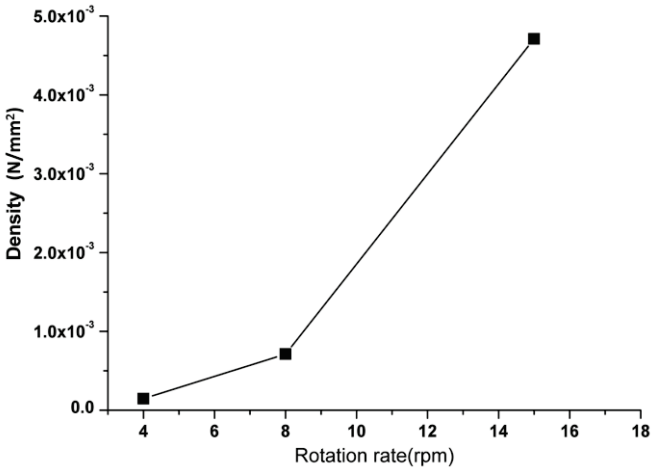

Figure 3.15 Bubbles density variation as a function of rotation rate (pulling rate 2.5mm/h)

For sapphire crystals, no matter grown along a-axis or r-axis, no matter low rotation rate (2.5 mm/h, 4 rpm) or high rotation rate (2.5 mm/h, 15 rpm), bubbles were observed and presented a random distribution in the section, the diameter of bubbles kept the same order of magnitude: ranged from 2 μm to 5 μm. With the increasing of rotation rate from 4 rpm to 15 rpm at pulling rate 2.5 mm/h, the bubbles density increased as shown in figure 3.15. When the rotation rate varied from 4 rpm to 8 rpm, the bubbles density increased comparatively slowly, during the variation of 8 rpm to 15 rpm, the bubbles density increased drastically. Alike pulling rate, high rotation rate also had more possibility to cause the melt flow rapidly thus more possibility of bubbles to be captured by crystallization interface in linear arrangement than low pulling rate.

As presented in section 2.1.2, in fact, the rotating crystal acts an important role in Cz technique. First it is helpful to get the desirable circular shape of crystal, second

it is also beneficial to yield the crystal having a radial uniformity of doping. From the present result, we suggest that rotation rate should not be higher than 8 rpm. Besides, in the next chapter, Ti-doped sapphire crystals exempt of bubbles were successfully grown with pulling rate 1.5 mm/h and rotation rate 8rpm. So, in this program, when the rotation rate is less than 8 rpm, it is acceptable.

3.3.6 The origin of bubbles

In the section 1.7.3.1 we summarized that, there are mainly four hypotheses to explain the origin of the bubbles: (1) growth atmosphere; (2) reaction among the molten alumina, the crucible and the graphite devices; (3) thermal decomposition of molten alumina; (4) dissolved gas in the raw material.

In the case of this thesis, we will analyze the four hypotheses one by one. For the (1) hypothesis—growth atmosphere, high purity argon of 1 bar pressure was used as protective gas during crystal growth. In our research, sapphire crystals exempt of bubbles were already obtained under the same growth atmosphere condition. That demonstrates the inert gas used is of high purity, the growth chamber is perfectly sealed and the vacuumizing before input argon was well achieved, so the growth atmosphere can be excluded to be origin of the bubbles.

For the (2) hypothesis—reaction among the molten alumina, the crucible and the graphite devices. In this thesis, the material of crucible is iridium; ZrO_2 grains and tubes, quartz tubes, alumina discs were applied for isolation, there were no graphite devices utilized in the crystal growth, so the forth hypothesis is excluded to be origin of the bubbles.

For the (3) hypothesis — thermal decomposition of molten alumina. As presented in the section 3.1, to control melt decomposition and material evaporating from the charge, the weight of the crucible including the charge were followed during all the experimental procedure (figure 3.1). A good thermal gradient was optimized and stable convection flow minimizes the fluctuation temperature which results in growing crystals under stationary stable state regime. It means the temperature of

melting zone in the preestablished programme should be well controlled below overheating degree (2100°C). But in actual growth, it is difficult to completely avoid overheating, so thermal decomposition of molten alumina was possibly to be a supplementary origin of gas.

Until now, the hypotheses (1) and (2) are all excluded, (3) is one supplementary possibility of bubbles origination. Therefore only hypotheses (2) —dissolved gas in the raw material, is assumed to be the main origin of bubbles. As illustrated in figure 3.16, if we just use alumina powder as the raw material, the volume of sapphire crystal will decrease distinctly after solidification, for the sake of getting enough large size sapphire efficiently, we usually use sapphire crackle and alumina powder together as raw material.

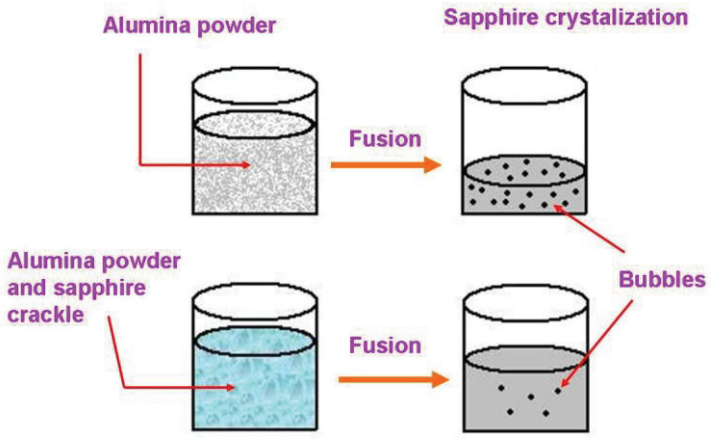

Figure 3.16 The difference between utilization of sapphire crackle and/or alumina powder [3]

There is another significant advantage to use crackle and powder at the same time, the obtained sapphire crystal contains much less quantity of bubbles than that grown from alumina powder. It is obvious that the density of alumina powder is less than sapphire crackle, the powder raw material contains more gas difficult to remove before crystal growth. Besides, the sapphire crackle is obtained from the melt, most part of gas were removed during the crystallization step. In conclusion, to get sapphire crystals with low bubbles concentration or bubbles free, it is better to use crackle sapphire than alumina powder.

3.3.7 The propagation of bubbles

Dissolved gas in the raw material will form micro bubbles in the melt, if these bubbles can not escape from the solid-liquid interface before crystallization, they will be captured by the growing crystal. As for how the bubbles penetrate from the melt to the crystallization interface and finally trap into the solid, E. Ghezal and K. Lebbou [4] observed the whole process by visualization of the crystallization interface and molten zone in sapphire crystals grown by μ-PD method. Although μ-PD is pulling down

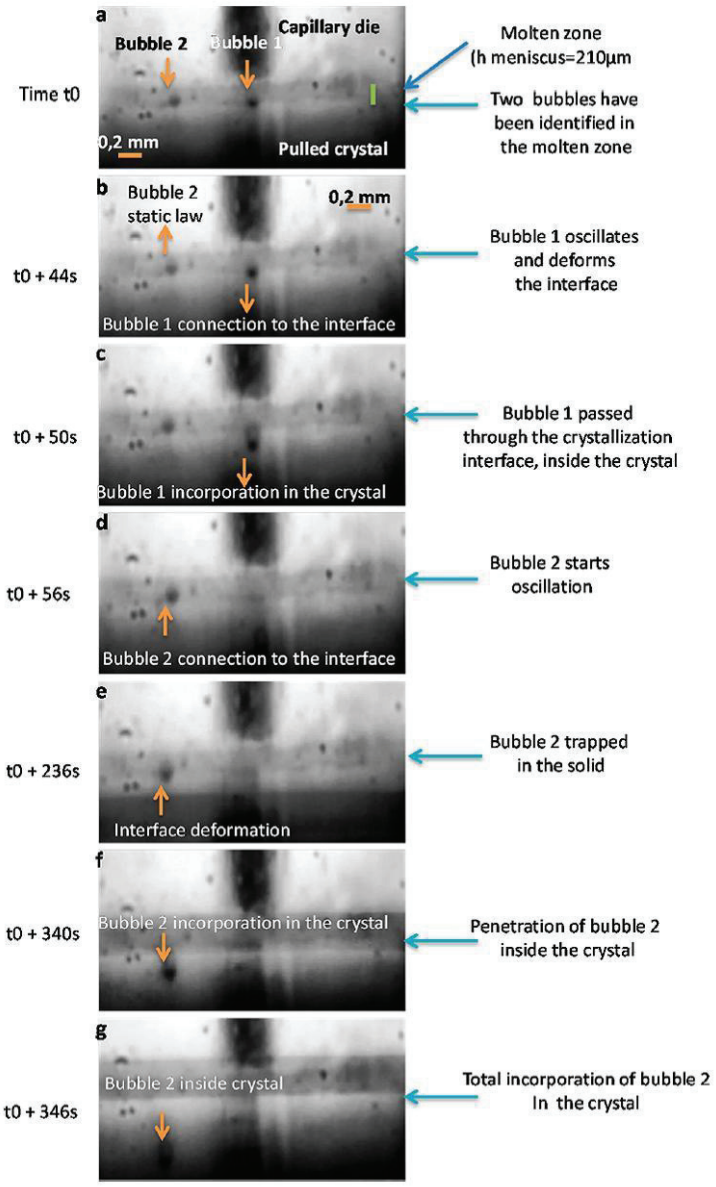

Figure 3.17 Video sequence of two bubbles' trajectory and the different steps before their incorporation in the crystal. The horizontal arrow shows the solid−liquid interface [4]

fiber, plates and rod shaped crystals while Cz is pulling up the crystal, but they can have a similar dynamic transfer process of the bubbles.

As illustrated in figure 3.17, where two bubbles can be seen in the molten zone as well as their movements before and after incorporation in the crystal. It should be noted that in figure 3.17a, bubble 1 and bubble 2 were at the same horizontal level, then bubble 2 spend more long time to penetrate the interface, and finally incorporate in the crystal at different level with bubble 1. That is due to the temperature field of two bubbles are different, which results from the difference of convection, flux, heat transfer and so on.

In the case of Cz method, we use rotation seed which is not used in the case of μ-PD technique, so it is more complicated and more difficult to explain the temperature field in melting zone and crystallization interface, some researchers make effort on simulation of thermodynamic analyses by computer modeling [5][6][7], here we try to simplify the explanation of the bubbles distribution by several significant factors.

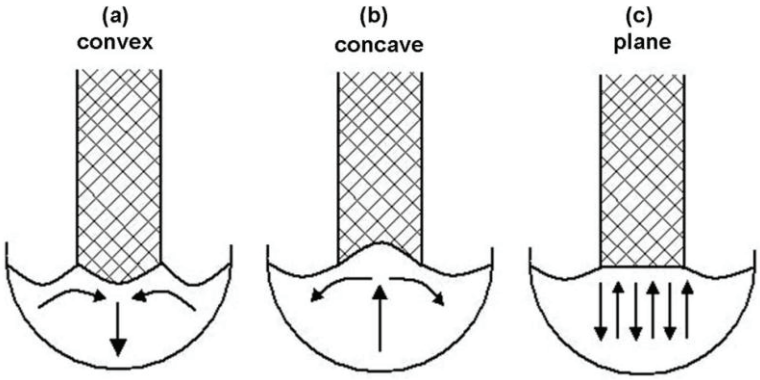

Figure 3.18 Convection flows in melt (shown by arrows) in growing single crystals (crystals are marked with hatching) by Cz method at different growth fronts [8]

Figure 3.18 indicates the convection flows in the melt during growing single crystals by Cz method at different growth fronts [8]. In Figure 3.18a the growth front is convex, and should be attributed to the low growth rate and rotation rate, in this case natural convective flow is predominant, bubbles have more time to escape from the interface, and the rest bubbles will follow the flux then concentrate in the center of

crystal. Figure 3.18b presents the concave interface, which should be attributed to the high growth rate or rotation rate, in this case forced convective flow is predominant, bubbles have less time to escape from the interface, and the rest bubbles will follow the flux then concentrate in the side of crystal. Figure 3.18c presents flat solid-liquid interface, which means the growth rate and rotation rate employed are appropriate, in this case natural and forced convective flow have equal effect, the bubbles will distribute randomly in the melt, and if the bubbles are created at the same horizontal level array in a line, they will keep the same position during penetration process, finally they will be captured by the crystal in a line array, which can explain why some bubbles present a linear arrangement.

As for the bubbles density in different parts of sapphire crystals is in the order of: top part > end part > middle part, which can be mainly attributed to two reasons. The first reason is that, under the dual effects of gravity difference between the gas and the liquid, and the heat transfer, the bubbles have a trend of rising, so the bubbles density of the molten zone is: top part > middle part > end part. The second reason is that, when the growth speed is changing, the solid-liquid interface becomes unstable, more possibilities of the bubbles being captured by the crystallization. It is obvious that the middle part of crystal has most steady growth velocity. Based on this two reasons, the bubbles density in different parts of sapphire crystals is in the order of: top part > end part > middle part.

3.3.8 Predicted model for the incorporation of bubbles defects

In order to study how the creation and the incorporation conditions affect the bubbles in undoped sapphire bulk crystal grown from the melt by Cz technique, several crystals have been grown with various growth conditions. All the crystals have practically the same diameter, but the pulling rate, the rotation rate and the seed are different. Considering the results presented above and the observation that we have register from the growth process it is possible to propose a coherent description of whole phenomena involved during the incorporation of bubbles defects in the crystal.

Before their incorporation in the crystal, the bubbles should destabilize the crystallization interface, they were trapped by the solidification interface and are incorporated in the crystal.

The bubble size in stationary equilibrium in the liquid depends on the liquid nature and the pressure in the liquid and the bubble. The difference pressure between the bubble and the liquid strongly depend on the temperature of the liquid given by the following equation:

$$\Delta T = T_{melt} - T_{liquid} \approx \Delta P = 2\sigma/r \quad (3.1)$$

T_{melt} -melting temperature, T_{liquid} -liquid temperature, ΔP-pressure difference between bubble pressure and the liquid pressure, σ-superficial tension; r-bubble radii.

If the bubbles diameter increase, it strongly depend on ΔP value controlled by liquid diffusion environment and the diffusion process is favoured by energy transfer from liquid to liquid gas interface. This energy allowed the production of the bubble and maintain the difference pressure.

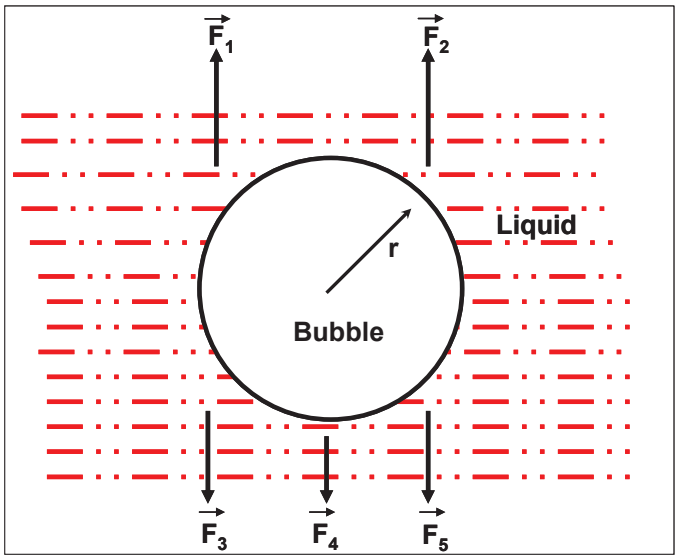

Figure 3.19 Forces acting on bubble in the liquid

The bubble in the liquid near the crystallization interface is in equilibrium (The forces resultant acting on the bubbles is zero) (figure 3.19). This equilibrium is strongly controlled by the thermal gradient around the bubbles.

$$F_1 + F_2 = F_3 + F_4 + F_5 \quad (3.2)$$

F_1: Archimedes force

$$F_1 = 4/3\ \pi r^3 \rho_l g \tag{3.3}$$

R-bubble radii, ρ_l-liquid density, g-gravitational acceleration.

F_2: Hydrodynamic force

$$F_2 = 2\pi v \eta_l (2\eta_l + 3\eta_p / \eta_l + \eta_p)\ r/h \tag{3.4}$$

v-growth speed, η_l :liquid viscosity, η_p-gas viscosity, r-bubble radii, h-distance between bubble and crystallization interface.

F_3: Capillary force

$$F_3 = -4\pi r^2\ (\partial\sigma/\partial T) 1.5 G_T \tag{3.5}$$

σ:liquid-gas surface energy, G_T :Thermal gradient.

F_4: force determined by separation pressure. This force is negligible for meniscus length h>0.1

F_5: gravity force

$$F_5 = 4/3\ \pi r^2\ \rho_g\ g \tag{3.6}$$

Where ρ_g is gas density.

This equilibrium depend on the thermal gradient. Figure 3.20 shows the forces distribution around one bubble in the liquid.

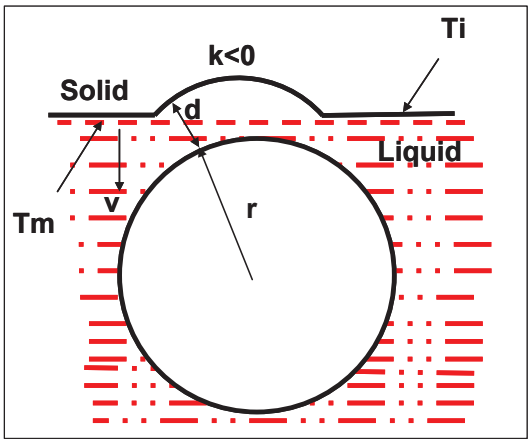

Figure 3.20 Bubble effect on the shape of the crystallization interface

If the bubble radius is less than 10^{-5}m, the last three forces can be negligible.

The bubble in the liquid affect the crystallization interface and practically the interface temperature (figure 3.20). Following Rempel et al. [9], the interface temperature is given by the following formula:

$$T_l = T_m - (T_m - \sigma_{SL} / \rho_s q_m)k - T_m (\lambda/d)^v \quad (3.7)$$

T_l-Interface temperature, T_m -Crystallization temperature for flat interface, σ_{SL}-Superficial tension ρ_s:Solid density, q_m:Heat flow, k-interface curvature, λ-length characteristical of intermolecular interaction, d-distance between position corresponding to flat interface and the new interface position, v- parameter depending on the interaction type (=3 for Van der Waals interaction).

The bubbles penetration in sapphire crystals is not only determined by the crystallization process, but it depend also on the surface process complexity. As we presented in the above section, the bubble origin can be connected to starting charge (Alumina powder). The bubbles can be rejected by the crystal if the growth speed don't exceed a critical value ($Vc \approx 10^{-5}$–10^{-3} cm/s for inclusions of size 10^{-4}–10^{-2}) [10]. This critical rate depends on the fluid and bubbles nature. It appears that the thermal conductivity ratio is an important factor for this process. It is clear that, before its incorporation the bubble is by some way attracted by the solid-liquid interface, to which they are separated by a thin liquid layer. Interaction of a particle with the interface has been studied for a long time [9,10,11,12,13]. It includes the disjoining pressure, electrostatic force, capillarity and the viscosity of the liquid film between the bubble and the interface. The attractive or repulsive behaviour of the interface depends on the relative amplitude of these forces and on the particle diameter; a clear review of the various phenomenon included in the models is given in ref. [15]. Keeping in mind that liquid alumina is a bit electrically conductive, electrostatic effects are likely to play a role in the stabilization of the bubble position close to the interface.

3.3.9 The propositional means to eliminate bubbles

From the discussion of the sections 3.3.1 to 3.3.7, it is very clear about the bubbles origin, penetration, distribution, and how the pulling rate and rotation rate influence the bubbles density. Therefore we can try to eliminate the bubbles from the

following aspects:

- The raw material---- decrease the proportion of α-Al_2O_3 powder, as much as possible to use sapphire crackle as raw material. If needed to use α-Al_2O_3 powder, try to choose more higher quality.
- The pulling rate---- lower pulling rate means more stable flat crystallization process, at the same time the production cost and efficiency should be taking in account, so one should employ as possibly high speed simultaneously without bubbles being captured. In the future work, it is suggested to try the pulling rate lower than 1.5 mm/h.
- The rotation rate---- rotation rate is a significant merit of Cz technique, it comes into being the forced convective flow from the center to the side, which is beneficial to get more uniform temperature field, and help the bubbles away from the crystallization zone finally possible to escape from the interface. But if the rotation rate exceeds a critical value, the growth front will be acutely disturbed, that is harmful to the crystal growth. In this research, comparing all the data, it is suggested that the appropriate value of rotation rate should be 8 rpm.

3.4 Optical characterization

The main topic of this thesis is bubbles study in undoped and Ti-doped sapphire (next chapter) grown by Cz technique. But we have also extendes our research program to the optical characterization of the grown crystal to investigate the bubbles effect on the optical properties and crystals performance. As a function of the growth conditions, we have grown more than twenty sapphire ingots by Cz technique. But because of the time and also the cost of cutting and polishing, we have selected some crystals to study their optical characterization.

3.4.1 X-ray rocking curve

To characterize the crystal perfection, XRC measurement was performed on the wafers cut from three sapphire single crystals ingots grown along a-axis. The selected

wafers were collected from the middle of the ingot area exempt of bubbles or contain a few amount of bubbles. The growth parameters are shown in table 3.2. All XRCs (figure 3.21) show Gaussian symmetrical single peak, without any additional or shoulder peak, which indicates the good and the perfect sapphire crystallinity. Not low angle grain no boundary or mosaic structure are observed in the grown crystals.

Table 3.2 Cz technique growth parameters of sapphire crystals for XRC measurement

Number of crystals	orientation	Pulling rate (mm/h)	Rotation rate (rpm)
1	A[$11\bar{2}0$]	3	8
2	A[$11\bar{2}0$]	5	8
3	A[$11\bar{2}0$]	3	10

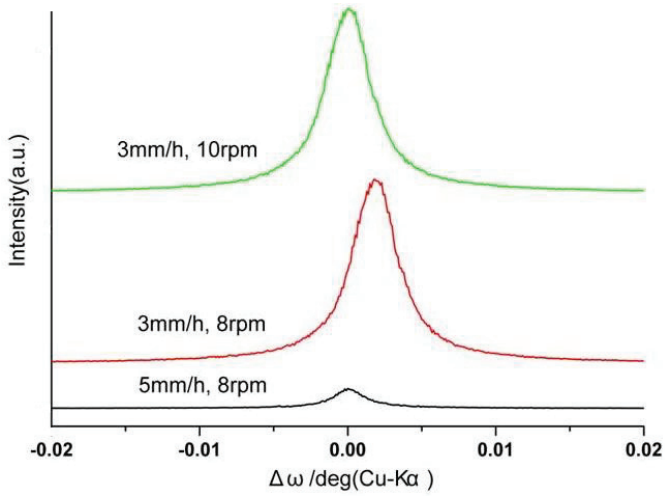

Figure 3.21 XRCs of sapphire crystals grown along a-axis [$11\bar{2}0$]

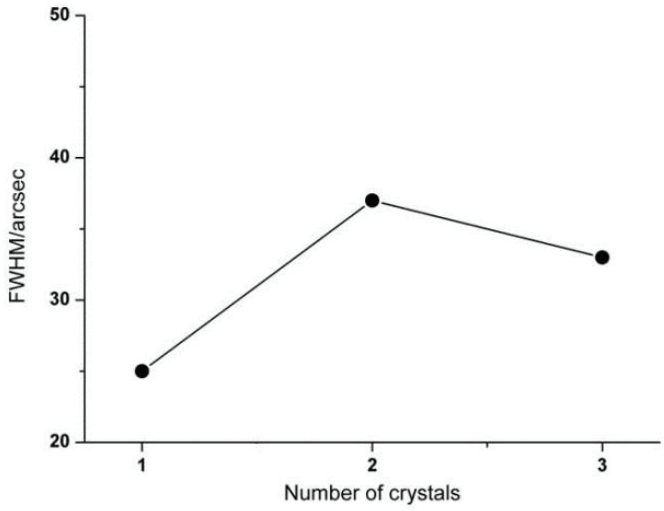

Figure 3.22 FWHM comparison of XRCs in figure 3.21

All FWHM values calculated from the X-ray rocking curves of ω-scan are less than 40 arcsec, this result suggests that the grown sapphire crystals have acceptable crystallinities. The bubbles defects have no damage to the crystallintiy. FWHM values of the three crystals were compared as shown in figure 3.22. For the same pulling rate, lower rotation rate resulted in a higher crystallity. For the same rotation rate, lower pulling rate had better crystallinity. However, the difference is not so significant, all sapphire single crystals grown by Cz technique have good qualities. So from these results, we can consider that our technology is able to grow a perfect sapphire single crystal without any microscopic defects such dislocations, grains boundary, twin and mosaic which strongly decrease the sapphire optical performance.

3.4.2 Raman spectra

To study the information of molecular structure of sapphire crystals, Raman spectrum was measured on sapphire crystals grown by Cz technique. Figure 3.23 and figure 3.29 show Raman spectra of sapphire crystals grown along a-axis and r-axis respectively, and the spectra obtained were compared with the standard spectra in the database RRUFF^{TM} which got from well characterized corundum. The results indicate that the structure of our sapphire crystals are exactly same as corundum.

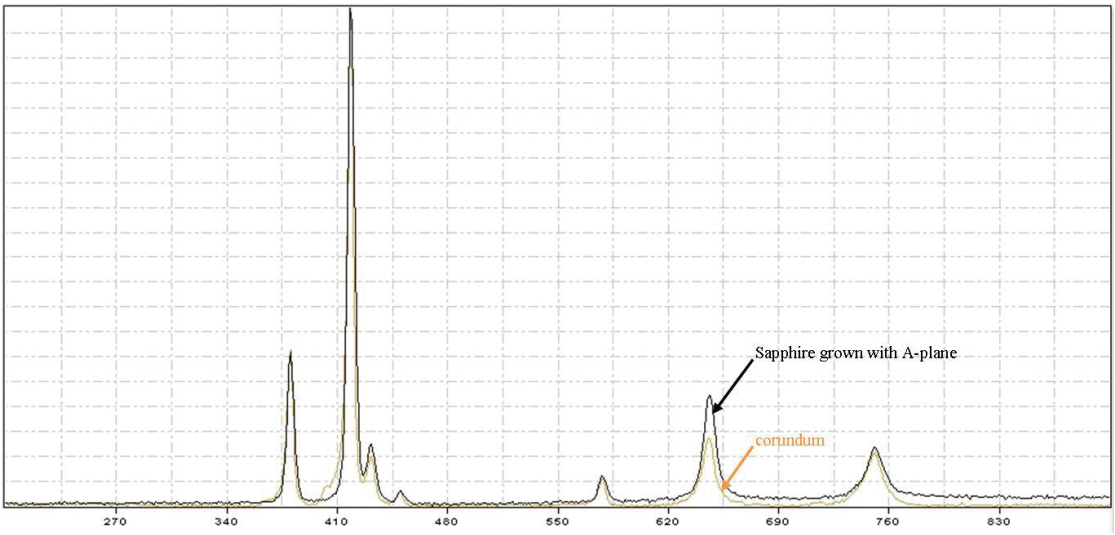

Figure 3.23 Raman spectrum of sapphire crystal grown along a-axis compare with spectrum of corundum

Figure 3.24 and figure 3.28 were labeled 7 characteristic peaks of alumina: 378 cm^{-1}, 418 cm^{-1}, 432 cm^{-1}, 450 cm^{-1}, 578 cm^{-1}, 645 cm^{-1}, 751 cm^{-1}, which are well agree with the spectrum of natural corundum, the seven bands are based on the D^6_{3d} symmetry of corundum and $2A_{1g} + 5E_g$ active phonon modes .

Figure 3.25 and figure 3.29 present Raman spectra measured of top (beginning), middle and end parts of sapphire crystals grown along a-axis and r-axis. Figure 3.26 and figure 3.30 present Raman spectra measured on edge region and center region of the wafers cut from sapphire crystals grown along a-axis and r-axis. Figure 3.31 presents Raman spectra measured of sapphire crystals grown at different pulling rate (1-1.5 mm/h, 2-2.5 mm/h, 3-3 mm/h, 4-5 mm/h) with rotation rate 8 rpm, figure 3.32 presents Raman spectra measured of sapphire crystals grown at different rotation rate with pulling rate 2.5 mm/h. No matter the sapphire crystals grown along a-axis or r-axis, no matter different pulling rate or rotation rate, no matter top (beginning), middle or end part of sapphire crystal, no matter edge region or center region of the wafers cut from sapphire crystals, their Raman spectra indicate a pure, regular structure of α-alumina. No Raman shift caused by inclusion or other large defects been observed.

The results of Raman spectra indicate that no obvious defects were detected in the sapphire crystals grown by Cz method. The bubbles defects had no any influence on sapphire structure. No matter what the growth speed or the rotation speed were employed, the sapphire structure had good agreement with corundum.

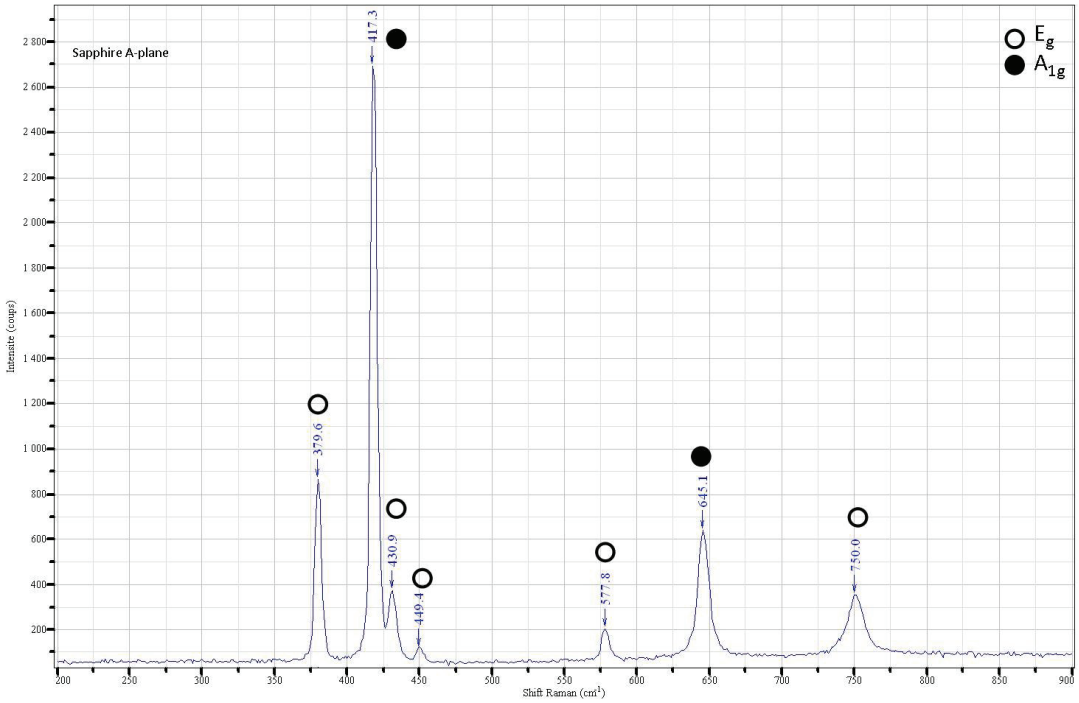

Figure 3.24 Characteristic peak of Raman Spectrum of sapphire crystal grown along a-axis

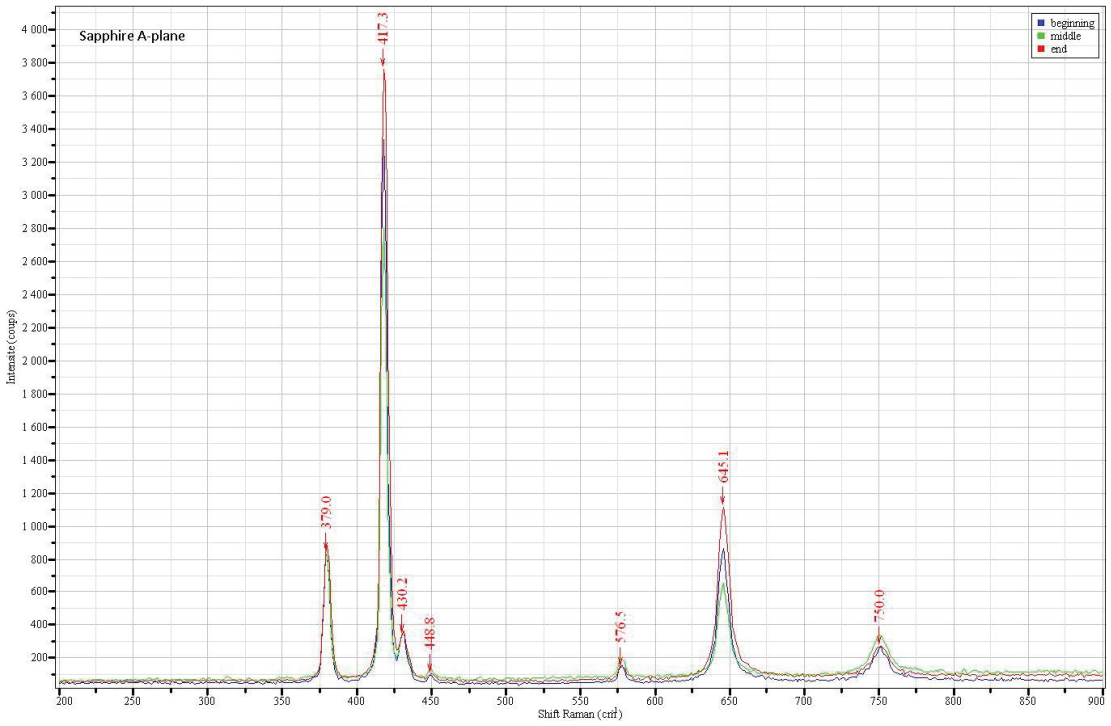

Figure 3.25 Raman Spectra measured at different position of sapphire crystal grown along a-axis

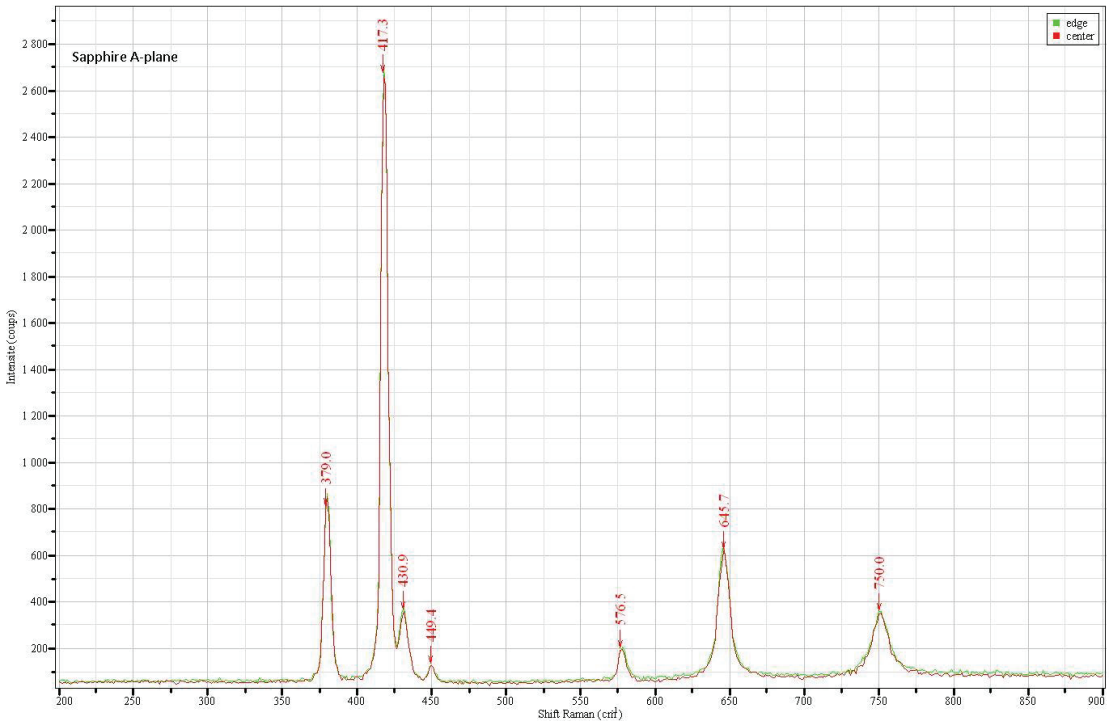

Figure 3.26 Raman Spectra measured at different position of the wafer cut from sapphire crystal grown along a-axis

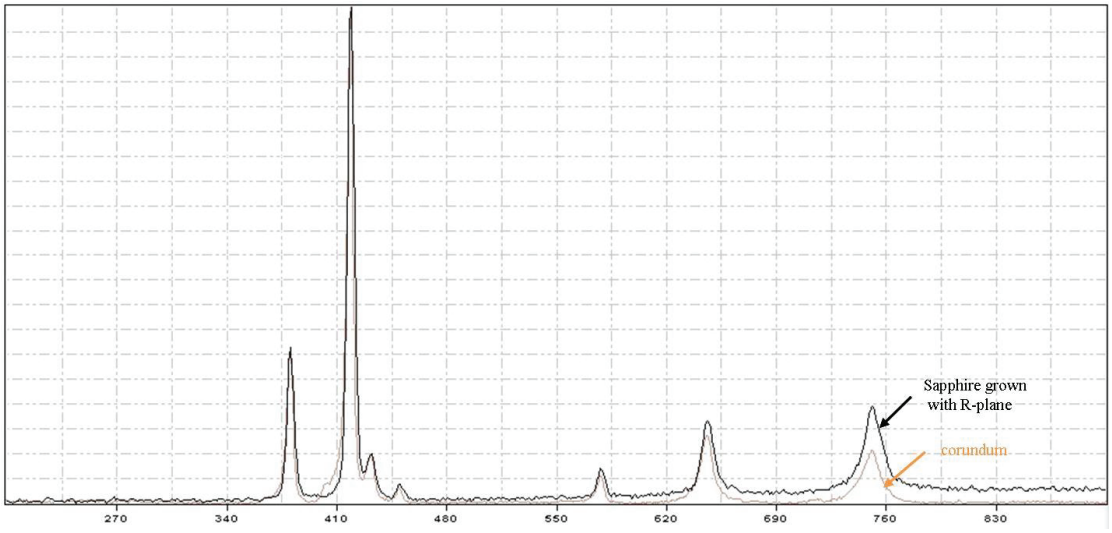

Figure 3.27 Raman spectrum of sapphire crystal grown along r-axis compare with spectrum of corundum

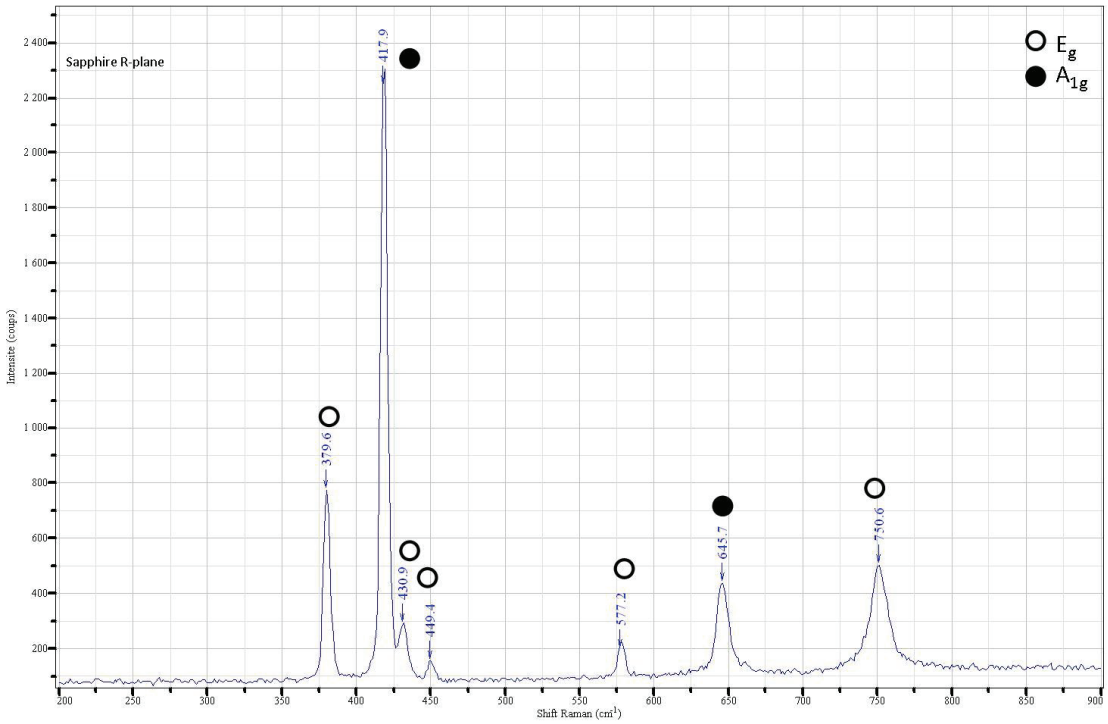

Figure 3.28 Characteristic peak of Raman Spectrum of sapphire crystal grown along a-axis

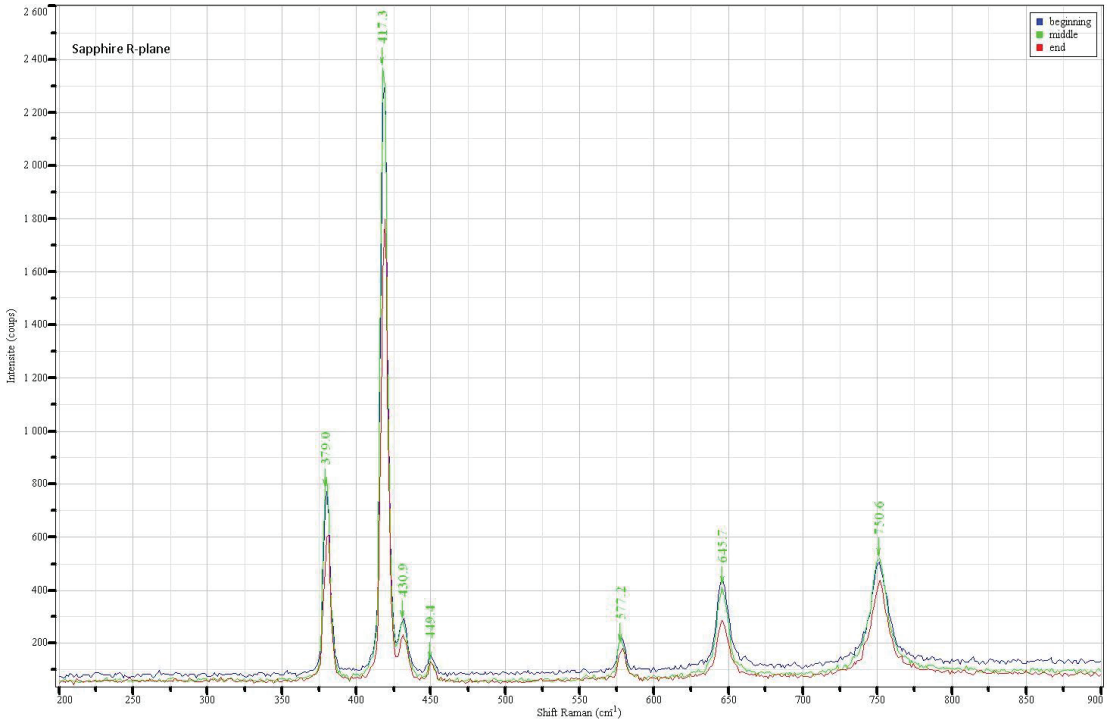

Figure 3.29 Raman Spectra measured at different position of sapphire crystal grown along r-axis

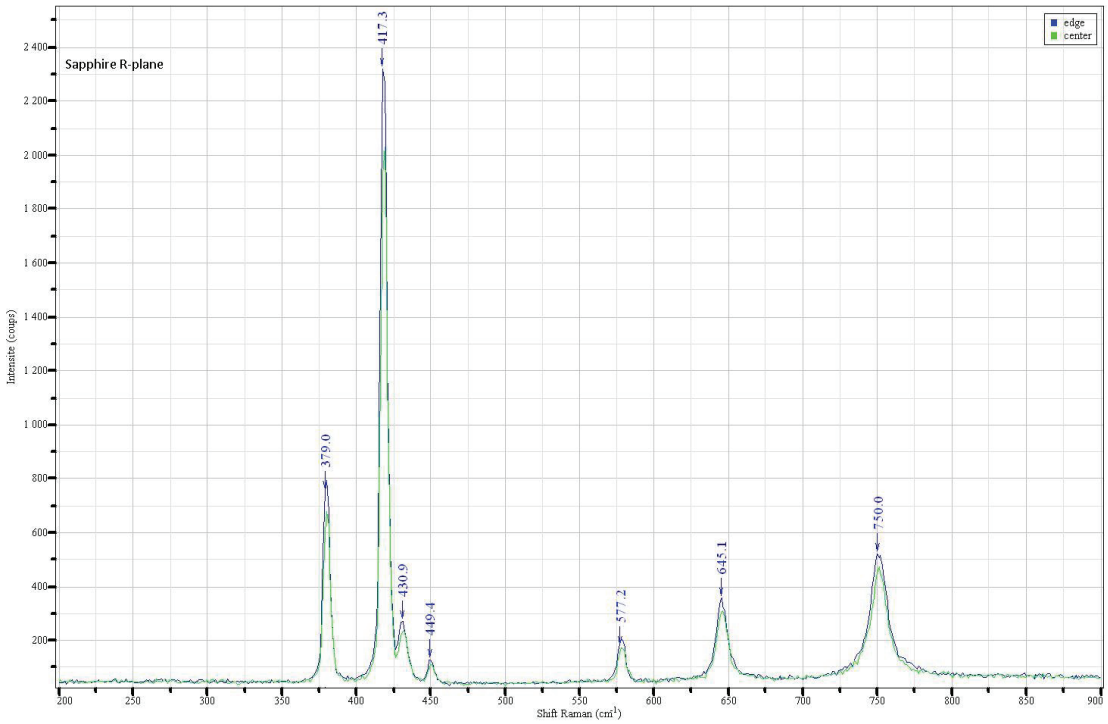

Figure 3.30 Raman Spectra measured at different position of the wafer cut from sapphire crystal grown along r-axis

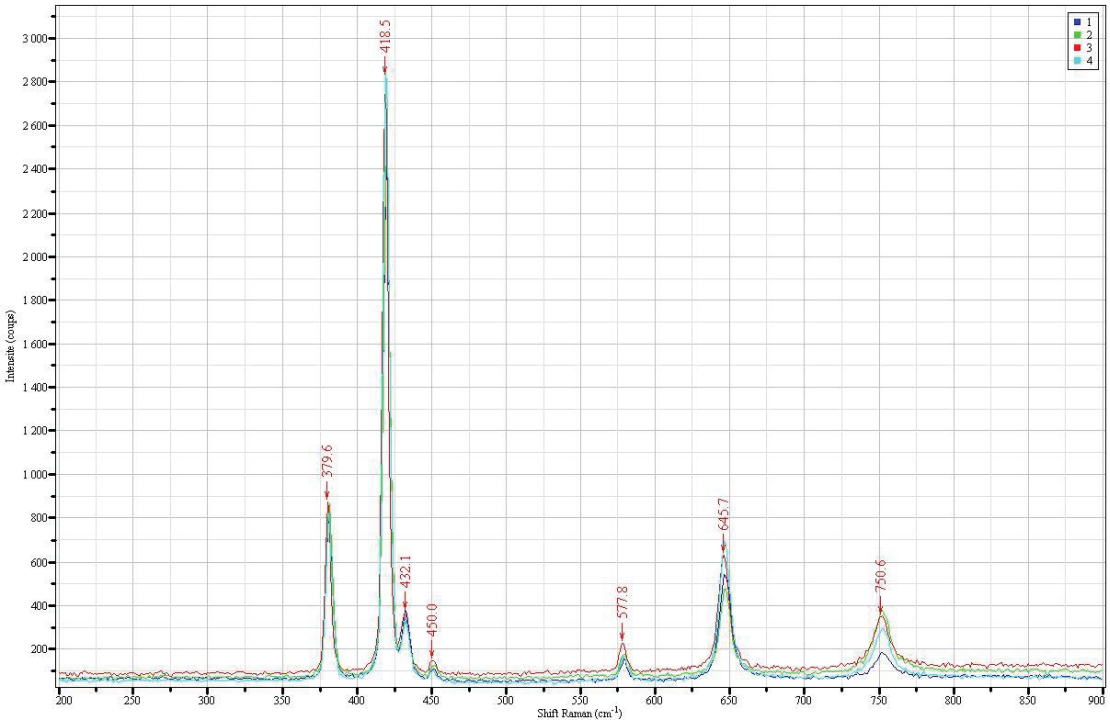

Figure 3.31 Raman spectra measured of sapphire crystals grown at different pulling rate (1-1.5 mm/h, 2-2.5 mm/h, 3-3 mm/h, 4-5 mm/h) with rotation rate 8 rpm

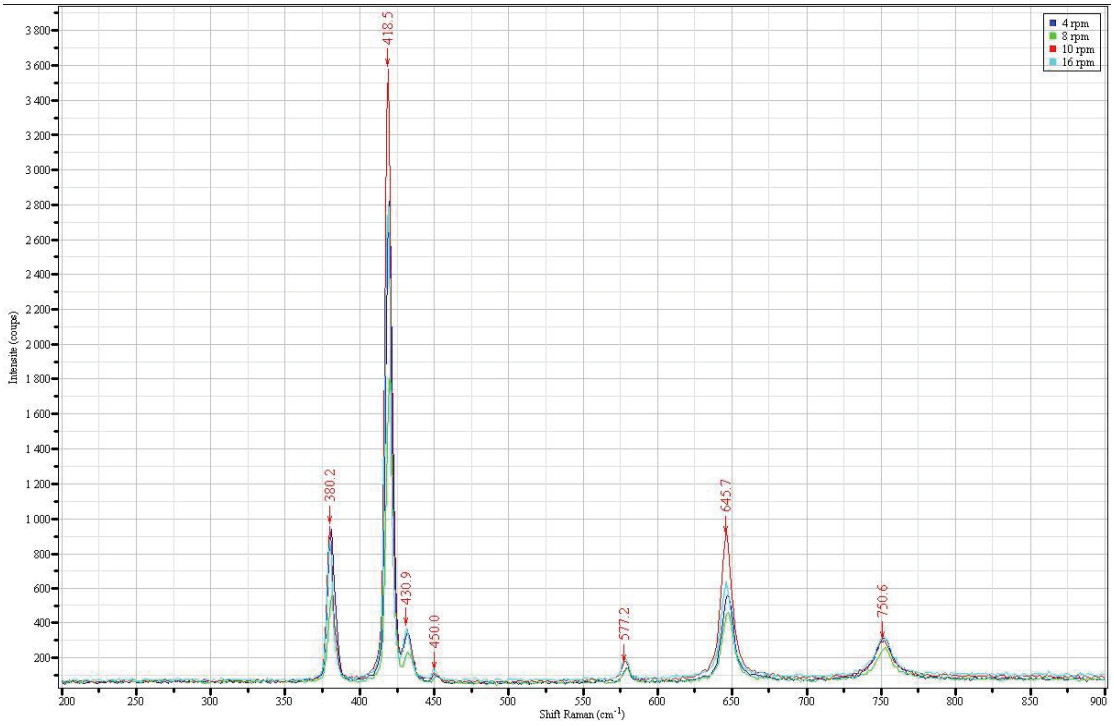

Figure 3.32 Raman spectra measured of sapphire crystals grown at different rotation rate with pulling rate 2.5 mm/h

3.4.3 Absorption spectra

The sapphire crystals grown by Cz method were cut into wafers perpendicular to growth direction, and optically polished. Five samples were chosen and performed absorption spectra at room temperature. The growth parameters of these 5 samples were listed in table 3.3. The thickness of the samples is 2 mm, they were grown along a-axis and r-axis respectively, the pulling rate is from 1.5 to 5 mm/h, the rotation rate is 8 rpm. In this measurement, the utilized light source has no polarization.

Table 3.3 The parameters of 5 samples for absorption

sample	Orientation	Pulling rate (mm/h)	Rotation rate (rpm)	Thickness (mm)
1(CrysU5)	a[$11\bar{2}0$]	5	8	2
2(CrysU8)	r[$10\bar{1}2$]	3	8	2
3(CrysU3)	a[$11\bar{2}0$]	2.5	8	2
4(CrysU7)	r[$10\bar{1}2$]	2	8	2
5(CrysU1)	a[$11\bar{2}0$]	1.5	8	2

In figure 3.33, a weak absorption band with the peak point about 255 nm can be observed from the spectrum of sample 1, 1A→1B transition of F^+ center should be

responsible for this absorption band [16]. Except this weak absorption band at 255 nm of sample 1, no other absorption had been observed in sample 2, 3, 4 and 5. As we discussed in chapter 2.3.7, there is a relationship between the absorption coefficient and the thickness of the sample according to the law of Lambert-Beer. But in our case, the thickness of 5 samples is same. Compare the growth parameters of the 5 crystals, sample 1 was grown at the most high growth rate—5 mm/h, so the F^+ center is mainly caused by high growth rate. There are some researchers observed absorption bands at 204 nm, 206 nm and 232 nm [16][17][18][19], absorption band at 204 nm was ascribed to F centers, bands absorbing at 296 and 232 nm were ascribed to F^+ centers. But all these absorption were not observed in our sapphire crystals.

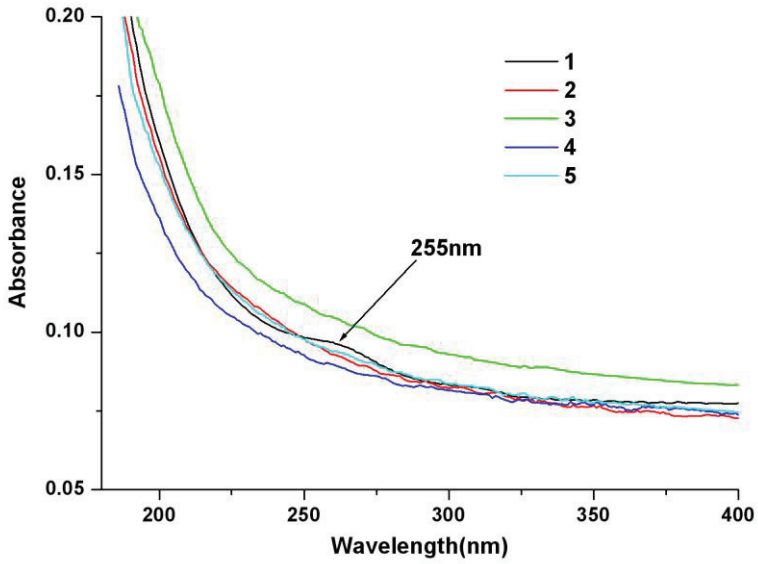

Figure 3.33 Absorption spectra of the grown sapphire crystals by Cz technique
(the reference of samples see table 3.3)

The absorption results demonstrate that, when the pulling rate<5 mm/h (rotation rate 8 rpm), the as-grown sapphire crystals possess high optical quality, no obvious defects were observed. While the crystal grown at high growth rate (5 mm/h, 8 rpm) contained a few quantity of F^+ color centers. It's mainly due to the crystallization process at high speed is more stabilization than at low speed, so more O^{2-} vacancies were created.

3.4.4 Transmission

The method how to measure transmission values and the meaning of comparison in transmission values were introduced in the section 2.2.6. In this measurement, all the samples were placed parallel to the polarization direction of the laser source (He-Ne laser, 633 nm). Figure 3.34 shows transmission of the sapphire crystals as a function of pulling rate with rotation rate 8 rpm. For low pulling rate (v≤2 mm/h) the transmissions exceeded 82% at room temperature. However, the transmission slightly decreased at higher pulling rate. This is most probably related to the increasing of the density of the bubbles that absorb the light in the measurement range and strongly affect the optical properties.

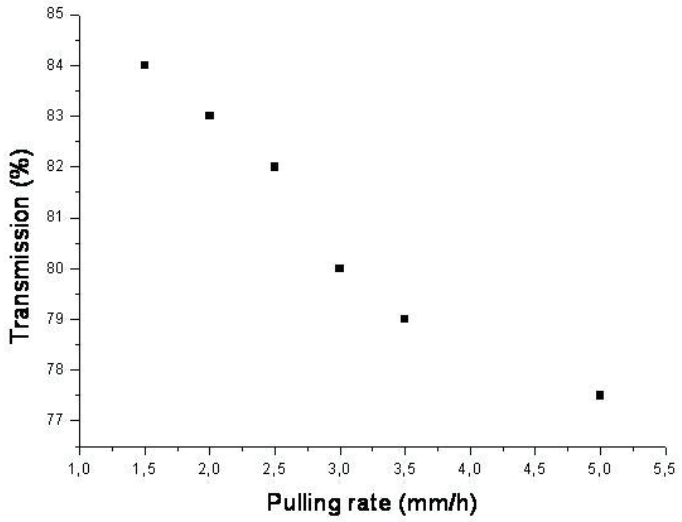

Figure 3.34 Polarized transmission evolution as a function of pulling rate (V_r=8 rpm)

Figure 3.35 shows transmission of the sapphire crystals as a function of rotation rate with pulling rate 2.5 mm/h. For low rotation rate (v≤8 rpm) the transmissions exceeded 82% at room temperature. While at higher rotation rate (v≥10 rpm), the transmission decreased distinctly. The decreasing of the transmission when rotation rate>10 rpm is most probably related to the increasing of the density of the bubbles that absorb the light in the measurement range and strongly affect the optical properties.

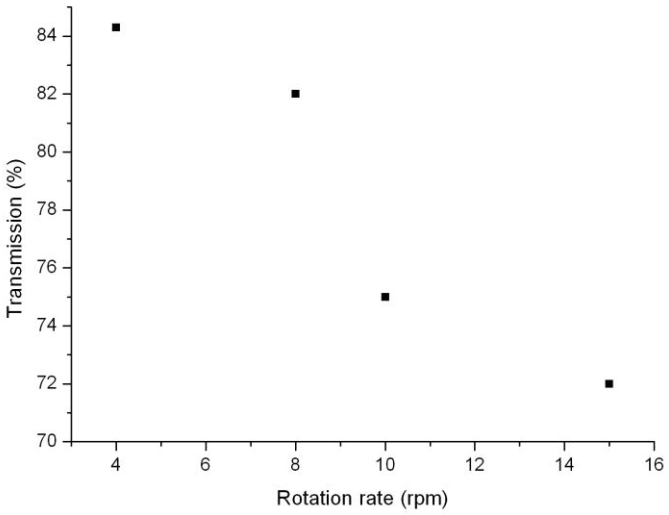

Figure 3.35 Polarized transmission evolution as a function of rotation rate (V_g=2.5mm/h)

3.4.5 Photoluminescence spectra

The measurements were performed using an EQ-99 broadband Laser-Driven Light Source (LDLS) from Energetic coupled with a Jobin Yvon Gemini 180 monochromator as excitation source. The luminescence is collected with a UV fiber to a Jobin YvonTriax 320 monochromator and detected by a Jobin Yvon 3000V CCD camera. This setup allows obtaining excitation emission amplitude map of the sample luminescence. This type of map presents in abscissa the excitation wavelength and inordinate the luminescence emission wavelength. This graphical representation permits to distinguish easily the luminescence emission in function of the excitation wavelength.

The luminescence of two sapphire samples was measured. Sample 1 was obtained from the crystal grown at pulling rate 3 mm/h and rotation rate 8 mm/h, sample 2 was obtained from the crystal grown at pulling rate 5 mm/h and rotation rate 8 mm/h. In figure 3.36 the excitation-emission amplitude maps in the excitation range 190-300 nm of sample 1 and sample 2 are reported. In figure 3.36a it is possible to observe two different emissions of sample 1: one centered around 330 nm for excitation at 260 nm; and a second one around 430 nm for excitation at 220 nm. The emission at 330 nn is attributed F^+ center [20]. The weak emission around 425 nm

should be attributed to the F color center. The maximum emission of F center in sapphire is normally around 413 nm for excitation at 205 nm [20], but unfortunately the experimental setup has too much noise on this area to record correctly this luminescence.

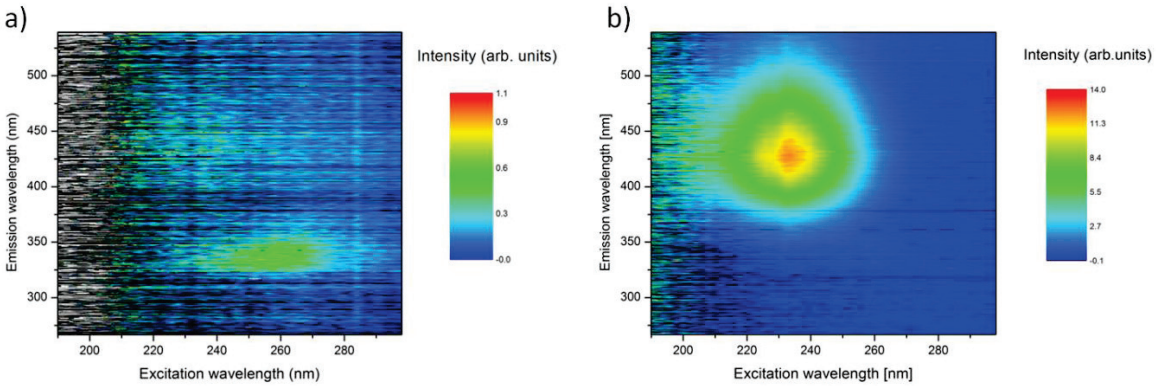

Figure 3.36 Emission amplitude maps for two sapphire samples in the excitation range 190-300nm in a) sample 1; and in b) sample 2.

In figure 3.36b, for an excitation at 230 nm a strong emission around 430 nm is observed on the sample 2. This emission is also well known in Ti-doped sapphire [21][22][23]. This luminescence can be explained by the following model: The raw material alumina powder contains very small quantity of titanium impurities. At first, the 230 nm excited a charge transfer from Ti^{3+} to F^{+}, then a F* center at excited state created, the transition of F* center to ground state emitted 420 nm photons [24]. With the increasing of the growth rate, more F^{+} centers were created in sample 2. This big amount of F^{+} centers in allowed efficient charge transfer mechanism from Ti^{3+} to F^{+}. In sample 1 this charge transfer was possible to occur also, however, there are less F^{+} centers in sample 1 than in sample 2, and which reduced drastically this emission.

Moreover, as shown in figure 3.37, sample 2 presents a luminescence emission around 600 nm in excitation at 230 nm, whereas, this emission was not observed in the sample 1. This emission is not clearly assigned but it is certainly due to a transfer from F^{+} center to impurity or another defect.

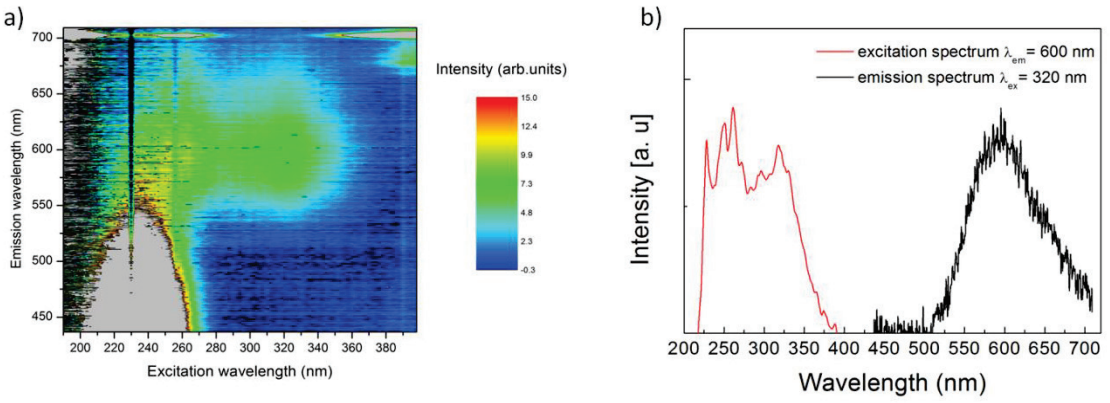

Figure 3.37 Emission amplitude maps for sample 2 in the excitation range 190-400nm a); and b) excitation and emission spectra of the luminescence around 600 nm in sample 2.

The figure 3.38 presents the luminescence around 700 nm due to the presence of Cr^{3+} ion in the two samples. The luminescence measurements exhibit the presence of color center or impurity like Cr^{3+} and Ti^{4+} in the samples. The luminescence of sample 1 growing with a lower growth rate presents less F^{+} center than which of the sample 2, therefore demonstrates a better quality of the crystal.

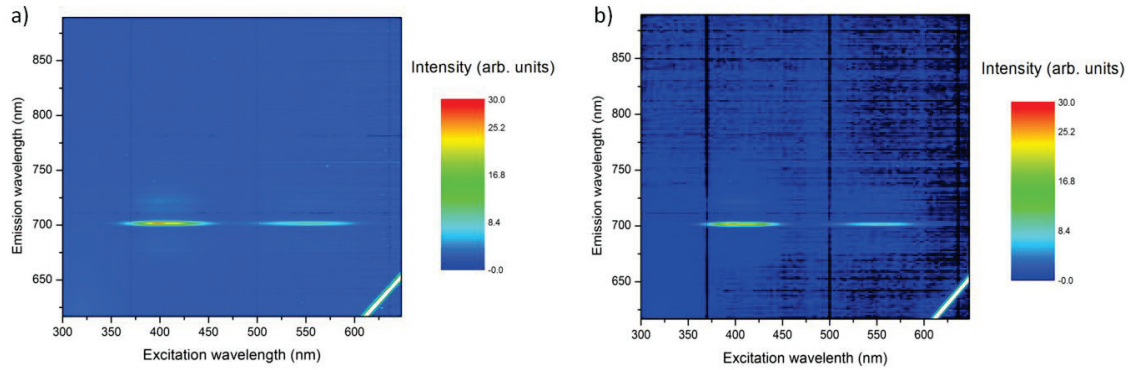

Figure 3.38 Emission amplitude maps for two undoped sapphire samples in the excitation range 300-650 nm in a) sample 1; and in b) sample 2.

3.4.6 Wavefront measurement

A focused beam from He-Ne laser was sent through the wafers. The diameter of the laser waist without sample was measured to be 140 µm. A focal imaging system was used to image the end face of the sample into the beam analyzer Beamwave 500 from Phaseview. The analyzer recorded the beam and the wavefront profiles. The Getlase software was used to analyze the beam profile and to calculate the coefficients

of the wavefront decomposition using Zernike polynomials. The wavefront profile measured without sample was perfectly plane (RMS=16 nm).

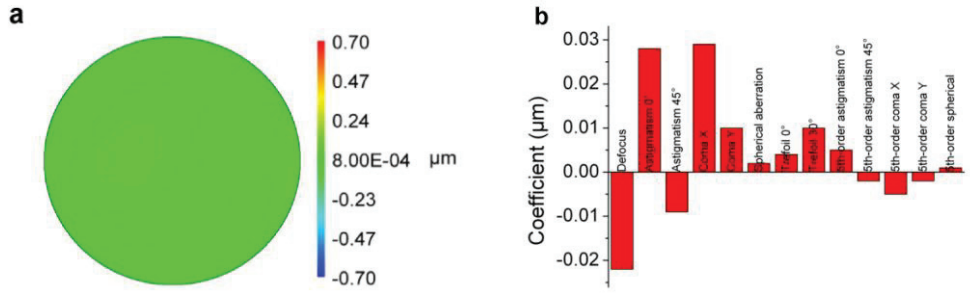

Figure 3.39 Wavefronts obtained from a 5mm thickness and 30mm diameter wafer of sapphire crystal grown under stationary regime (V_g=1.5 mm/h and V_r=8 rpm). (a) Wavefront profile measurement for the laser propagation in the wafer; (b) Zernike coefficient histogram obtained from the (a) wavefront profile.

Figure 3.39a shows wavefronts recorded using 5 mm thickness and 30 mm diameter wafer cut from the sapphire crystal grown under stationary regime (V=1.5 mm/h), the crystal contains very few bubbles, 21 nm RMS phase deformation was measured in the wavefront profile after propagation through the wafer. Figure 3.39b shows the histograms featuring pertinent terms in the Zernike decomposition. The sample induced very small aberration in this area.

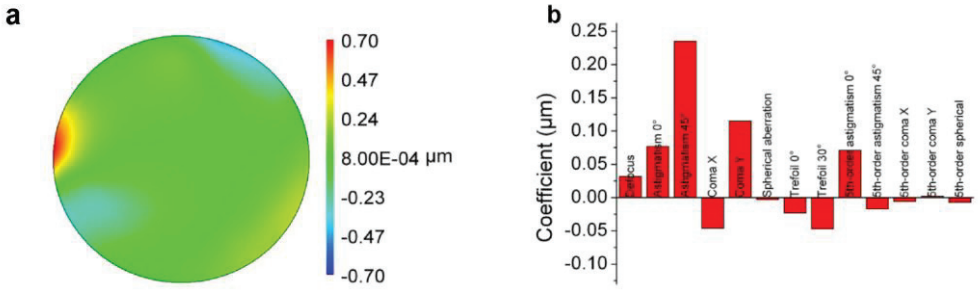

Figure 3.40 Weavefronts obtained from a 5mm thickness and 30mm diameter wafer of sapphire crystal grown under stationary regime (V_g=5 mm/h and V_r=8 rpm). (a) Wavefront profile measurement for the laser propagation in the wafer; (b) Zernike coefficient histogram obtained from the (a) wavefront profile.

Figure 3.40a illustrates the wavefront profile for the laser beam propagation in the center of the sapphire wafer grown with pulling rate 5 mm/h and rotation rate 8

rpm, this crystal contains comparatively more bubbles. The wavefront profile was modified by the sample (RMS=134 nm). The sample induced strong astigmatism aberrations (figure 3.40b).

3.4.7 Laser beam shape measurement

In order to visualize the effect of the bubbles on the intrinsic quality of the grown crystals, we have used a non-destructive analysis method based on the utilization of He/Ne laser emitting at 633 nm. A focused beam from the laser was sent through the optically polished wafer, the output intensity was recorded with a CCD digital camera connected to a computer. The region exempt bubbles show Gaussian profile of the transmitted laser beam (figure 3.41b). On the other hand, for the crystals containing bubbles, the beam profile was non-Gaussian and disturbed (figure 3.41c), which is due to the bubbles defects in sapphire crystals cause losses in the intensity profile as well as phase deformations.

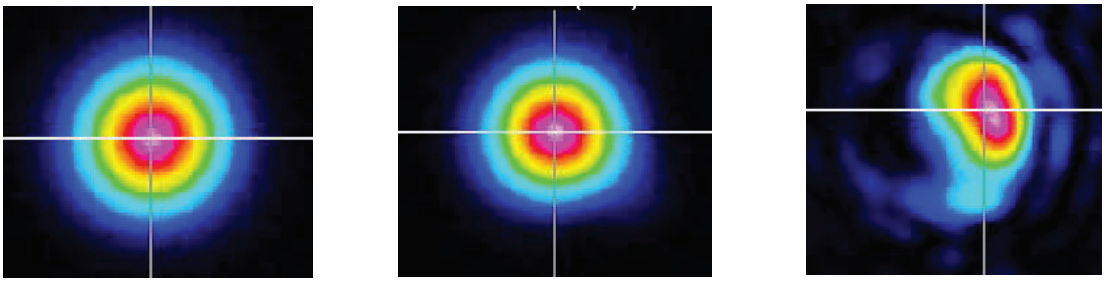

Figure 3.41 Intensity distribution in the He/Ne laser beam (P=0.95 mW) in air (a); and after light passing through the crystals grown at pulling rate of 1.5 mm/h (b); and 5 mm/h (c). Both cases rotation rate is 8 rpm. The crystals were cut from the middle of the ingot and were oriented along a-axis.

3.5 Conclusions

1. Undoped Sapphire single crystals were successfully grown by Cz method. They were grown along a-axis and r-axis, at different pulling rate and rotation rate, respectively. The as grown crystals were transparent and colorless, exempt from macroscopic defects. Micro bubbles were observed in the grown sapphire crystals. All the crystals had desirable crystallinity, their structures were well agreed with

corundum.

2. The crystal grown along a-axis, with pulling rate 1.5 mm/h and 8 rpm contained very little quantity of bubbles. The crystal grown at higher pulling rate or rotation contained high bubbles concentration. Most of the bubbles were distributed randomly in the crystal volume, and other presented arrays line perpendicular to growth direction. All bubbles were homogeneous and spherical, their diameters varied from 2 μm to 5 μm. Some adjacent small bubbles were connected and formed into large size "bubbles" which appeared irregular shapes.

3. The destabilization of solid-liquid interface results from the gas rejection. The order of bubbles density in the crystal is: top >end >middle. The bubbles density increased with the increasing of pulling rate. The optimized rotation rate should be kept 8 rpm or less than 8 rpm. The dissolved gas in raw material is supposed to be the main origin of bubbles, thermal decomposition of molten alumina is possibly to be supplementary origin of bubbles.

4. The crystals grown at lower speed have high optical quality. The polarized transmission decreased as a function of pulling rate and rotation rate due to the bubbles defect. F^+ color center was formed in the crystal grown at high speed (5mm/h), while the crystals grown with the pulling rate<5mm/h had no color center. The wavefront and laser beam shape experiments visibly indicate that the bubbles degrade the optical quality significantly.

5. To grow bubbles-free sapphire crystal, it is very important to use low pulling rate and low rotation rate allowing the obtainment of flat interface. Besides, it is very important to use sapphire crackle as starting charge instead alumina powder.

References:

[1] "http://www.cyberstar.fr." .

[2] E. A. Ghezal, H. Li, A. Nehari, G. Alombert-Goget, A. Brenier, K. Lebbou, M. F. Joubert, and M. T. Soltani, "Effect of Pulling Rate on Bubbles Distribution in Sapphire Crystals Grown by the Micropulling Down (μ-PD) Technique," *Cryst. Growth Des.*, vol. 12, no. 8, pp. 4098–4103, Aug. 2012.

[3] G. E. H. Ahmed, "Croissance cristalline de saphir non dopé préformé et étude des effets de la matière première et des vitesses de tirage sur la distribution des bulles et la qualité cristalline," L'UNIVERSITE CLAUDE BERNARD LYON 1, 2013.

[4] E. A. Ghezal, A. Nehari, K. . Lebbou, and T. Duffar, "Observation of Gas Bubble Incorporation during Micropulling-Down Growth of Sapphire," *Cryst. growth Des.*, vol. 12, pp. 5715–5719, 2012.

[5] S. E. Demina and V. V. Kalaev, "3D unsteady computer modeling of industrial scale Ky and Cz sapphire crystal growth," *J. Cryst. Growth*, vol. 320, pp. 23–27, 2011.

[6] C.-W. Lu, J.-C. Chenb, C.-H. Chenb, C.-H. Chenb, Wen-Ching Hsuc, and C.-M. Liu, "Effects of RF coil position on the transport processes during the stages of sapphire Czochralski crystal growth," *J. Cryst. Growth*, vol. 312, pp. 1074–1079, 2010.

[7] C. J. Jing, S. Ihara, K.-I. Sugioka, T. Tsukada, and M. Kobayashi, "Analysis heat transfer in CZ crystal growth," *J. Cryst. Growth*, vol. 310, pp. 204–213, 2008.

[8] Kh.S.BAGDASAROV, *High-temperature Crystallization From Melt*, Edit Print. Edit Print, 2003, p. 180.

[9] A. W. Rempel and M. G. Worster, "Particle trapping at an advancing solidification front with interfacial-curvature effects," *J. Cryst. Growth*, vol. 223, no. 3, pp. 420–432, Mar. 2001.

[10] A. A. . Chernov and D. E. Temkin, "Capture of Inclusions in Crystal Growth," in *Crystal Growth and Materials*, 1977, p. Chapter I.1.

[11] D. R . Uhlmann, B. Chalmers, Jackson, and K. A. J., "Interaction Between Particles and a Solid-Liquid Interface," *J. Appl. Phys.*, vol. 35, p. 2986, 1964.

[12] J. Cissé and G. F. Bolling, "The steady-state rejection of insoluble particles by salol grown from the melt," *J. Cryst. Growth*, vol. 11, no. 1, pp. 25–28, 1971.

[13] J. Pötschke and V. Rogge, "On the Behavior of Foreign Particles at an Advancing Solid-Liquid Interface," *J. Cryst. Growth*, vol. 94, pp. 726–738, 1989.

[14] D. K . Shangguan, S. Ahuja, and D. M. Stefanescu, "An analytical model for the interactions between an insoluble particle and advancing solid/liquid interface," *Met. Trans.*, vol. 23A, pp. 669–680, 1992.

[15] S. Sen, B. K. Dhindaw, D. M. Stefanescu, A. Catalina, and P. A. Curreri, "Melt convection effects on the critical velocity of particle engulfment," *J. Cryst. Growth*, vol. 173, no. 3–4, pp. 574–584, April 1997.

[16] K.H. Lee and J.H. Crawford, "Luminescence of the F center in sapphire," *Phys. Rev. B*, vol. 19, no. 6, 1979.

[17] P. W. Levy and G. J. Dienes, "Colour Centers Induced in Al_2O_3 by Reactor and Gamma-Ray Irradiation," in *Report of the Bristol Conference on Defects in Crystalline Solids,The Physical Society, London*, 1955, pp. 256–260.

[18] T. J. Turner and J. J. H. Crawford, "Nature of the 6.1-eV band in neutron-irradiated Al_2O_3 single crystals," *Phys. Rev. B*, vol. 13, no. 4, pp. 1735–1740, 1976.

[19] G. Zhou, Y. Dong, J. Xu, H. Li, J. Si, X. Qian, and X. Li, "Φ140 mm sapphire crystal growth by temperature gradient techniques and its color centers," *Mater. Lett.*, vol. 60, pp. 901–904, 2006.

[20] J. H. Crawford, "DEFECTS AND DEFECT PROCESSES IN IONIC OXIDES: WHERE DO WE STAND TODAY?," *Nucl. Instruments Methods Phys. Res. Sect. B Beam Interact. with Mater. Atoms*, vol. 1, no. 2–3, pp. 159–165, 1984.

[21] A. Lupei, V. Lupei, C. Ionescu, H. G. Tang, and M. L. Chen, "SPECTROSCOPY OF Ti^{3+}: Alpha-Al_2O_3," *Opt. Commun.*, vol. 59, no. 1, pp. 1–3, 1986.

[22] G. Blasse and J. W. M. Verweij, "The luminescence of titanium in sapphire laser material," *Mater. Chem. Phys.*, vol. 26, no. 2, pp. 131–137, Oct. 1990.

[23] P. S. Page, B. S. Dhabekar, B. C. Bhatt, a. R. Dhoble, and S. V. Godbole, "Role of Ti^{4+} in the luminescence process of Al_2O_3:Si,Ti," *J. Lumin.*, vol. 130, no. 5, pp. 882–887, May 2010.

[24] V. B. Mikhailik, P. C. F. Di Stefano, S. Henry, H. Kraus, and A. Lynch, "Studies of concentration dependences in the luminescence of Ti-doped Al_2O_3," *J. Appl. Phys.*, vol. 109, no. 053116, 2011.

Chapter IV

Results & Discussions: Ti-sapphire crystal

The Cz technique was used to grow Ti-doped sapphire crystals. The crystals were grown along a-axis and r-axis, with different growth rate and titanium concentration respectively. Bubble-free and high-FOM Ti-sapphire crystals were obtained under optimized growth parameters. The crystallinity and structure of the as grown Ti-sapphire crystals were analyzed. Optical microscopy and other complementary techniques were used to study the bubbles creation and titanium segregation. The difference of bubbles size and their distribution between sapphire and Ti-doped sapphire crystals were discussed.

4.1 Ti-doped sapphire crystals grown by Cz technique

Ti-sapphire crystals were grown along a-axis and r-axis respectively, pulling rates were from 1.5 to 4 mm/h, rotation rate was 8 rpm. Doping with Ti used as TiO_2 powder (99,99% purity) in the range 0.1-0.3atom%. In some cases, we have also used Ti-doped sapphire crackle crystallized by Ky and Verneuil techniques. As already observed in undoped sapphire, the crystals grown along a-axis are faceted and the ones grown along r-axis have circular geometry. The geometry of the shoulder (beginning) and the tail (end) of the grown crystals depend on the growing parameters program selected in the pulling software [1]. The profile of the grown boules is cylindrical with good symmetry and uniformity. The cylindrical profile has been adjusted by varying the crystal growth parameters, so that the heat power and pulling rate are automatically changed. The crucible was not rotated during the growth. After the growth run, the crystal was cooled at approximately 30°C/h down to room temperature (25°C). The diameter of the crystal from the growth is same as the diameter in the parameter growth (30 or 35 mm). The diameter of the crystal increased when the growth was around the equilibrium temperature of the system. As the growth progressed, the diameter of the growing crystal was controlled by adjusting the crucible temperature. Lowering the heating power will accelerate the crystallization and lead to an increased diameter, while increasing the power will decrease the diameter of the crystal.

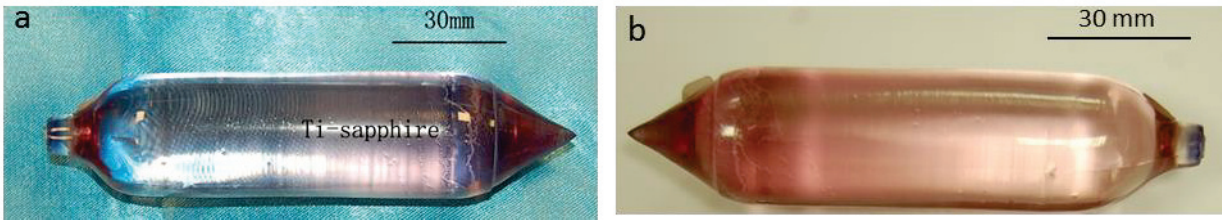

Figure 4.1 Ti-doped sapphire crystals grown by Cz technique (diameter of crystals = 30 mm) (a) Ti-doped sapphire crystals grown along r-axis, and (b) a-axis.

Figure 4.1 shows the typical crystal boules of Ti-doped sapphire grown in ILM laboratory by the Cz technique. In the same figure is Ti-doped sapphire crystals along r-axis (figure 4.1a) and a-axis (figure 4.1b) , grown at pulling rate 1.5 mm/h, rotation rate 8 rpm, starting titanium concentration 0.10 atom%. The crystals were transparent, pink (because of titanium dopant), and exempt of visible macroscopic defects such as bubbles and cracks. The Ti-sapphire crystal grown along a-axis, pulling rate 2.5 mm/h, rotation rate 8 rpm and titanium concentration 0.28 atom% in the melt, contained a few bubbles in the top and high bubbles concentration at the end part of the crystal. The middle part was bubbles free (figure 4.2). While it is more obvious in figure 4.3, the Ti-sapphire crystal grown along a-axis, 4 mm/h, 8 rpm, Ti-concentration 0.5 atom%, contained a few bubbles in the top part, no bubbles in the middle part. The end part of this crystal contain more bubbles and strong visible titanium segregation was observed. This part (segregation phenomenon) will be discussed in detail in the next sections.

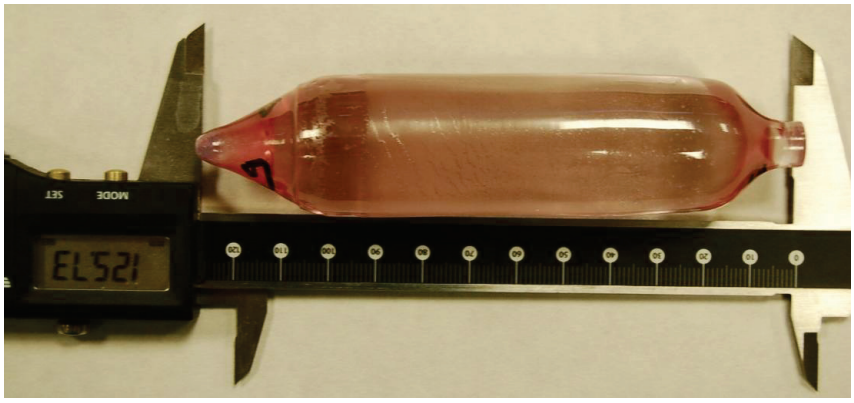

Figure 4.2 Ti-doped sapphire crystal grown along r-axis (diameter 30 mm) and initial titanium concentration in the melt is 0.28 atom%

Figure 4.3 Ti-sapphire crystal grown along a-axis, 4 mm/h, 8 rpm, Ti concentration 0.5 atom%

As in the case of undoped sapphire crystals, three parts (top, middle and end) of each Ti-doped sapphire ingot were cut into wafers of 5 mm in thickness (figure 4.4), then optically polished in cristalinnov plateform and characterized. The facets were clearly observed.

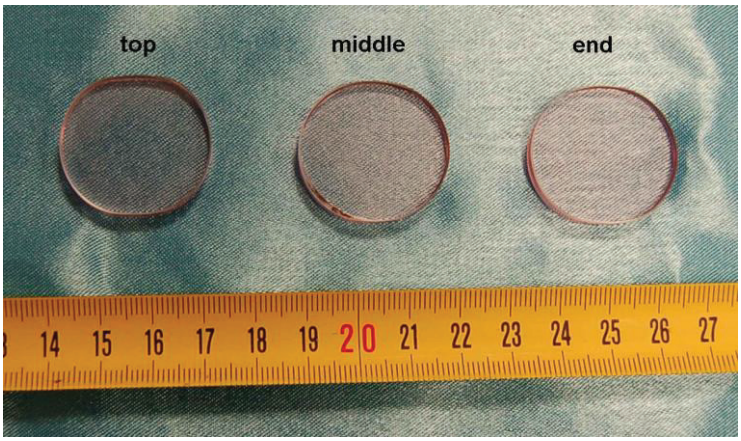

Figure 4.4 Optically polished Ti-sapphire wafers
(5mm thickness, cut from the crystal grown along a-axis)

4.2 Bubbles characterization

4.2.1 The distribution of bubbles

The Ti-doped sapphire crystal grown with low pulling rate (V≤1.5 mm/h) and rotation rate 8 rpm present a good surface morphology without bubbles presence. Figure 4.5 shows the surface of one wafer cut from the middle of the ingots grown along a-axis. The same results have been obtained in the case of the crystal grown along r-axis. The wafers don't contain bubbles and even if the melt contain bubbles,

with such growth condition the bubbles are not trapped by the crystal. An another hand, whatever the seed orientation, the crystals grown at high pulling rate (V>1.5mm/h) contain at the beginning and the end parts of the crystals bubbles concentered in the center of the wafer (figure 4.6).

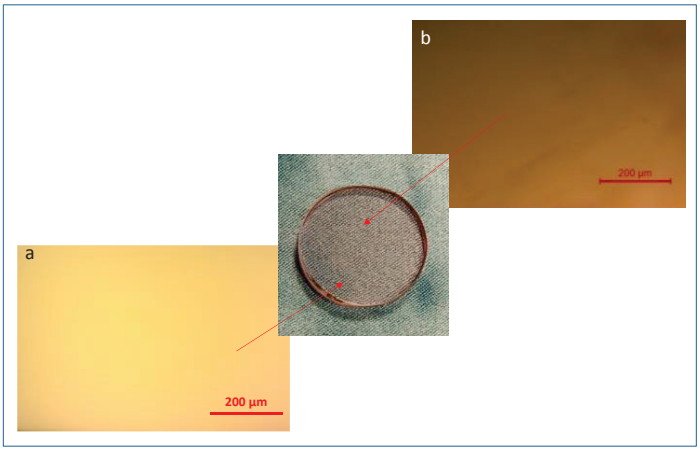

Figure 4.5 Optical microscopy analysis of Ti-doped sapphire crystal wafer cut from ingot grown along a-axis (V_g=1.5 mm/h, V_r=8 rpm, Ti=0.1 atom%).
(a) periphery of the wafer; (b) center of the wafer.

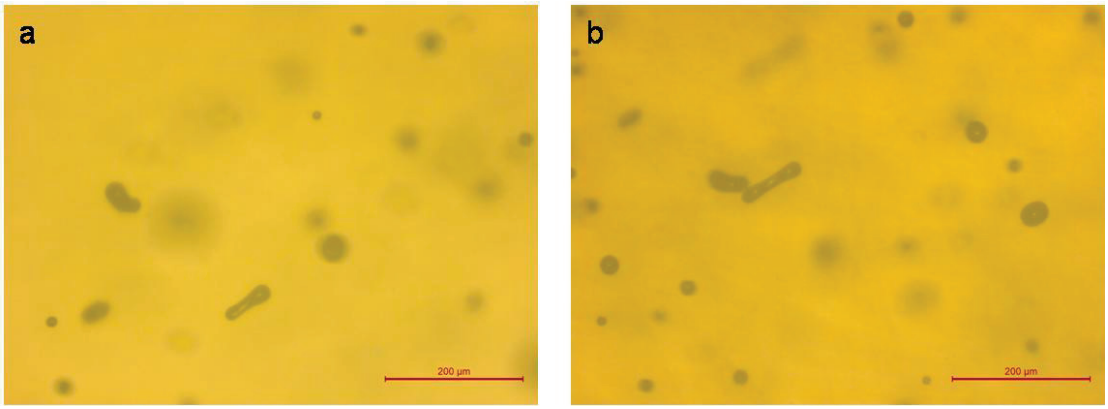

Figure 4.6 Optical microscopy of the top (beginning) (a); and end part (b) of wafer cut from Ti-doped sapphire crystal ingot showing the presence of bubbles (analysis in the center of the wafer). Growth conditions (V_g=2.5 mm/h and V_r=8 rpm).

The bubbles distribution of Ti-doped sapphire crystals is different with undoped one. Table 4.1 summarizes the obtained results as a function of the growth conditions. We can find that, the change of seed orientation have no apparent effect on bubbles size and distribution. The changes of pulling rate and Ti-concentration had significant effect on the distribution and quantity of bubbles. When grown at 1.5 mm/h and 0.1 atom% Ti-concentration, the crystals were completely free of bubbles. When grown at

2.5 mm/h, Ti-concentration from 0.1-0.28 atom%, the crystals contained bubbles in the center of top and end parts, and the top part had more bubbles than the end part. When Ti-concentration reached to 0.45 atom%, the crystals contained a great deal bubbles in the end part, the top part had a few bubbles. No matter what growth conditions, the middle part was always free of bubbles.

Table 4.1 Bubbles analysis in Ti-sapphire crystals as a function of growth conditions

Reference	CrysT1	CrysT2	CrysT3	CrysT4	CrysT5	CrysT6	CrysT7	CrysT8
Seed	a-axis	r-axis	r-axis	a-axis	a-axis	r-axis	r-axis	a-axis
Pulling rate (mm/h)	1.5	1.5	2.5	2.5	2.5	4	2.5	4
Rotation rate (rpm)	8	8	8	8	8	8	8	8
Ti-concentration (atom%)	0.1	0.1	0.1	0.17	0.28	0.28	0.45	0.5
Wafer thickness (mm)	5	5	5	5	5	5	5	5
Bubbles sizes (μm)	no	no	10-45	10-45	10-45	10-45	10-45	10-45
Bubbles distribution (analysis from the top, the middle and the end parts of the crystal)	no	no	Top (end, middle free)	Top, end (middle free)	Top, end (middle free)	Top, end (middle free)	Top, end (middle free)	Top, end (middle free)
The size of bubbles region in the top part (mm)	no	no	0.5-1	1.5-2	3.5-4	5-7	3-4	4-5
The size of bubbles region in the end part (mm)	no	no	0.1-0.2	0.1-0.2	0.5-1	2-3	20-25	25-30

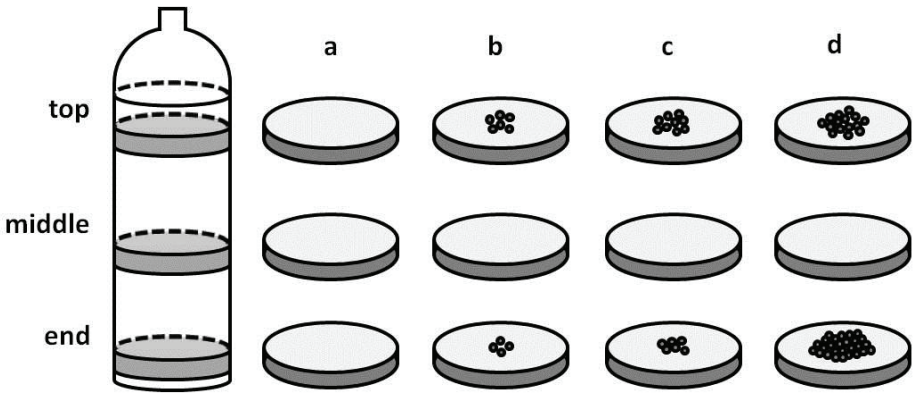

Figure 4.7 Schematic illustration of bubbles distribution of Ti-sapphire crystals with pulling rate, rotation rate and start titanium concentration respectively. (a) 1.5 mm/h, 8 rpm, 0.10 atom%; (b) 2.5 mm/h, 8 rpm, 0.10 atom%; (c) 4 mm/h, 8 rpm, 0.28 atom%; (d) 4 mm/h, 8 rpm, 0.5 atom%.

Figure 4.7 (a)(b)(c)(d) shows an illustration of the bubbles distribution as a function of growth conditions. As we have seen before, the Ti-doped crystal grown at low pulling rate are practically bubbles free. In the case of the crystals grown with high pulling rate, the bubbles were not distributed randomly in all the region of the crystals but centered of shouldering and tailing part, the middle part were always exempt of bubbles. The bubbles distribution in Ti-doped sapphire crystals is different with undoped sapphire crystals, which is due to titanium segregation. We will make a detailed analysis of this phenomenon in the section 4.2.3.

4.2.2 The shape and size of the bubbles

Bubbles size (diameters range from 10 μm to 45 μm) in Ti-doped sapphire crystals (figure 4.8) are comparatively larger than in sapphire crystals (diameters range from 2 μm to 5 μm) grown by Cz technique. Figure 4.8a shows some individual spherical bubbles and figure 4.8b shows some "bubbles" present various figure and size. As analyzed in the section of undoped sapphire crystals, the "bubbles" in various shapes are formed by several adjacent spherical bubbles.

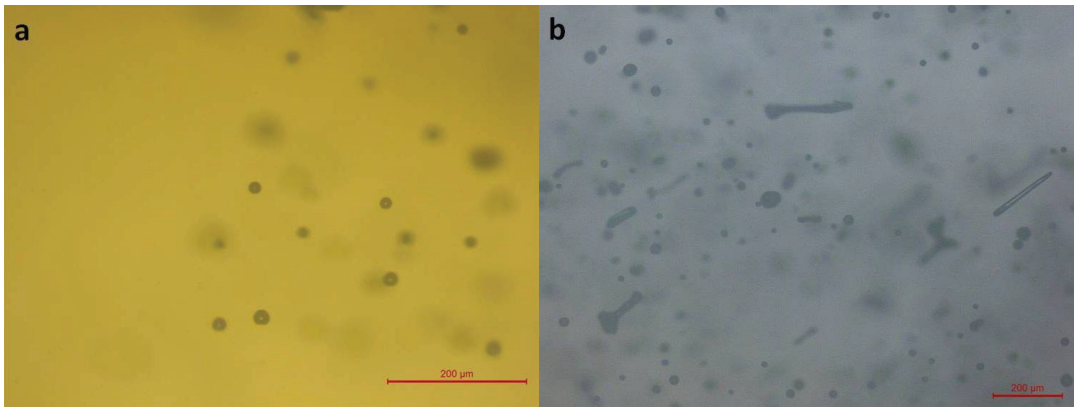

Figure 4.8 Bubbles observation in Ti-sapphire crystal wafers of 5mm thickness using reflection light. (a) individual bubbles; (b) integrated bubbles present different shape.

Figure 4.9a represents magnified image of individual bubbles, figure 4.9b and figure 4.9c illustrate connected bubbles arrange periodically in line while figure 4.9d indicates adjacent bubbles arranged curvilineally. For Ti-sapphire crystals, when the growth rate was lower or equal to 1.5 mm/h and rotation rate 8 rpm, the whole crystal

is free of bubbles or any other macro defects. When the pulling rate was increased to 2.5 mm/h, the crystal tended to contain micro-bubbles in the core of beginning and end parts, bubbles of beginning part are quantitatively more numerous than bubbles of end part, while the middle part is always exempted of bubbles. When the growth parameters was still 4 mm/h and 8 rpm, but the started titanium concentration was enhanced from 0.28 atom% to 0.5 atom%, serious titanium segregation took place and redundant titanium was finally solidified in the end part, thus more bubbles were captured in the end part accompanied the rejection of titanium (see figure 4.7). The difference of bubbles distribution between sapphire and Ti-doped sapphire crystals is due to that, for pure alumina the destabilization of solid-liquid interface results from the gas rejection while for doped materials from the rejection of the impurities, which is accordant with the reference [2]. Besides, a qualitative measurement of the Ti^{3+} spatial distribution inside the Ti-sapphire crystals validated this phenomenon further.

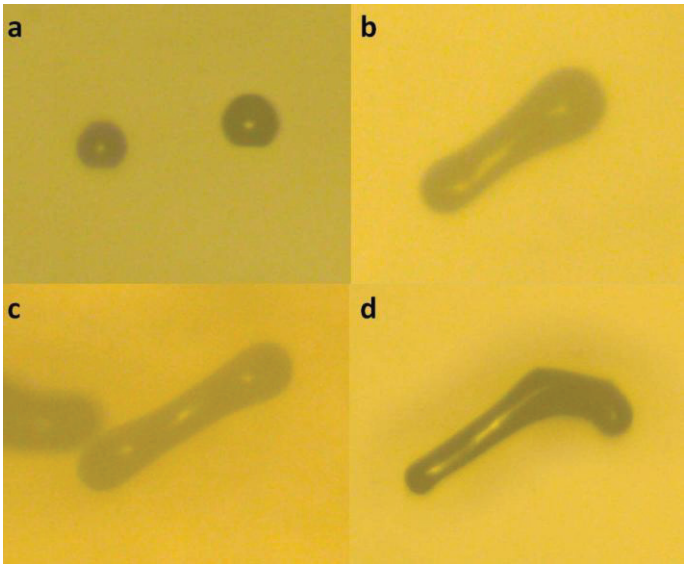

Figure 4.9 Magnified image of various bubbles visualizations under reflection light of Ti-sapphire wafers with 5mm thickness. (a)-individual bubbles; (b), (c)-linear arrangement bubbles; (d)-curvilinear arrangement bubbles.

4.2.3 The effect of Ti-concentration on crystal quality and bubbles distribution

For the growth of Ti-doped sapphire crystals, the Al_2O_3 starting material (melting point T_f=2050°C) with small additives of typically < 1 mol% of titanium dioxide (TiO_2)

must be molten under fixed conditions (T, PO_2) and the trivalent oxidation state (+3) must be stable for both metals. It is known that titanium has a variety of stable oxides ranging from TiO(+2) to TiO_2 (+4) and that a large number of Magneli phases can formed between Ti_2O_3 and TiO_2. Ti_2O_3 being the sole titanium oxide containing only Ti^{3+} ions, it is essential to find the adequate conditions to grow Ti^{3+}-doped sapphire crystals with predominance of Ti_2O_3 species and to obtain, in particular, crystals free of Ti^{4+} impurities. As the titanium (effective) segregation coefficient (the ratio of solute/dopant concentration Cs in the grown crystal near the interface to its concentration Cl in the melt) differs from unity (K= Cs/Cl <1), both a high proportion of (Ti^{3+}) active ions and a good homogeneity in their spatial distribution are key factors to obtain good quality Ti:Al_2O_3 laser crystals. Moreover, the subsistence of Ti^{4+} species and the existence of a parasitic absorption band (originating from the formation of Ti^{3+}-Ti^{4+} ions pairs) in the Ti^{3+} laser emission wavelength domain is an important issue since this absorption band strongly affects the laser threshold and slope efficiency of the materials.

In the case of k<1 less solute is incorporated into the growing crystals than provided by the melt. As a result the solute concentration in the melt (C_l) increases continuously during crystallization and leads to a solute concentration in the crystal that increase along the pulling direction. The axial solute profile can be describes with the well-known Pfann relation:

$$C_S = k_e \, C_0 (1-f)^{(k_e - 1)} \tag{4.1}$$

Where C_0 and f denoting the initial solute concentration in the melt and the solidified fraction of the melt respectively. The value f may vary between 0 for the beginning of the growth and 1 when the entire melt was crystallized. However, for typical oxide growth the concentration of solute and impurities in the melt already at f=0.5…0.75 has reached a level at which morphological instabilities of the interface become imminent and the process should be terminated.

4.2.3.1 Theoretical analysis of titanium dopant concentration

In order to reach optimum titanium content, the crystals were grown from the melts with different Ti concentration (0.1-0.5 atom%). According to our results, 0.1-0.3 atom% Ti in the melt was the good concentration to control the growth process (interface stability) and to obtain good quality transparent Ti-doped sapphire crystals under stationary stable conditions. At greater content of TiO_2 (Ti>0.3 atom%), Al_2TiO_5 phase was formed especially at the end of the crystal (figure 4.10). During the growth of large Ti-sapphire crystals by Cz technique, high pulling rates and high rotation speeds induce vibrations and temperature variations of the crystallization interface causing high thermal stresses. These factors decrease the optical quality of the crystals, and macroscopic defects such as bubbles and cracks, particular for large Ti^{3+}-Al_2O_3 crystals were observed. The distribution of the Ti^{3+} ion along the crystals was inspected in different parts of the grown ingots by Inductive Coupled Plasma Emission Spectrometer(ICP) method. The titanium segregation coefficient for the crystals grown by the Cz technique (this work) was measured to be 0.22. As it was expected, due to the ionic radii difference between Ti^{3+} (60.5 pm) and Al^{3+} (53.3 pm), the segregation coefficient was small.

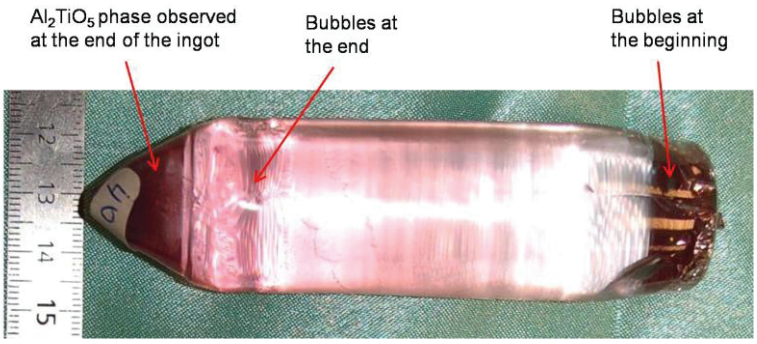

Figure 4.10 Ti-doped sapphire ingot grown from the melt with 0.45 atom% Ti, V_g =2.5 mm/h and V_r = 8rpm, seed: r-axis.

In addition, stressing the structure by incorporating such Titanium dopant in aluminium (Al^{3+}) sites increases the amount of defects such as inclusions, dislocation arrays, and striations if growth conditions are not carefully tuned. The theory of constitutional supercooling determines the suitable conditions for growing solid

solutions with a stable interface, which is described by the following equation [3]:

$$G/V \geq mC_0 (1-k)k / D \quad (4.2)$$

G: temperature gradient, V: growth velocity, m: slope of liquidus, C_0: bulk solute concentration, k: distribution coefficient of the solute, D: diffusion coefficient of the solute into the melt.

The formula indicates that the value of the growth rate needs to be lower than the critical value to stabilize growth. The fluctuations in the growth rate caused by thermal and instrumental instabilities must be lower than the critical growth rate.

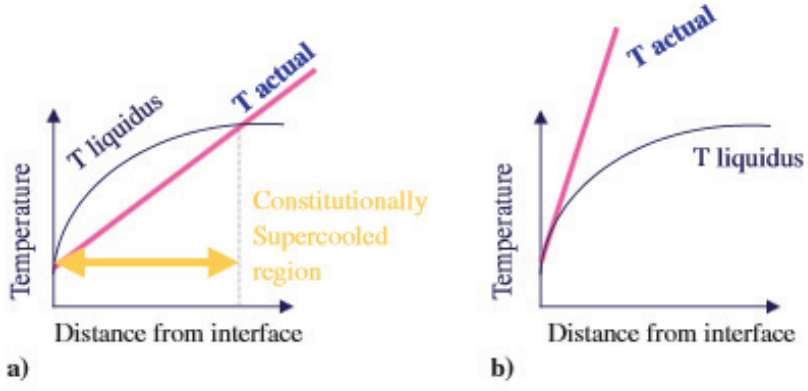

Figure 4.11 Constitutional supercooling. (a) conditions for constitutional supercooling; and (b) conditions for no constitutional supercooling.

Figure 4.11 graphically represents instances in which constitutional supercooling conditions are figure 4.11a encountered or b avoided. Figure 4.11a and b represents the steady-state equilibrium liquidus temperature distribution when k<1. As shown in figure 4.11b, if the actual temperature is higher than the liquidus temperature, solid solution growth from the melt can be achieved without constitutional supercooling. However, if the actual temperature is under the liquidus temperature as shown in figure 4.11a, constitutional supercooling will occur, leading to morphological instability of the interface. To achieve a good growth interface shape, it is necessary to optimize the temperature gradient. The temperature gradient has to be large enough to prevent both faceting at the interface and constitutional supercooling of the fluid close to the interface. However, too large of a temperature gradient must also be avoided since this can lead to large thermal stress which induces dislocation multiplication and sub-grain boundary formation in the hot crystal region.

Stabilizing the gradient is also an important factor. With stable gradients (or low temperature fluctuations in the melt), the growth rate will remain more constant and fluctuations in the dopant concentration will be minimized.

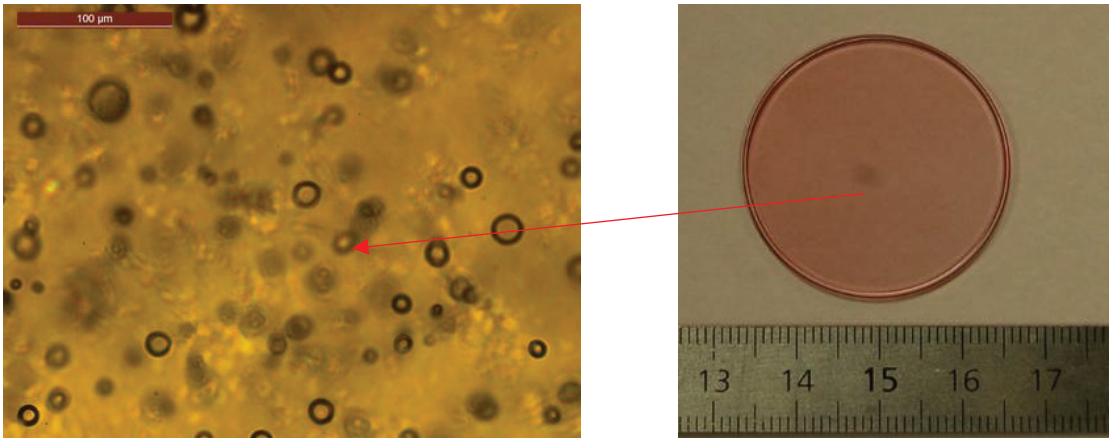

Figure 4.12 Ti-doped sapphire crystal containing bubbles in the center (starting Ti concentration in the charge 0.3 atom%)

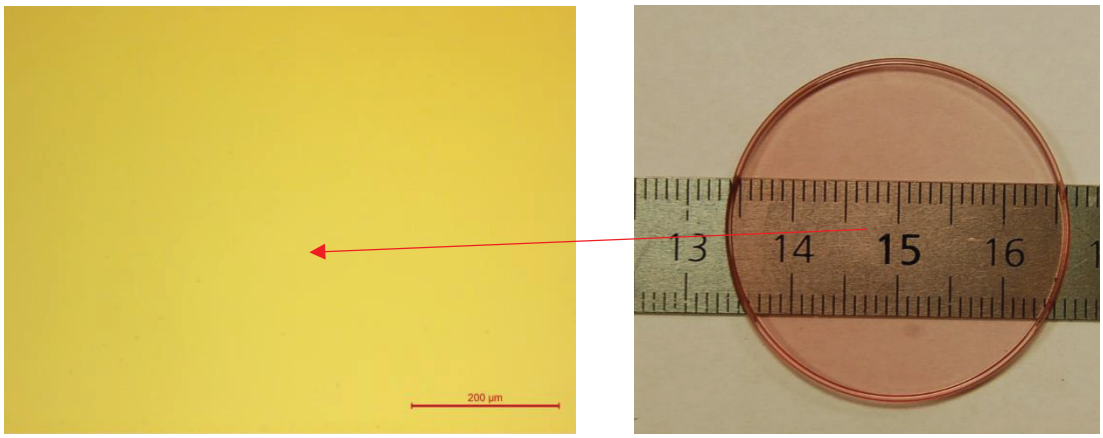

Figure 4.13 Ti-doped sapphire crystal exempt of bubbles (starting Ti concentration in the charge 0.1 atom%, V_g =1.5 mm/h, V_r= 8 rpm)

So in the case of titanium (Ti^{3+}) doped sapphire crystal the bubbles creation and their propagation are slightly complex than undoped sapphire. Their presence and their propagation were affected by the titanium concentration in the melt and their incorporation in the crystal through the crystallization interface. Using high titanium concentration in the melt will create strong segregation problem and some precipitate belonging to the binary Al_2O_3-TiO_2 system will be formed with high bubbles concentration (figure 4.12). Their distribution in the crystal depend on the growth parameters. But the most important thing, it is to suppress the composition of Al_2O_3,

addition of oxygen gas to the atmosphere is effective. However, the use of oxygen gas is not suitable for crystal growth of undoped and Ti-doped sapphire because of the large amount of oxygen gas inducing oxidization of the Ir crucible which induces contamination of the crystal. Therefore the examination of Ti-doped sapphire crystal grown under low pulling rate and steep thermal gradient conditions in order to suppress the entrapment of the supersaturated gases into the crystal. As the pulling rate was lower (1.5mm/h), an amount of bubbles in the crystal became small and bubbles can completely disappear (figure 4.13). Therefore, we suggest that a very low pulling rate less than 1.5mm/h is required to grow bubbles-free crystals in the argon atmosphere.

4.2.3.2 Titanium dopant concentration analysis by microlumienscense

A qualitative measurement of the Ti^{3+} spatial distribution inside the Ti-sapphire crystals inspected by microluminescence analysis validated the segregation of titanium dopant. The spectra were recorded on the wafers of 30mm diameter and 5mm thickness at different part of the crystals. For the measurement, the wafer was placed under a microscope (lens ×15) and was directly excited with a focused beam of 532 nm frequency-doubled and Q-switched Nd:YAG laser. The luminescence was recorded through the microscope by an optical fiber and transmitted to a monochromator that dispersed the emitted light onto a CCD detector cooled to -20°C. The measurement was performed in different transversal sections of the wafer exempt from bubbles or contains bubbles in the core.

The curves in figure 4.14a indicated relatively higher luminescence intensity and higher Ti^{3+} ion concentration at the periphery than the core of the wafers exempt bubbles, the radial distribution of Ti^{3+} in figure 4.14a expressed as luminescence at 730 nm is illustrated in figure 4.14b. We assume that the variation of luminescence intensity is linear with the concentration of Ti^{3+} in the crystal.

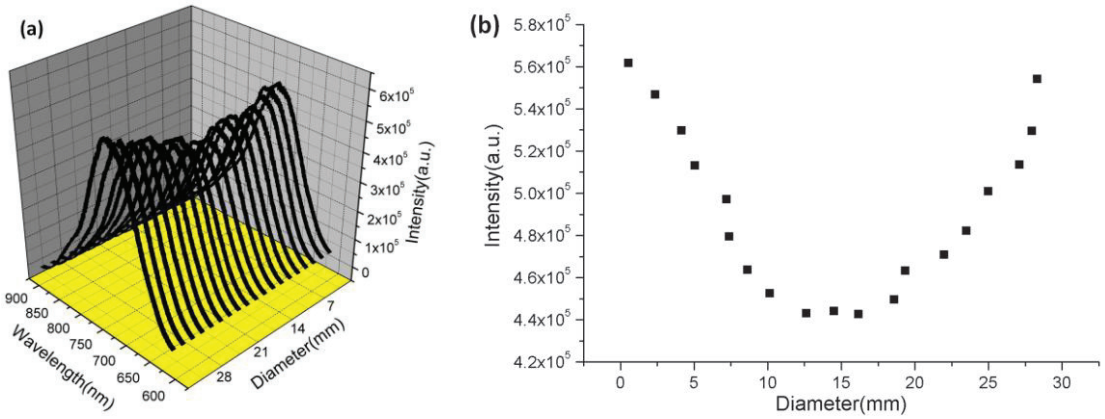

Figure 4.14 Microluminescence spectra recorded in different region of Ti-sapphire wafers without bubbles (excitation of the Ti^{3+} luminescence at 532 nm) (a); and (b) Profile of the Ti^{3+} ion distribution in the as grown Ti-sapphire crystal (starting titanium concentration in the melt was 0.28 atom %).

On the contrary, figure 4.15a shows relatively higher luminescence intensity and higher Ti^{3+} ion concentration in the core region contains bubbles than the periphery region without bubbles, the radial distribution of Ti^{3+} in figure 4.8a expressed as luminescence at 730 nm is illustrated in figure 4.8b. The explicit contrast of figure 4.7 and figure 4.8 manifests that for Ti-doped sapphire crystals the destabilization of solid-liquid interface results from the titanium rejection, which led to more bubbles were captured in the core of crystals.

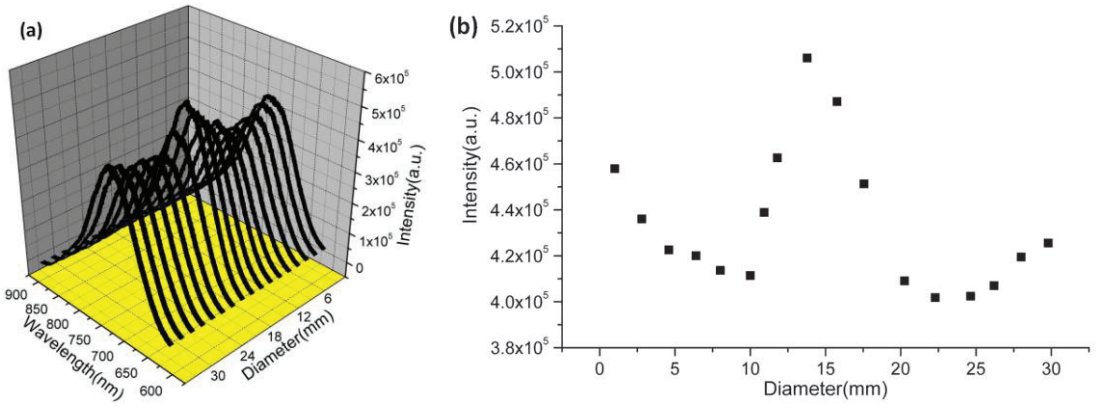

Figure 4.15 Microluminescence spectra recorded in different region of Ti-sapphire wafers contain bubbles in the core (excitation of the Ti^{3+} luminescence at 532 nm) (a); and (b) Profile of the Ti^{3+} ion distribution in the as grown Ti-sapphire crystal (starting titanium concentration in the melt was 0.28 atom%).

4.2.4 Bubbles comparison between undoped and Ti-doped sapphire crystals

As summarized in table 4.2, the bubbles difference between sapphire and Ti-sapphire crystals grown by Cz method is: the size, the density and the distribution.

✧ The size---- the bubbles' diameter of sapphire is in the range of 2-5 μm, while in the case of Ti-sapphire crystals the size is in the range of 10-45 μm.

Table 4.2 Bubbles' comparison between sapphire and Ti-sapphire crystals

Bubbles parameters	The horizontal distribution range	The vertical distribution range	The order Of bubbles' quantity	Distribution form	Diameter (μm)	Figure
Sapphire	Randomly in edge and center area	All the crystal	Top > end	Irregular and linear	2-5	Spherical
Ti-sapphire	Concentrated in the core, free of the edge area	Top and end parts	Top < end	Irregular	10-45	Spherical

✧ The bubbles density ---- under the same growth conditions, the bubbles density in Ti-doped sapphire is less than undoped sapphire crystals. It is supposed due to the starting raw material. To grow undoped sapphire, α-Al_2O_3 powder and sapphire crackles were used as starting charge. For Ti-doped crystals, sapphire crackles and high purity titanium powder were used. So the gas contained in alumina powder can be trapped by the crystallization interface during the growth process. This hypothesis needs more complementary characterization such alumina powder analysis by ESCA technique.

✧ The distribution----In the case of Ti-doped sapphire crystals, most of the bubbles were concentrated in the center of the crystal, but in the case of undoped sapphire the bubbles were distributed in the center and the periphery of the crystal. So the Kentic of bubbles distributions is different between the undoped and Ti-doped doped sapphire crystal.

4.3 Optical characterization

Many application of sapphire today demand the highest quality to achieve the upper limits of sapphire properties. In the previous part we have discussed the bubbles apparition which strongly affect the crystal properties. In this part we will present the crystal perfection and the optical properties of the grown crystal.

4.3.1 X-ray rocking curve

To characterize the crystallinity, XRC measurement was performed on the top, middle and end parts of Ti-sapphire single crystals grown along a-axis and r-axis. As the crystal containing low titanium concentration (0.1 atom%) and grown under low pulling rate (1.5 mm/h) and rotation rate 8 rpm don't contain bubbles, we did XRC characterization on these crystals. This measurement was done in Yoshikawa Laboratory (Japan). Figure 4.16a shows XRCs measurement of Ti-sapphire crystal grown along r-axis and figure 4.17b shows XRCs of sapphire grown along a-aixs.

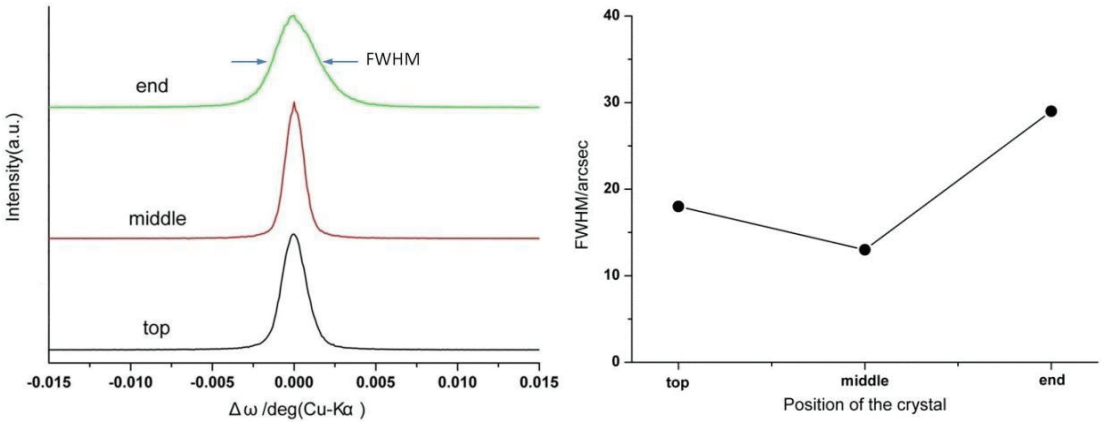

(a) (b)

Figure 4.16 XRCs of different parts cut from Ti-sapphire crystal grown along r-axis (a); and (b) FWHM comparison of XRCs. (initial Ti in the charge is 0.1atom%, V_g=1.5 mm/h, V_r= 8 rpm)

All XRCs present symmetrical single peak without any presence of second peak or shoulder peak. Neither low angle grain boundary nor mosaic structure were observed which indicates the Ti-sapphire crystals grown in the frame of this thesis have a good crystallinity. FWHM values were calculated from the X-ray rocking

curves of ω-scan, the values of top, middle and end parts of the two Ti-sapphire crystals were compared respectively in figure 4.16b and 4.17b.

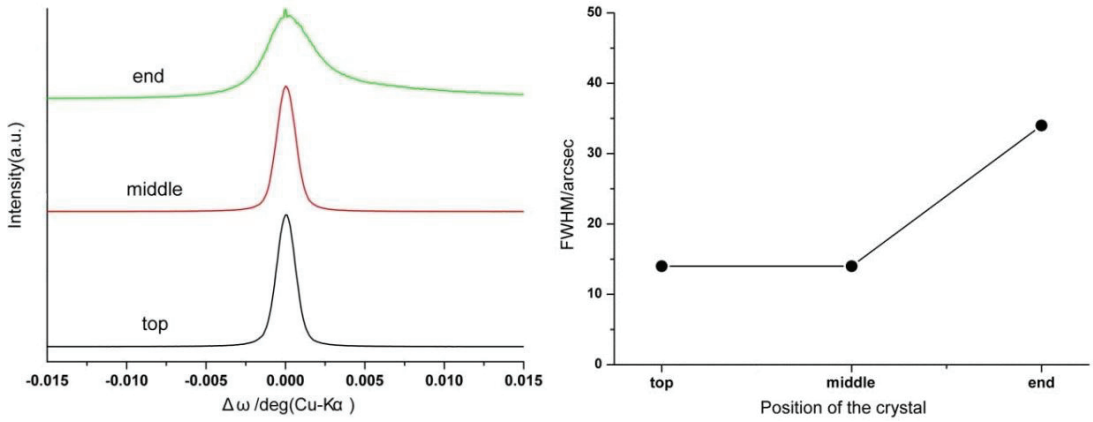

(a) (b)

Figure 4.17 XRCs of different parts cut from Ti-sapphire crystal grown along a-axis (a); and (b) FWHM comparison of XRCs in (a). (initial Ti in the charge =0.1 atom%, V_g=1.5 mm/h, V_r=8 rpm)

The middle part has the best crystal perfection, but the end (bottom of the crystal) part is less perfect than the top and the middle part. This is connected to the longitudinal segregation of titanium and the change of the crystallization interface during shoulder and tail preparation by the automatic software. Besides, as discussed in the section 4.3.3, usually the titanium concentration in the end part is higher than the top and the middle part because of titanium segregation phenomenon. All the FWHM values are smaller than 40 arcsec which confirm the good crystal quality. Compare with XRCs results of undoped sapphire crystals (section 3.4.1), Ti-doped sapphire crystals possessed better crystal perfection, this is due to the performed Ti-sapphire crystals were exempt of bubbles.

4.3.2 Raman spectra

To study the molecular structure of Ti-sapphire crystals, Raman spectrum measurement was performed. Figure 4.18 and figure 4.22 show Raman spectra of Ti-sapphire crystals grown along a-axis and r-axis respectively. The spectra obtained were compared with the standard spectra of corundum in the RRUFF^{TM} database. In figure 4.19, seven peaks at: 378 cm^{-1}, 418 cm^{-1}, 432 cm^{-1}, 450 cm^{-1}, 578 cm^{-1}, 645

cm^{-1}, 751 cm^{-1} were observed. The structure of Ti-sapphire crystals grown in the frame of this program are in good agreement with corundum. The seven bands are based on the D^6_{3d} symmetry of corundum and $2A_{1g}+5E_g$ active phonon modes. Figure 4.20 and figure 4.23 present Raman spectra measurement at the beginning (top), middle and end parts of sapphire crystals grown along a-axis and r-axis. Figure 4.21 and figure 4.24 present Raman spectra measured on edge and center region of the wafers cut from sapphire crystals grown along a-axis and r-axis. All the Raman measurement are similar to the corondum. This result substantiates that the doped Ti^{3+} ions substitute the Al^{3+} sites in the lattice, and no new phase was formed. Furthermore, no Raman shift caused by inclusion or other large defects has been observed.

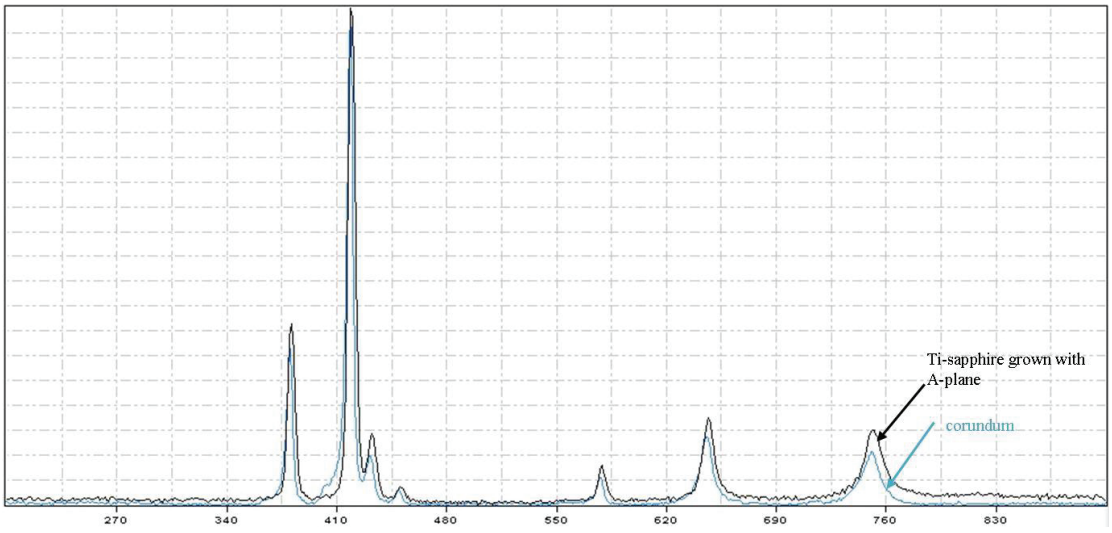

Figure 4.18 Raman spectrum of Ti-sapphire crystal grown along a-axis comparison corundum

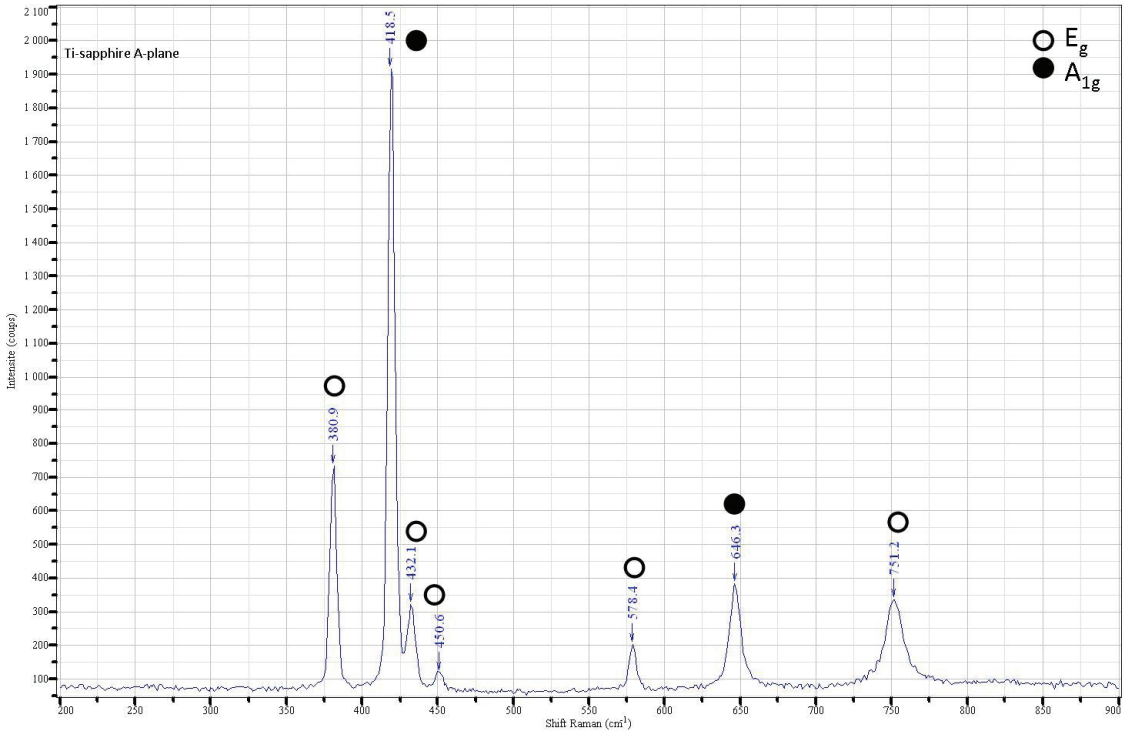

Figure 4.19 Characteristic peaks of Raman spectrum of Ti-sapphire crystal grown along a-axis

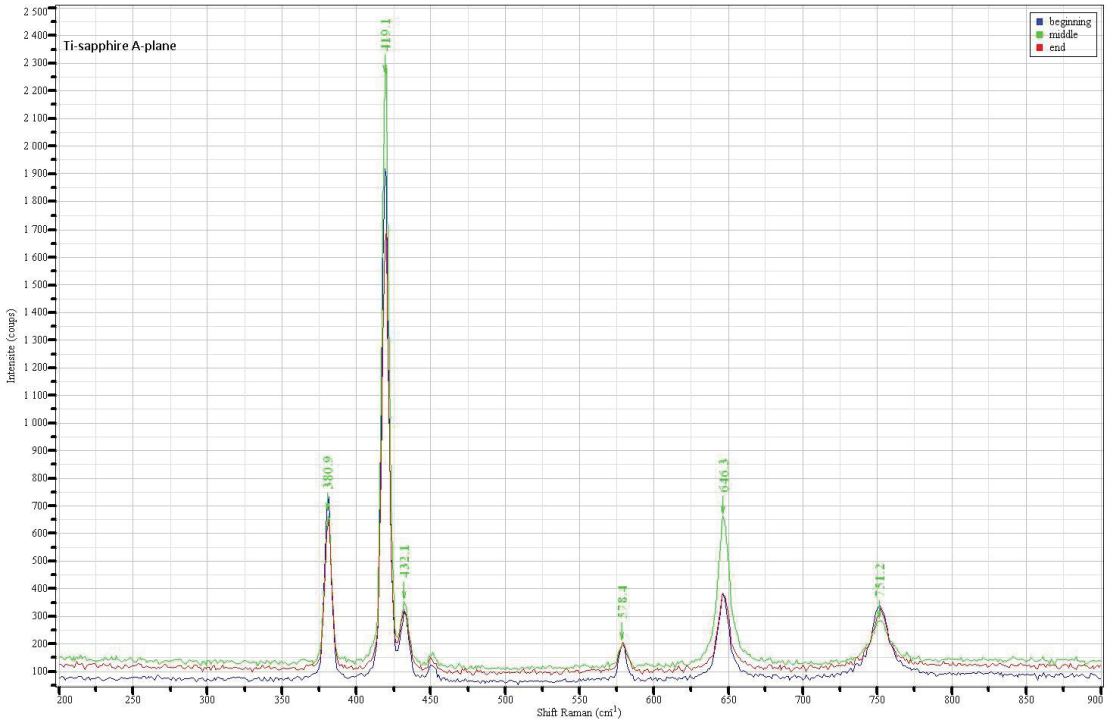

Figure 4.20 Raman Spectra measurement of Ti-sapphire crystal grown along a-axis (position: beginning, middle, end)

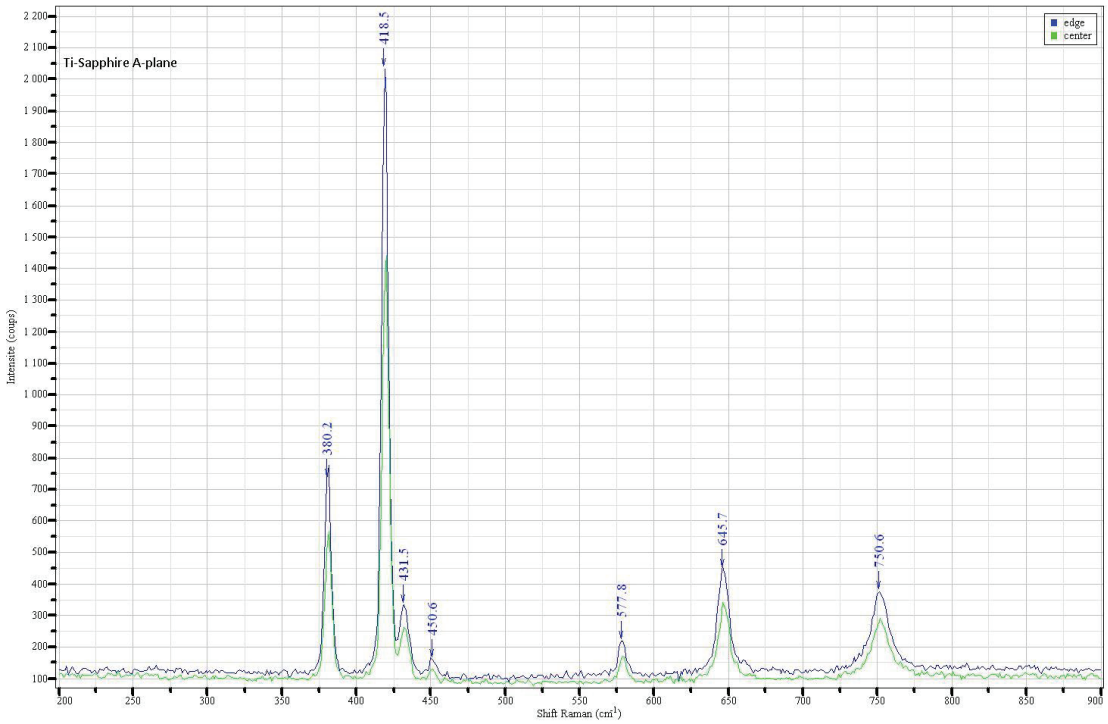

Figure 4.21 Raman spectra measured at different positions of Ti-sapphire crystal grown along a-axis

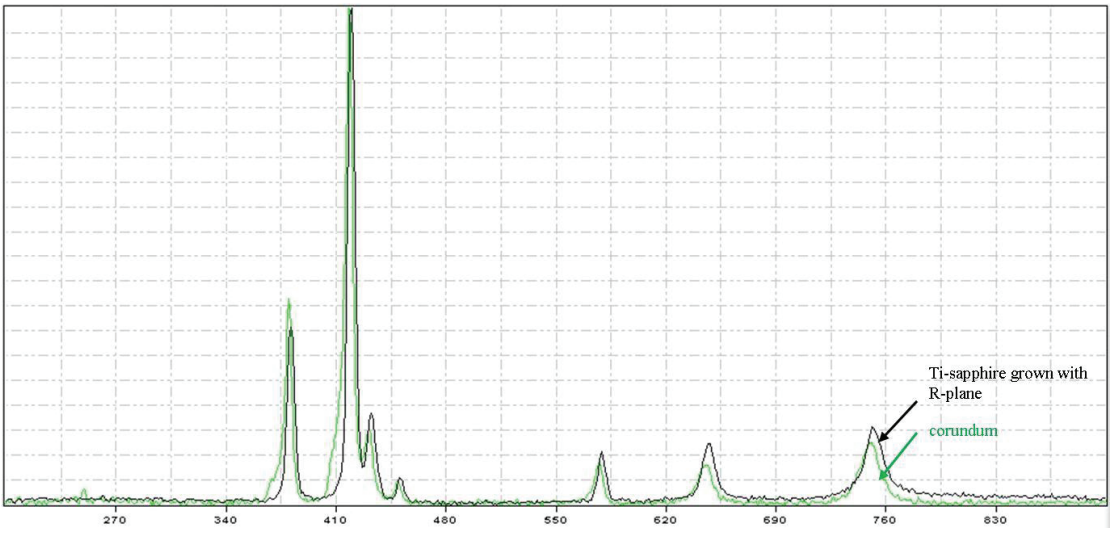

Figure 4.22 Raman spectrum of Ti-sapphire crystal grown along r-axis comparison with corundum

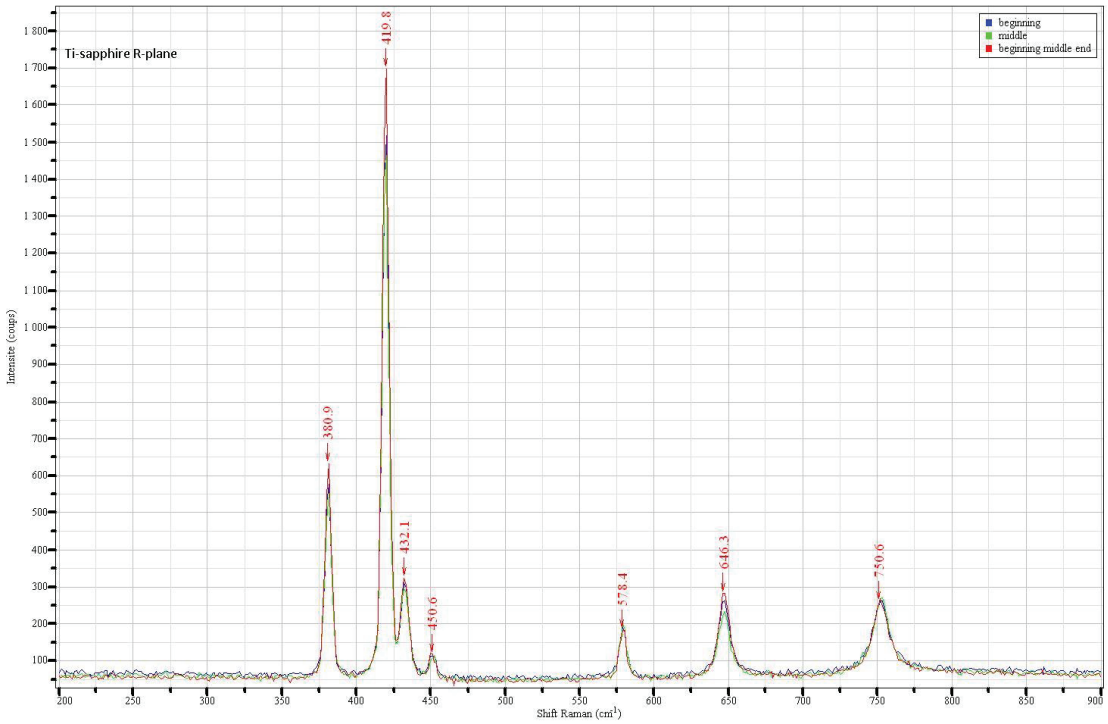

Figure 4.23 Raman spectra measurement of Ti-sapphire crystal grown along a-axis (position: beginning, middle, end)

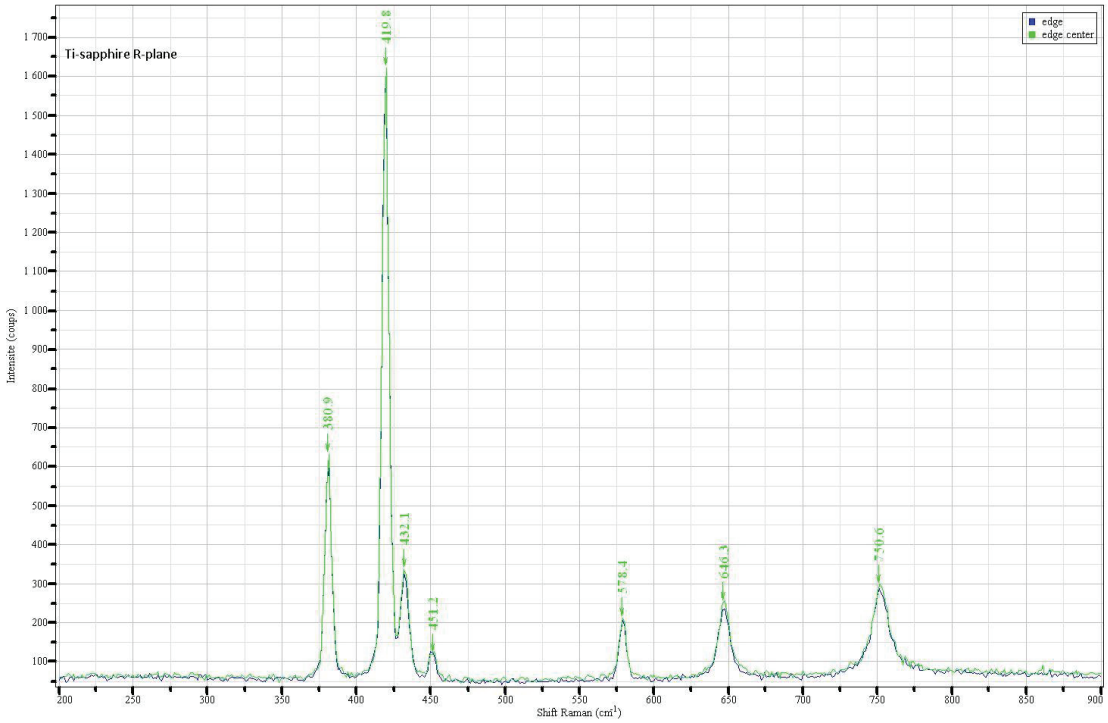

Figure 4.24 Raman spectra measured at different positions of Ti-sapphire crystal grown along r-axis

4.3.3 Absorption spectra

The absorption measurement were performed on six samples cut from different Ti-sapphire crystals grown along a-axis and r-axis. Table 4.3 summarizes the references of selected samples. In this measurement, the utilized light source has no polarization. The absorption spectra (figure 4.25) show two overlapping broad bands peaking around 490 and 525 nm, which correspond to two phonon side bands of the same Ti^{3+} optical transition from level $^2T_2$ to level ^2E, the double-peaked nature of the band is due to the Jahn-Teller effect of ^2E state splitting into two sublevels [4]. As it is known, in the α-sapphire lattice, Ti^{3+} ($3d^1$) substitutes Al^{3+} and is surrounded by an octahedron of oxygen with a slight trigonal distortion. Other researchers observed some UV absorptions which may be caused by a high concentration of Ti^{4+} ions, and a broad absorption band with a long tail, extending well beyond 800 nm is usually related to a charge transfer transition between coupled iron-titanium ion pairs (Fe^{3+} Ti^{3+}-$Fe^{2+}Ti^{4+}$), which is due to impurities such as Fe [5]. We didn't observe this band of our crystals.

Table 4.3 Ti-sapphire crystal samples used for absorption measurement

Sample number	Crystal number	Area of the crystal	Started titanium concentration	Thickness (mm)	Growth direction
1	39#	Top	0.10 atom%	5	r-axis
2	39#	Middle	0.10 atom%	5	r-axis
3	39#	End	0.10 atom%	5	r-axis
4	40#	Top	0.17 atom%	5	a-axis
5	40#	Middle	0.17 atom%	5	a-axis
6	40#	End	0.17 atom%	5	a-axis

The absorbance has linear relationship with the thickness and titanium concentration of the samples. In this measurement, the thickness of different samples are same, so the absorbance is assumed in function of titanium concentration. According to figure 4.25, the order of absorbance is: 6>5>3>4>2>1. The result indicates that the order of titanium concentration is: crystal 40# > crystal 39#; end of crystal 39# > top of crystal 40#; for both crystal 39# and 40#: end > middle > top. The

results are agreed with conclusions of 4.3.1 and 4.3.3.

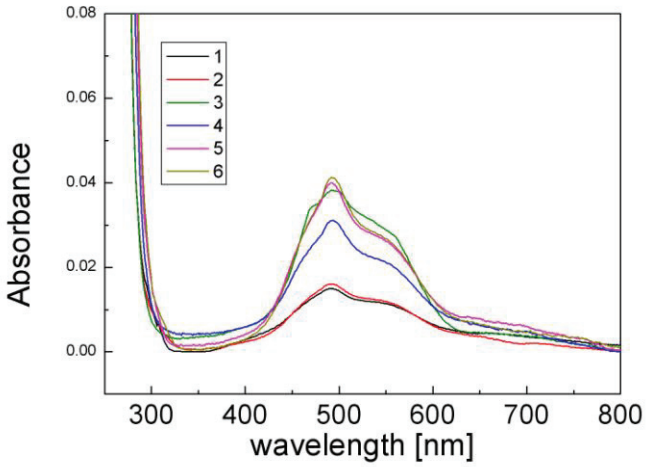

Figure 4.25 Absorption spectra of Ti-sapphire crystals as a function of titanium concentration and seed orientation (the reference of samples see table 4.2)

4.3.4 FOM calculation

The significance and the way to calculate FOM was introduced in the section 2.2.6. In this research, three Ti-sapphire crystals grown with different parameters by Cz method were chosen to measure FOM values. A green laser (λ=532 nm, ZM18) was used as pump band to measure the transmission of Ti-sapphire crystals, a 800 nm laser was used as laser band to measure the transmission of Ti-sapphire crystals. All the samples were measured without annealing treatment. The results are shown in table 4.4. The crystal had the best FOM value—122.585, was grown with pulling rate 1.5 mm/h and rotation rate 8rpm, owned titanium concentration 0.10 atom%, it is an ideal FOM value for this titanium concentration. The other crystals, due to titanium segregation and bubbles defects, the FOM values are not so desirable.

Table 4.4 FOM calculation of Ti-sapphire crystals grown by Cz technique

Crystal number	Thickness of sample (cm)	Seed	Puling rate (mm/h)	Rotation rate (rpm)	Ti-concentration (atom%)	T_{532nm}	T_{800nm}	FOM
T1	0.527	r[$10\bar{1}2$]	1.5	8	0.10	0.66	0.852	122.585
T2	0.526	r[$10\bar{1}2$]	2.5	8	0.10	0.69	0.852	101.238
T3	0.526	a[$11\bar{2}0$]	2.5	8	0.17	0.71	0.852	87.516
T4	0.525	a[$11\bar{2}0$]	2.5	8	0.28	0.66	0.851	78.380
T5	0.532	r[$10\bar{1}2$]	4	8	0.28	0.64	0.848	42.137

As discussed in the section 2.2.6, for Ti-sapphire crystals, T value is impacted by both the quality and the titanium concentration of the sample. Moreover, FOM of the Ti:Al_2O_3 laser crystals which measures the ratio of the absorption coefficients at the usual pump wavelength of 532 nm and at the maximum of the laser gain curve around 800 nm. The subsistence of Ti^{4+} species and the existence of a parasitic absorption band (originating from the formation of Ti^{3+}-Ti^{4+} ions pairs) in the Ti^{3+} laser emission wavelength domain is an important issue since this absorption band strongly affects the laser threshold and slope efficiency of the materials. From this point of view, it is worth noting that at high titanium concentration, the transfer process to Ti^{3+} becomes saturated, and the FOM values are generally reduced. Crystal T1 has the best quality due to more slower growth rate, it is free of any macroscopic defects and free of bubbles. Crystal T2 had same titanium concentration but grown with more fast speed. Crystals T3, T4 and T5 grown with higher titanium concentration and higher speed. All these crystals contained bubbles in the core and appeared titanium segregation. Besides, the transfer process to Ti^{3+} became saturated in high titanium concentration crystals. All above factors decreased FOM level significantly. In conclusion, to increase FOM of Ti-sapphire crystals, not only requested to enhance the dopant of titanium, but also necessary to improve the crystal quality. When more titanium was doped in sapphire, more slower growth rate was required to get homogeneous Ti^{3+} distribution.

4.3.5 Photoluminescence spectra

The luminescence of three Ti-sapphire samples were measured: sample 1 was obtained from the Ti-sapphire crystal grown along r-axis, pulling rate 1.5 mm/h, rotation rate 8 rpm, titanium concentration 0.10 atom%; sample 2 was obtained from the Ti-sapphire crystal grown along a-axis, pulling rate 2.5 mm/h, rotation rate 8 rpm, titanium concentration 0.17 atom%; and sample 3 was obtained from the Ti-sapphire crystal grown along a-axis, pulling rate 2.5 mm/h, rotation rate 8 rpm, titanium concentration 0.28 atom%. In the excitation range 190 nm to 270 nm, the three samples produced a blue emission centered at 430 nm (see figure 4.26a for sample 1).

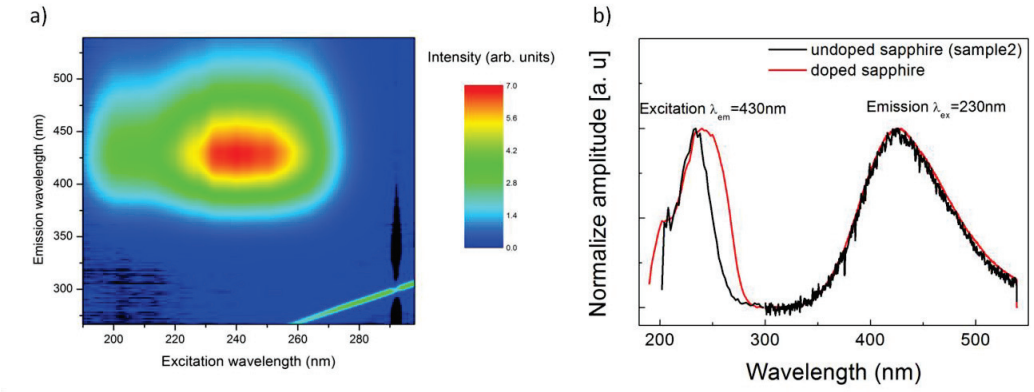

Figure 4.26 Excitation emission amplitude maps for the Ti-sapphire sample 1 in excitation range 190-300 nm and emission range 270-540 nm (a); and (b) comparison of excitation and emission spectra between the undoped sapphire sample 2 and the Ti-doped sapphire sample 1.

This emission is well known in Ti-doped sapphire [6,7,8] and it can be explained by the following scheme [7,9]:

$$Ti^{3+} + hv_{ex} \rightarrow T^{4+} + e^{-} \quad (4.3)$$

$$F^{+} + e^{-} \rightarrow (F)^{*} \rightarrow F + hv_{lum}\ (420nm) \quad (4.4)$$

Where F* stands for excited F center. This emission was also observed in the undoped sapphire sample 2 (see the section 3.4.5). But in case of Ti-doped sapphire, the excitation range of the luminescence was broader due to larger amount of Ti^{4+} in the crystal (see in figure 4.26b).

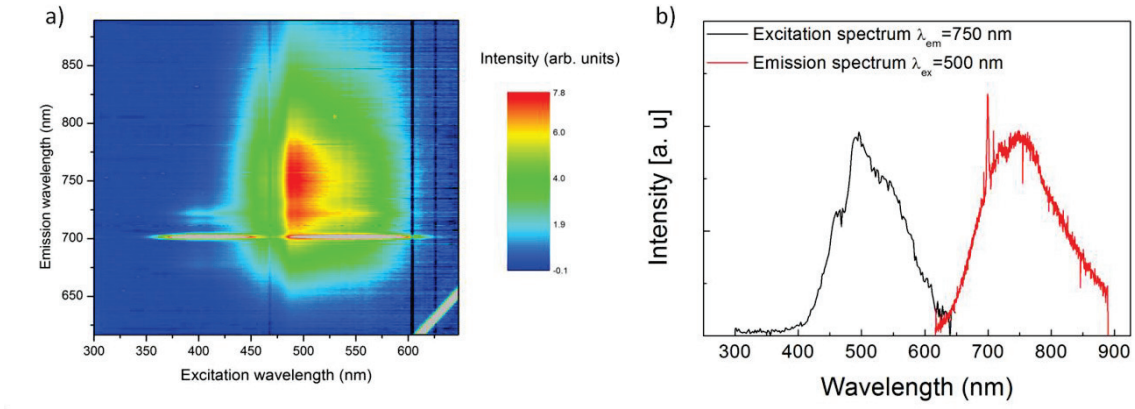

Figure 4.27 Excitation emission amplitude maps for the Ti-sapphire sample 1 in excitation range 300-650 nm and emission range 620-980 nm (a); and (b) excitation and emission spectra of the Ti^{3+} in sample 1.

In figure 4.27a, the luminescence of Ti^{3+} centered at 750 nm and of Cr^{3+} centered at 694 nm appeared clearly in the excitation emission amplitude map. The excitation and emission spectra of the Ti^{3+} are shown in figure 4.27b. The luminescence spectrum of the Ti^{3+} is accordant with the spectrum expected in this material [4] and the excitation spectra of Ti^{3+} presented the same shape as the absorption spectra presented in figure 4.25.

The 3 samples presented the luminescence properties as expected in case of Ti-sapphire crystal. No particular defects were revealed by the luminescence measurements. In addition, the luminescence lifetime of Ti^{3+} in Al_2O_3 was measured at room temperature, which was 3.16 μs.

4.3.6 Wavefront measurement

Figure 4.28 shows wavefronts recorded using 5mm thickness and 30mm diameter wafers cut from Ti-sapphire crystal grown under stationary regime (V_g=4 mm/h, V_r=8 rpm). A focused beam from He-Ne laser was sent through the wafer. The diameter of the laser waist without sample was measured to be 140 μm. A focal imaging system was used to image the end face of the sample into the beam analyzer Beamwave 500 from Phaseview. The analyzer recorded the beam and the wavefront profiles. The Getlase software was used to analyze the beam profile and to calculate the coefficients of the wavefront decomposition using Zernike polynomials.

The wavefront profile measured without sample was perfectly plane (Figure 4.28a, RMS=10 nm). Figure 4.28b illustrates the wavefront profile for the laser beam propagation in the bubbles. The wavefront profile is modified intensely by the defects (RMS=127 nm). A Zernike decomposition of the wavefront profile allows quantifying optical aberrations observed after laser propagation in the region contains bubbles. The bubbles caused significant astigmatism, coma and trefoil aberrations of the histograms featuring pertinent terms in the Zernike decomposition (figure 4.28c). The laser beam and wavefront measurements bring out and permit to quantify how bubble defects decrease seriously the optical properties of Ti-sapphire, therefore all ways and

means should be utilized to avoid this defect in the interest of high optical crystal quality.

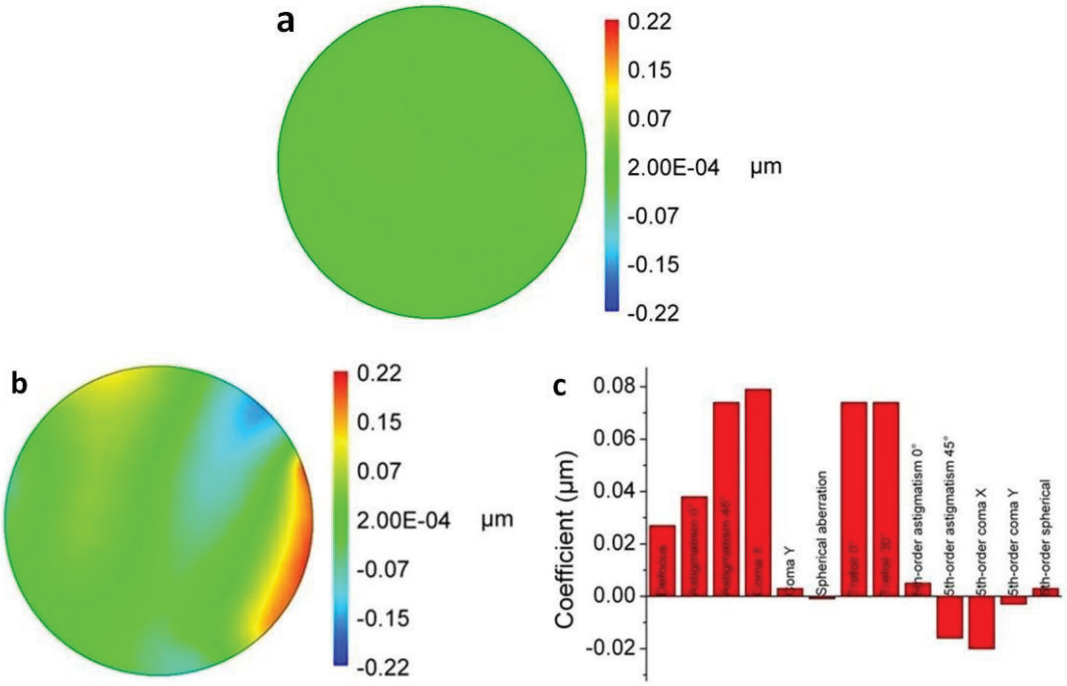

Figure 4.28 Weavefronts obtained from a 5mm thickness and 30mm diameter wafer of Ti-sapphire crystal grown under stationary regime (V_g=4 mm/h and V_r=8 rpm). (a) Wavefront profile measurement for the laser propagation in the region exempt from defects; (b) Wavefront profile measurement for the laser propagation in the region contains bubbles; (c) Zernike coefficient histogram obtained from the b wavefront profile.

4.3.7 Laser beam shape measurement

In order to estimate how inner bubbles will influence on optical qualities of Ti-sapphire crystals, a nondestructive method based on the utilization of an He/Ne laser emitting at 633 nm. A focused beam from the laser was sent through the wafers (diameter 30 mm, thickness 5 mm) cut from the Ti-sapphire crystal grown with pulling rate 4 mm/h and rotation rate 8 rpm. The output intensity was recorded with a CCD digital camera connected to a computer. Figure 4.29a presents the output intensity of the laser without passing samples. For the measurement of the region exempt of defects such as bubbles or cracks etc., the transmitted laser beam presented a near Gaussian profile (figure 4.29b) demonstrated high optical grade. When the laser beam was focused on the area contains intrinsic small bubbles, Figure 4.29c visualized more strongly losses in intensity as well as significantly disturbed profile.

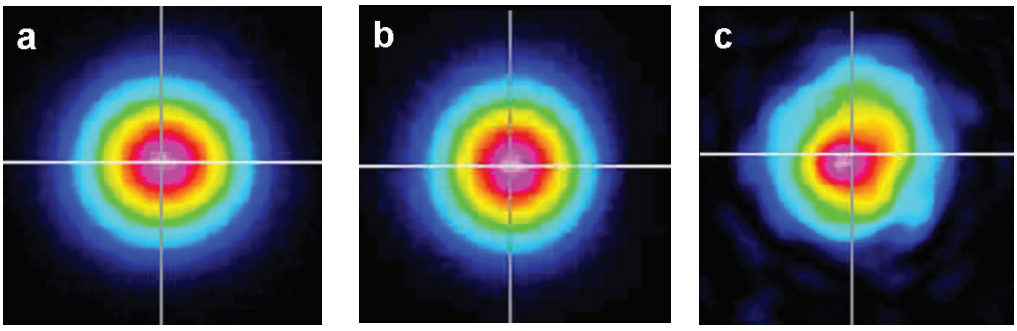

Figure 4.29 He/Ne laser beam shape (0.95 mW) (a) in air; and passed through the Ti-sapphire crystal region (b) without bubbles; (c) contained bubbles.

4.4 Conclusions

1. Ti-sapphire single crystals were grown by Cz method. They were grown along a- and r-axis, at different pulling rate and rotation rate, with various titanium concentration, respectively. All the as grown crystals were transparent and pink, exempt from macroscopic defects such as cracks. The structure of the Ti-sapphire crystals is in good agreement with corundum.

2. The Ti-sapphire crystal possessed excellent quality was grown under the following condition: grown along r-axis, at pulling rate 1.5 mm/h, rotation rate 8 rpm, with titanium concentration 0.10 atom%. The crystal was exempt of bubbles, furthermore, it had a desirable FOM value—122.585.

3. The bubbles were observed in the Ti-sapphire crystals grown at high speed and of high titanium concentration. The quantity of bubbles increased with the increasing of growth speed and titanium concentration. The bubbles presented spherical shape, their diameters varied from 10 μm to 45 μm. All the bubbles aggregated in the core of the crystal, they appeared in the top and end parts accompanying titanium segregation. The middle part of the crystal was free of bubbles. Some adjacent small bubbles integrated in large size "bubbles" with irregular shapes.

4. The order of bubbles' quantity in the crystal is: end>top, which is attributed to the segregation coefficient of Ti^{3+} in Al_2O_3 is less than 1, the superfluous titanium

was rejected in the residual melt, and the bubbles were rejected leech on to the impurities.

5. In the cross section of the Ti-sapphire crystal exempt from bubbles, the Ti^{3+} ions presented a radial distribution, viz. higher luminescence intensity and higher Ti^{3+} ion concentration at the periphery than the core of the wafers. On the contrary, in the cross section contained bubbles in the core, there were higher luminescence intensity and higher Ti^{3+} ion concentration in the center than the periphery region. This phenomenon farther manifests that for Ti-sapphire the bubbles were rejected together with the superfluous titanium dopant.

6. As expected, the Ti-sapphire crystals presented normal luminescence prosperities. The wavefront measurement and laser beam shape experiment visibly indicate that the bubbles degrade the optical quality significantly.

References:

[1] "http://www.cyberstar.fr." .

[2] O.M.Bunoiu, Th.Duffar, and I.Nicoara, "Growth and Characterization of Materials," *Prog. Cryst.*, vol. 56, no. 123, 2010.

[3] A. Ghosh, "Segregation in cast products," vol. 26, April, pp. 5–24, 2001.

[4] P. F. Moulton, "Spectroscopic and laser characteristics of Ti:$A1_20_3$," *J. Opt. Soc. Am. B*, vol. 3, no. 1, pp. 125–133, 1986.

[5] R. C.Powell, J. L. Caslavsky, Z. Alshaieb, and John M. Bowen, "Growth, characterization and optical spectroscopy of Al2O3：Ti^{3+}," *J. Appl. Phys.*, vol. 58, no. 6, pp. 2331–2336, 1985.

[6] A. Lupei, V. Lupei, C. Ionescu, H. G. Tang, and M. L. Chen, "SPECTROSCOPY OF Ti^{3+} : Alpha-Al_2O_3," *Opt. Commun.*, vol. 59, no. 1, pp. 1–3, 1986.

[7] G. Blasse and J. W. M. Verweij, "The luminescence of titanium in sapphire laser material," *Mater. Chem. Phys.*, vol. 26, no. 2, pp. 131–137, Oct. 1990.

[8] P. S. Page, B. S. Dhabekar, B. C. Bhatt, a. R. Dhoble, and S. V. Godbole, "Role of Ti^{4+} in the luminescence process of Al_2O_3:Si,Ti," *J. Lumin.*, vol. 130, no. 5, pp. 882–887, May 2010.

[9] V. B. Mikhailik, P. C. F. Di Stefano, S. Henry, H. Kraus, and A. Lynch, "Studies of concentration dependences in the luminescence of Ti-doped Al_2O_3," *J. Appl. Phys.*, vol. 109, no. 053116, 2011.

Chapter V Conclusions

In this PhD thesis, the background, motivation, methodology, and results of this research have been presented. The tendency of undoped and Ti-doped sapphire to brittle failure is associated with defects especially bubbles which strongly deteriorate the performance characteristics of pieces and the polish quality, as well as increase the light scattering. The bubbles size varies from submicron value to millimeters range. At high concentration of these defects ($>10^5 cm^{-1}$), the material is unsuitable for optical applications. The criteria of the crystal structure perfection is the density of point defects such as microscopic and macroscopic bubbles incorporated in the crystal. Therefore, in this research PhD thesis program a good deal of effort has been done to understand the origin of bubbles creation and their propagation in the grown crystals as a function of growth parameters and composition (case Ti-doped sapphire). Our aim is to eliminate these defects or at list decrease their density to the minimum level allowing the obtainment of performed properties.

By Czochralski(Cz) crystal growth technology, different undoped and Ti-doped sapphire crystal were grown under stationary stable regime. Many growth difficulties were solved and the bulk crystal growth was enable in ILM Laboratory. Whatever the starting composition and the seed orientation (a or r axis), the grown crystals are transparent, free of cracks and grains boundary. Up to 90% of the melt were crystalized in single crystal.

We have studied the bubbles propagation in the grown sapphire crystals. The bubble shapes are evidence of the complexity and variety of processes resulting in bubbles formation. As we have used iridium crucible as container and the growth process has been initiated in inert argon gas atmosphere, the main bubbles formation factor in sapphire grown crystal from the melt is believed to be the dissolved gas in the melt from the crystallization interface. When sapphire crystal is growing using a container such iridium crucible, it is difficult to ovoid overheating or overcooling of the

crucible, and thus of the melt. The melt interaction with impurities in the starting charge and the melt dissociation are possible supplements. Before their incorporation in the crystal, the bubble interact with crystallization front through interaction force. The change shape of the crystallization interface can capture macro or micro bubbles of the cooled melt. In this case, the bubbles are formed during the subsequent crystallization of those microvolumes due to density differences between the crystals and the melt. The melt dissociation, being a possible consequence of overheating, also increases the gas saturation. In this case the main dissociation products are atomic oxygen and atomic aluminum. Whatever the sapphire composition (undoped or Ti-doped) and seed orientation, bubbles formation are observed when sapphire is grown at high pulling rate. The pulling rate strongly affect the meniscus length which increased by increase the growth speed, in this case the concentration supersaturation region becomes extended over the entire meniscus and high bubbles density can be trapped in the crystal through the crystallization interface. The bubble size has no relation with the growing speed, which remain in the range 2 μm to 5 μm. Some adjacent small bubbles can congregate into bubbles clustering and present different shapes. As the growth speed increases, this trend of congregation is more possible to occur.

Other conditions being the same, the bubble concentration in Ti-doped sapphire is higher than undoped sapphire, because the melt doped with titanium contain more particles which interact with the container and the crystallization interface more intensively. In addition using high titanium concentration, a second phase micro particles may be precipitated in the crystal. In this case bubbles result from capturing of foreign solid particles by the crystallization front or from the phase segregation under the crystal cooling. The bubbles kinetic distribution in Ti-doped sapphire crystals is different with undoped sapphire. They are aleatory distributed in undoped sapphire and more concentered in the center of the Ti-sapphire. So the bubbles mechanism propagation is deferent and it is necessary to more investigate the different phenomenon involved during bubbles creation in Ti-doped sapphire.

The performed analysis indicates that one of the most important problems for the development on undoped and Ti-doped sapphire production is the increase in the size of the crystals (4 ,6 and 8 inch) and to get crystal without bubbles defects. This is explained not only by economic consideration, but also by technical requirements. Large sapphire crystals are needed for optics, laser and airborne windows with aperture of 600 mm and larger (for the medium-wave IR region of the spectrum). At the present, it is very difficult to grow large crystals without bubbles. In spite of the paper number about sapphire crystal growth, only a few papers have been published on bubbles in sapphire and Ti-doped sapphire bulk crystals. In addition their conclusions are often inconsistent and contradictory. This is essentially because every research group has used different growth machines, with different heating systems, different growth atmosphere, different crucibles and this makes for a difficult general treatment of the subject. Consequently, we performed Cz crystal growth process to understand the bubbles problems. It is so difficult to grow different crystals, cut, polish and characterize all the ingots. But in spite of the difficulties we succeeded to get a perfect bulk crystal without bubbles, we find the way to eliminate these bubbles (decrease pulling rate) and also we optimize the best titanium concentration (0.1 atom%) to minimize the titanium segregation and to decrease the bubbles concentration in Ti-doped sapphire. But the quantitative aspects of bubble formation and their propagation in Cz sapphire bulk crystal still remain approximate because of the various physical constant such as segregation, diffusion and so on.

Appendix I: List of figures

Chapter I

Chapter II

Chapter III

Chapter IV

Appendix II: Abbreviations

RF : Radio Frequency

FWHM : Full Width at Half Maxium

IR : Infrared

UV : Ultraviolet

CCD : Charge Coupled Device

ICCD : Intensified Charge Coupled Device

XRD : X-ray Diffraction

XRC : X-ray rocking curve

ICP : Inductive Coupled Plasma Emission Spectrometer

FZ : Floating Zone

Cz : Czochralski

Ky : Kyropoulos

EFG : Edge-defined film-fed growth

TGT : Temperature gradient technique

HEM : Heat change method

LHPG : Laser heated pedestal growth

μ-PD : Micro-pulling down

SAPMAC: sapphire growth technique with micro-pulling and shoulder-expanding at cooled center

FOM : Figure of Merit

rpm : Revolutions per minute

V_g : growth rate or pulling rate

V_r : rotation rate

fs : femtosecond

pm : picometer